Development of a Quantification Method for X-ray Microanalysis with an Electron Microscope

Paula Horny

Doctor of Philosophy

Mining, Metals and Materials Engineering Department

McGill University

Montreal, Quebec

2006

A thesis submitted to McGill University in partial fulfillment of the requirements of the degree of Doctor of Philosophy

Your file Votre référence
ISBN: 978-0-494-27789-8
Our file Notre référence
ISBN: 978-0-494-27789-8

DEDICATION

This thesis is dedicated to my son Adrien.

ACKNOWLEDGEMENTS

I thank my thesis supervisor Raynald Gauvin for his invaluable, patient and precious help, advice and guidance. He was always available to answer my questions by interesting and enriching discussions about my topic and many other things. I owe him my grateful thanks for what he taught me and what I learned from him.

I also thank Eric Lifshin for his listening and long enriching discussions. I thank my colleague Hendrix Demers for his comprehensive support in programming and Monte Carlo simulations and his fast answers to my computer questioning. I thank Helen Campbell for generously sharing with me her experience in scanning electron microscopy and x-ray microanalysis as well as her knowledge of the English language. I thank the professors, staff, graduate students of the Mining, Metals and Materials Engineering Department for the quality of the time I spent with them.

I thank the Fonds Québecois de la Recherche sur la Nature et la Technologie NATEQ and the Mining, Metals and Materials Engineering department of McGill University for the grants they allotted me to pursue my work.

Finally, I want to thank my husband for his unfailing support and patience during these years.

ABSTRACT

The overview of the history of quantitative x-ray microanalysis shows the efficiency of the use of standards to achieve the most reliable quantification. State-of-the-art cold field emission gun scanning electron microscopes offer excellent resolution but lack a sufficient level of beam current stability essential for reliable quantitative microanalysis. The purpose of this work is to devlop a new method for quantitative x-ray microanalysis adapted to unstable beam current conditions.

In the Cliff and Lorimer method, which was developed for the analytical transmission electron microscope, the composition was calculated from the ratio of the characteristic x-ray intensities of two elements in the same spectrum. In this work, this ratio method is applied to bulk specimens in a scanning electron microscope (SEM). In order to reduce the amplitude of error propagation, the proposed ratio for SEM quantitative microanalysis is the intensity of a x-ray divided by the sum of intensities of one or more characteristic lines of each of the elements found in the specimen. Moreover, the calculated x-ray intensities are corrected for the effects of absorption, fluorescence and Coster-Kronig yields, and other physical factors normally considered in microbeam analysis. Uncertainties in physical parameters and models, due to the lack of exhaustive measurements as well as their scattering, revealed by a disagrement between the measured and calculated ratios, are minimized

by the use of a calibration factor inserted into the ratio. This calibration factor is determined using a standard for a given element. It can be used as often as needed and allows for the correction of uncertainties in the x-ray detector efficiency. In order to quantify the specimen, the measured experimental ratio is compared to a simulated ratio with the appropriate calibration factor. The composition is interpolated from the theoretical ratio curves. Two methods of calculation of emitted x-ray intensity are proposed, by analytical calculations using the Pouchou and Pichoir model or by an in-house developed Monte Carlo simulation program. Two sets of National Bureau of Standards (NBS) microanalysis standard reference materials, AuCu (SRM 482) and AuAg (SRM 481), are used to validate this method.

The comparison of calculated composition with the nominal one underlines the need for a beam-energy-dependent calibration factor, particularly because of ionization cross-section uncertainties. The use of high energy characteristic x-ray lines (above 5 keV) permits accuracy around 3 % with a beam-energy-dependent calibration factor. The effects of beam energy, ionization cross-section models, mass-absorption coefficients and x-ray generation methods are compensated by the appropriate calibration factor. The change of the family of characteristic lines affects the accuracy. Finally, as in any quantitative microanalysis, the use of a filter to extract the characteristic intensity causes errors for low energy peaks. The analysis of the effect of calibration factors and mass-absorption coefficient enhances the need for refining the x-ray generation and emission parameters.

The error propagation is less important than if using the classical Cliff and Lorimer method in a SEM. However, the use of appropriate calibration factors and

pair of lines offers promising accuracy in almost any conditions. This method is independent of the beam current, which is the purpose of this work. Despite many uncertainties of physical parameters, this method offers an efficient and reliable alternative to quantitative x-ray microanalysis with any electron microscope. Although developed for a binary material, the method can be extended to heterogeneous, rough, multiple-component materials, inasmuch as it can be simulated with a Monte Carlo program or any other method that computes characteristic x-ray lines intensities.

ABRÉGÉ

L'utilisation de standards pour effectuer une microanalyse quantitative par rayons X se révèle être la méthode la plus efficace pour obtenir des valeurs sûres et précises. Un paramètre essentiel est la stabilité du courant de sonde. Or les microscopes à effet de champ les plus modernes, qui offrent une résolution sptatiale optimale, produisent des variations de courant nuisibles à la qualité de la quantification par rayons X. Ce projet propose donc de développer une nouvelle méthode de microanalyse quantitative par rayons X indépendante des variations de courant de la source.

La méthode de Cliff et Lorimer a été élaborée pour le microscope électronique analytique à transmission et pour des films minces. La composition est calculée à partir du ratio des intensités de raie caractéristiques de deux éléments dans le même spectre. Cette méthode est appliquée ici à des matériaux massifs dans un microscope électronique à balayage. Afin de réduire l'effet de la propagation des erreurs de mesure, le ratio est modifié sous la forme de l'intensité d'une raie caractéristique divisée par des intensités d'une raie caractéristique de chaque élément de l'échantillon. L'effet d'absorption, de la fluorescence et des transitions de Coster-Kronig sont ajoutés à l'équation de base du modèle d'intensité des rayons X. L'incertitude de détermination des paramètres physiques d'émission des rayons X, due au manque de mesures expérimentales exhaustives, est compensée par l'introduction d'un facteur de calibration dans le ratio. Le facteur de calibration, déterminé à

partir d'un standard, peut être réutilisé aussi souvent que possible et corrige aussi l'incertitude de détermination de l'efficacité du détecteur. Dans la procédure de quantification, le ratio mesuré à partir d'un spectre expérimental est comparé à la courbe décrite par les ratios calculés en fonction de la composition par un programme de génération de rayons X et calibrés. La composition est déterminée par interpolation. Deux méthodes de calcul des ratios sont proposées, soit avec le modèle analytique de Pouchou et Pichoir, soit avec un programme de simulation de Monte Carlo développé pour ce projet. Pour valider la méthode, deux groupes de quatre échantillons standards du National Bureau of Standards (NBS) sont utilisés : AuCu (SRM 482) et AuAg (SRM 481).

La comparaison entre les compositions calculées par cette méthode et les valeurs nominales révèle que le facteur de calibration doit varier en fonction de l'énergie du faisceau d'électrons afin d'optimiser la précision, notamment à cause de la connaissance très incomplète des sections efficaces d'ionisation. Cependant, avec un facteur de calibration adéquat, les ratios déterminés avec des raies caractéristiques à haute énergie permettent d'obtenir une précision de 97 % environ. L'influence des incertitudes sur les paramètres physiques comme les sections efficaces d'ionisation, le coefficient d'absorption et le modèle de génération des rayons X est corrigé par l'utilisation d'un facteur de calibration approprié. L'application du ratio à différentes familles de raies caractéristiques modifie la précision. D'autre part, comme pour toute microanalyse quantitative, l'utilisation d'un filtre pour extraire l'intensité des raies caractéristiques augmente les erreurs expérimentales. L'étude de l'impact du facteur

de calibration et du coefficient d'absorption massique souligne le besoin d'améliorer la connaissance des paramètres de génération de rayons X.

La propagation des erreurs est moins importante qu'en utilisant l'équation de Cliff et Lorimer. L'utilisation de facteurs de calibration appropriés permet de compenser ces incertitudes. Cette méthode se révèle indépendante des variations du courant de sonde. En dépit de beaucoup d'incertitudes sur les paramètres physiques, cette méthode offre une alternative efficace pour effectuer des micronalyses quantitatives avec tout type de microscope électronique, et particulièrement à effet de champ. Elle a été développée pour des échantillons binaires, mais peut être étendue à des matériaux hétérogènes, rugueux ou à composants multiples, dans la mesure où ils peuvent être simulés par un programme de Monte Carlo ou tout autre méthode qui calcule l'intensité des raies caractéristiques de rayons X.

TABLE OF CONTENTS

LIST OF TABLES

LIST OF FIGURES

Chapter 1
Introduction

In recent decades, electron microscopy has changed materials science, and introduced scientists to the inside secrets of matter. Today, state-of-the-art field emission gun scanning electron microscopes (FEG-SEM) are found in many materials laboratories and offer outstanding imaging capabilities. By collecting and analyzing photons emitted by electron-matter interaction, x-ray microanalysis can characterize the chemical composition of the irradiated volume with an excellent accuracy, better in the case of smaller probe size, as offered by a FEG-SEM.

Quantitative microanalysis was developped from the statement that the ratio of characteristic x-ray intensities is equal to the ratio of concentration, in the ideal world [13]. Therefore, the use of a standard material of known composition permits the determination of the composition of the unknown specimen. The use of real standards is the most accurate method [37, 79] but this method is costly (standards may be expensive and even not available), and time-consuming (microanalysis of standards). The use of standards requires the analyst to microanalyze standards containing each element [37, chapter 9]. While considering real materials, the ratio of x-ray intensities must be corrected to calculate the concentrations. Thus, the ratio of intensity of the characteristic x-ray of the same element in the specimen and in the standard, named the k-ratio, is equal to the ratio of concentrations multiplied

by a correction term, usually called ZAF, which takes account of the atomic number, absorption and fluorescence effects occuring in the material. This method was specially developed for wavelength dispersive spectrometers (WDS) which analyze a limited number of elements at the same time and give an accuracy better than 5 % in 95 % of studied cases [44]. Later, when energy dispersive spectrometers (EDS) provided the analyst with full spectrum measurements, standardless microanalysis was developed [79] on the basis of interelement correction rather than corrections based on k-ratio measurements. However, two major aspects, neglilible for wavelength dispersive spectrometers, are essential in energy dispersive spectrometry: background subtraction and peak deconvolution [63].

To go faster with an EDS, the standardless method seems appropriate but offers uncertain accuracy. Standardless quantitative microanalysis, which uses calculated or tabulated characteristic x-ray intensities as the standard, is now included in every EDS software package sold [72]. This method provides questionable results with doubtful reliability according to Newbury [72]. The other drawback of standardless microanalysis is the fact that there is no way of estimating the error of quantification. Moreover, there are intrinsic errors [72] due to variables that influence the analytical procedure, such as the class of material, the specimen shape, the choice of standard and the matrix correction, and they must be carefully evaluated before the microanalysis. Szalòki et al. [107] established quite a comprehensive statement of methods and knowledges in x-ray spectrometry, including x-ray microanalysis.

Moreover, the requirement for accurate x-ray quantitative microanalysis is, by definition, the conservation of microanalysis conditions, particularly the stability of

the beam current during the microanalysis, in order to keep constant the rate of x-ray generation. Thermal emitters (electron guns with tungsten filament) and Schottky emitters offer appropriate beam current stability, with less than 1% of variation per hour [37, chapter 2]. In order to improve imaging capabilities, cold field emission electron microscopes were developed in the 70's and they produce excellent quality of imaging, especially below 5 keV, because of higher brightness and lower chromatic aberration [29]. They permit the user to obtain very good spatial resolution, due to their performance at low beam energy [59]. However, beam current instability increases to around 5 % per hour [37, chapter 2]. And since FEG-SEMs produce low beam currents, the live times of the microanalyses must be increased, therefore, beam current fluctuation effects are amplified [37, chapter 2]. This instability is not eliminated with the ZAF or $\phi(\rho z)$ quantification with standards. Moreover, the use of standards and the measurement with a Faraday cup of the beam current in some microscopes complicate the quantification process, because they add extra steps in the process.

Hence, the purpose of this work consists of the development of a quantification process adapted to FEG-SEM beam current variations, without the systematic use of standards and the need for stable beam current. It introduces an innovative approach that can be applied for quantitative x-ray microanalysis. Based on the principle of the so-called Cliff and Lorimer method [20], developed for the analytical electron microscope, this work aims at determining the composition of a specimen independently of the beam current and by the calculation of theoretical characteristic x-ray intensities. However, it must be kept in mind that, whatever the used

method for quantitative x-ray microanalysis is, Heinrich reminded that this technique is definitely limited by a certain number of factors [46], such as uncertainties of x-ray measurements, chemical shifts, uncertainties in physical parameters used in the correction procedure, limitations in the type of standards, uncertainties in the standards specifications and effect of standard preparation.

The method introduced here can provide fast and accurate quantification. Differently to the Cliff and Lorimer method, the ratio is the intensity of a characteristic line of an element to the sum of the intensities of a characteristic line of each element. Calculations or simulations link this ratio to the compositon of the specimen. Since the x-ray intensities come from the same spectrum, the beam current cancels out. The most important point is however the determination of the physical parameters of x-ray generation which do not cancel, contrary to the ZAF process. Moreover, calibration is needed in order to adjust the ratio method to the microscope characteristics as well as to correct uncertainties in the models.

Chapter 2
History and principles of electron microscopy and x-ray microanalysis

2.1 Review of electron microscopy

The discovery of the wave property of matter in 1923 by L. de Broglie raised the idea that all particles, and particularly electrons, can behave as waves. This is the basic principle of the first trasmission electron microscope built in 1931 by the German researchers E. Ruska and M. Knoll, who replaced the light source by an electron gun and glass lenses by electromagnetic fields. The specimen was sliced a few hundreds of nanometers thick, in order to allow the electron beam to travel through the material. The electron and x-ray detectors were located below the specimen. The electron gun was a heated tungsten filament. A very high electric field extracted free electrons from the tip. Then, a series of apertures and electromagnetic condenser lenses concentrated the electron flux in the beam and reduced its diameter. The first scanning electron microscope was elaborated by Manfred von Ardenne in 1939, in Germany. This microscope allowed the observation of a bulk specimen by the detection of backscattered and emitted signals from the top surface of the specimen. The working principle was the irradiation of a specimen by a focused electron beam which scanned over a specified area of the sample surface. Further work showed that the best results were produced by the smallest beam diameter with the highest current density, meaning the higher brightness.

The typical column of a scanning electron microscope, shown in figure 2–1, is not so different from the first to the last state-of-the-art electron microscope. The specimen chamber can be located either below the column of optics or between the second condenser lens and the objective lens (or final lens). The objective lens makes the electron beam focus on the specimen surface and the scan coils make it scan the surface. The apertures and the condenser lenses make the electrons concentrate in the beam and the beam diameter reduce.

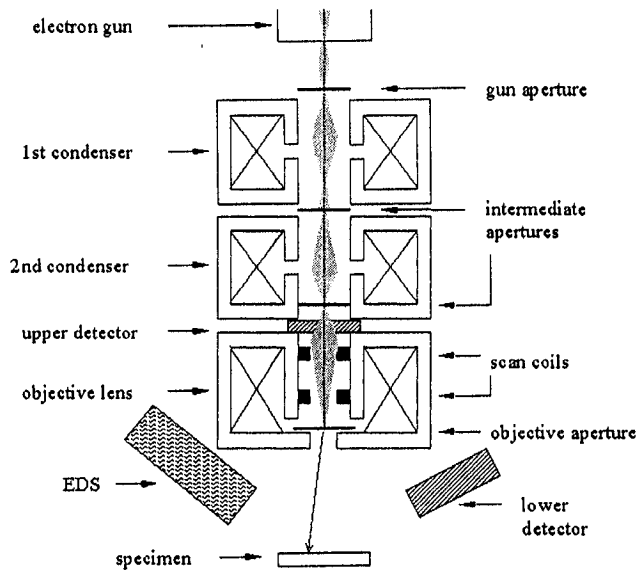

Figure 2–1: Schematic drawing of a typical SEM column, with the electron optics (from Goldstein [37])

2.2 Particle emission and detection

The interaction of the electrons with the atoms of the lattice generates a certain number of particles, such as secondary (SE I and SE II), backscattered (BSE) or Auger electrons (AE), characteristic and continuum photons, depending on the

chemical composition and the morphology of the material as shown in figure 2–2, which present the interaction volume of the electron in the matter and the main emitted particles used in an electron microscope.

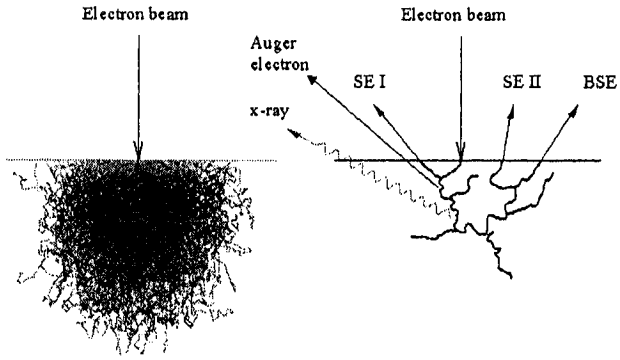

Figure 2–2: Electron simulation of the interaction volume (Win X-ray [36] pure Cu at 15 keV, 10 000 electrons) and the main emitted particles (SE I, SE II, BSE and x-rays [37])

When an incident electron interacts with the atoms, elastic and inelastic interactions occur. Elastic scattering essentially changes the electron trajectory, while inelastic scattering causes a transfer of the electron energy to the orbital electrons of the material. When the incident electron travels back through the specimen surface, it is called a backscattered electron (BSE) and the number of BSEs is dependent on the average atomic number of the material and its topography. When the incident electron interacts inelastically with the orbital atoms, a part of its energy is transferred to the orbital electrons. The excited atom then frees an electron, called a secondary electron. The secondary electron emitted by the incident electron is called an SE I and by a BSE is called an SE II. The de-excitation of the atom causes the emission of an Auger electron or a characteristic x-ray. The wavelength of the

characteristic photon depends on the shell transition in a specific atom. The number of generated characteristic photons is proportional to the concentration of this atom.

In order to collect secondary electrons, the lower detector (as shown in figure 2–1) is typically the Everhart-Thornley detector for secondary electrons. The Upper Detector is a more recent version of electron detector and detects the secondary electrons and the backscattered electrons within the solid angle of the objective aperture. In some cases, a backscattered electron detector is added as a disk below the objective aperture with a central hole for passage of the electron beam. The EDS detector collects the x-rays emitted by the material in the solid angle of detection of the detector window.

BSEs and SEs are composition-dependent but do not directly provide information about the different species and their weight fraction, because they depend of the average atomic number in the material. Characteristic x-ray microanalysis is the most reliable method to characterize the chemical composition of a material by electron microscopy, as Castaing demonstrated in his thesis in the late 40's [13]. He proposed linking the characteristic x-ray energy to the elements in the material and its intensity to the chemical composition [14]. This was the first x-ray microanalysis.

2.3 From x-ray generation to quantitative microanalysis

Quantitative x-ray microanalysis is based on the principle that the generated characteristic x-ray intensity of an element is dependent on its concentration, among other physical parameters. X-ray generation is initiated by inner-shell ionization for the characteristic x-rays and by continuous interaction for the bremsstrahlung. When a vacancy is formed by inner-shell ionization according to a probability described by

the ionization cross-section (see section 4.1), the excited atom regains its stable state by an electron jumping from an outer shell until the atom reaches a stable state. To do so, it will lose a certain amount of energy in the form of an ejected internal electron, such as an Auger electron or a characteristic photon according a fraction called the fluorescence yield (see section 4.2). The energy of the emitted photon is equal to the difference in energy of the two shells. This is the basic mechanism of characteristic photon generation.

For the generation of a characteristic x-ray, when an electron from an outer shell of energy, for example E_{LIII}, jumps to an inner-shell of energy E_K ($E_K > E_{LIII}$), a photon is emitted and it is called a K_α x-ray as shown in figure 2–3.

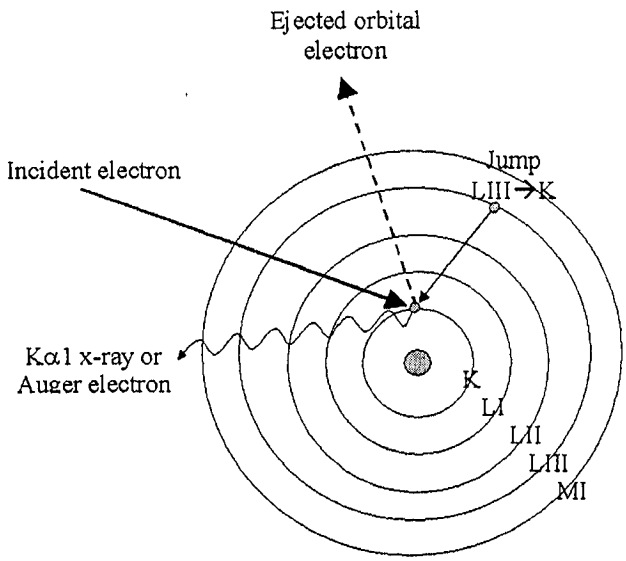

Figure 2–3: X-ray generation process by an atom ionized by an incident electron

The generated x-ray energy is:

$$E_{K_{\alpha 1}} = E_K - E_{LIII} \tag{2.1}$$

Since the energy level of each subshell is unique to a specific element, when a shell electron moves from an upper to a lower shell, the energy that the atom loses is characteristic of the atomic number. According to the example, the energy $E_{K\alpha}$, and therefore the wavelength λ, of the emitted photon are equal to the energy lost in the electron jumps as shown in:

$$E_{K_\alpha}(keV) = h\nu = \frac{hc}{\lambda} = \frac{12.4}{\lambda(\mathring{A})} \tag{2.2}$$

where h denotes Planck's constant and c the speed of light. The energy of transition between the different shells is tabulated [4] from experimental measurements or calculated [24] but are not exhaustive. For each element, many sub-shell transitions are possible, depending on the number of subshells, but some are more probable than others, according to the x-ray transition probability (see section 4.2). Thus the number of occurrences of a transition depends of this probability.

If an emitted photon is detected and if its energy is determined, it is possible to determine the chemical components of the material (qualitative microanalysis) and also their proportion (quantitative microanalysis). Since some fundamental parameters of x-ray generation were not accurately known at that time, Castaing [13] proposed using the ratio of characteristic x-ray intensities of the same element, in order to cancel out most of them. The quantification process consists of microanalyzing under exactly the same conditions an unknown material and a standard containing

the same elements (or different standards, containing at least one of the elements). If the fluorescence and absorption effects are very small, and the atomic number close, the ratio of measured intensities of standard and specimen is roughly proportional to the ratio of weight fraction of the emitting element i [13, 14] as Castaing's first hypothesis stated:

$$\frac{C_i}{C_i^0} = \frac{I_i}{I_i^0} = k_i \tag{2.3}$$

where C_i and C_i^0 are the concentrations of the element i in the specimen and the standard respectively, and I_i and I_i^0 are the x-ray intensities of the same peak of the same element. In order to determine the emitted intensity, the need for a correction factor depending on the material arose quite early.

In fact, equation 2.3 is particularly appropriate for thin foils. "Thin" means that the thickness is small with respect to the elastic mean free path of the electron; therefore it can pass through the specimen without significant deflection and energy loss. In this simplest case, the number n_i of generated photons per incident electron in a film of thickness Δz and for the element i is:

$$n_i = \frac{N_A C_i}{A_i} \sigma_i \varpi_i P_i (1 + T_{CK,i}) \rho \Delta z \tag{2.4}$$

where N_A is the Avogadro number, C_i the weight fraction of element i, A_i the atomic weight, σ_i the ionization cross-section, ϖ_i the fluorescence yield, P_i the line fraction (see section 4.2), $T_{CK,i}$ the Coster-Kronig transition coefficient (detailed in section 4.2, equation 4.19) and ρ is the material weight density. The ionization cross-section parameterizes the probability of emission of a characteristic x-ray and

depends on the incident electron energy. The fluorescence yield estimates the probability of generating a x-ray or an Auger electron by the excited atom. The physical models of the parameterization of characteristic x-ray generation are mostly very difficult to measure because of their interdependence.

When the target is thick, the electron backscattering through elastic collisions and the energy loss through inelastic collisions are no longer negligible. Moreover, the absorption effect is also rarely negligible and the emitted x-ray intensity I is expressed from the generated x-ray intensity I_0 at the mass-depth ρz in the slice of thickness $\Delta\rho z$ as:

$$\frac{I}{I_0} = e^{-\frac{\mu}{\rho}\rho t} \tag{2.5}$$

where μ/ρ is the mass-absorption coefficient and t is the distance traveled by the photon in the material as shown in figure 2–4, which presents a schematic diagram of absorption calculation. In order to generate the depth distribution of generated x-ray, the interaction volume is sliced as in figure 2–4 and the intensity of x-ray generated and emitted in each slice is calculated as in equations 2.4 and 2.5. The emitting element can also be fluoresced by a photon emitted by a different element. This phenomenon is the fluorescence effect. In that case, the relationship between the concentration and the characteristic x-ray intensity is more complex.

After escaping from the surface, the photon flies through the vacuum to the detector. Only the fraction of photons emitted in the solid angle of the detector (the base of the cone is the disk of the detector hole and the tip is located at the exit point of the photon) are collected as shown in figure 2–5. Then, the photon flies through

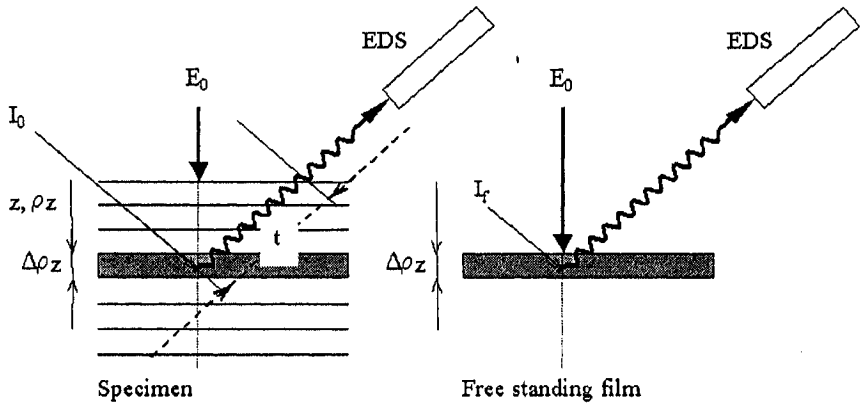

Figure 2–4: Schematic diagram for the calculation of absorption of photons and genration of the $\varphi(\rho z)$ curve

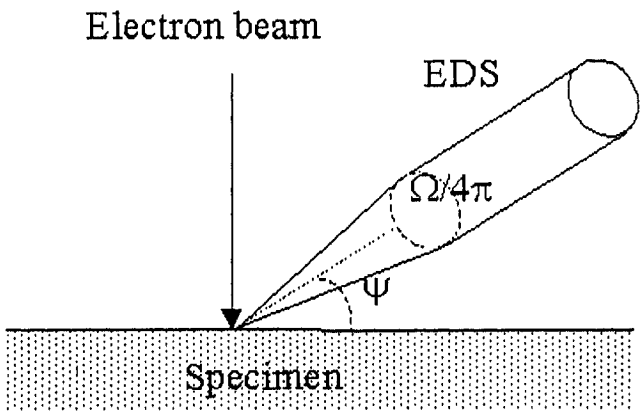

Figure 2–5: Definition of the detector take-off angle ψ and fractional solid angle of detection $\Omega/4\pi$

the different layers of the detector semi-conductor crystal as shown in figure 2–6 and described by Tsoulfanidis [110, chapter 6] and briefly in appendix A.

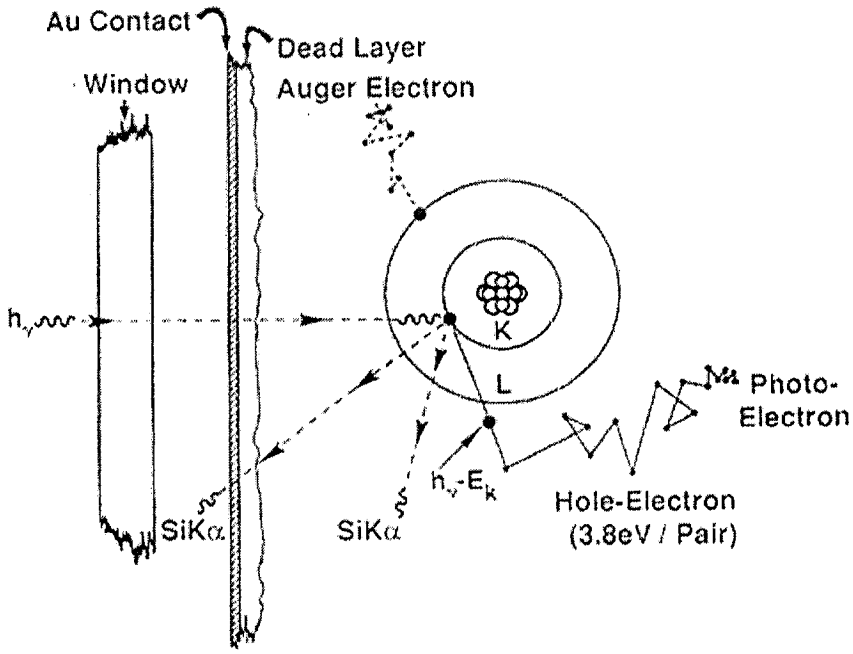

Figure 2–6: Schematic of the energy dispersive spectrometer window [37]

The x-ray intensity measured by the detector is the product of many parameters, as shown in the next equation for a bulk, flat and homogeneous specimen (from [37, 67]):

$$I = n_E \frac{\Omega}{4\pi} \frac{N_A C_i}{A_i} \epsilon_i \sigma_i \varpi_i P_i (1 + \delta_i)(1 + T_{CK,i}) \int_0^\infty \phi(\rho z) e^{-\chi_i \rho z} d(\rho z) \qquad (2.6)$$

where n_E is the number of incident electrons, $\Omega/4\pi$ the fractional solid angle of the detector, ϵ_i the detector efficiency and δ_i the fluorescence effect. $\phi(\rho z)$ describes the generated x-ray intensity with depth (without absorption). n_E is calculated from the

beam current i_B and the live time τ of microanalysis:

$$n_E = \frac{i_B \tau}{e} \tag{2.7}$$

where e is the electron charge ($1.6 \cdot 10^{-19}$ Coulombs). The absorption parameter χ_i is defined by:

$$\chi_i = \left.\frac{\mu}{\rho}\right|_i^{spec} \csc\psi \tag{2.8}$$

where ψ is the take-off angle of the detector and $\mu/\rho]_i^{spec}$ is the mass-absorption coefficient of element i in the specimen as explained by Goldstein [37] (see chapter 9):

$$\left.\frac{\mu}{\rho}\right|_i^{spec} = \sum_{j=0}^{j=n} \left.\frac{\mu}{\rho}\right|_i^j C_j \tag{2.9}$$

where n is the total number of elements and $\left.\frac{\mu}{\rho}\right|_i^{spec}$ is the mass-absorption coefficient of element i by element j.

The $\phi(\rho z)$ function describes the generation of x-rays as a normalized generated x-ray intensity which varies with the depth as suggested by Castaing [13]. The term ρz is the mass-depth and allows the comparison of different $\phi(\rho z)$ curves for materials of different density. The normalizing term is the intensity generated in a free standing layer of thickness $\Delta\rho z$ where no elastic scattering occurs as shown in figure 2–4. For each layer of thickness $\Delta\rho z$ at the mass-depth ρz, the definitions of the generated $\phi(\rho z)$ (without absorption) and emitted $\varphi(\rho z)$ (with absorption) functions are:

$$\begin{aligned} \phi(\rho z) &= \frac{I_0}{I_f} \\ \varphi(\rho z) &= \frac{I_0}{I_f} e^{-\chi \rho t} \end{aligned} \tag{2.10}$$

where I_0 is the generated intensity in the embedded film and I_f in the free standing film.

The layer can be either of the same average composition as the specimen or a pure element. The most important point is to keep the same layer thickness, density and composition for all calculations. Typical curves for Cu LIII ($\phi(\rho z)$, without absorption) and CuLα ($\varphi(\rho z)$, with absorption) are shown in figure 2–7 (Monte Carlo simulations, 10 000 electrons, 20 keV, $Au_{40}Cu_{60}$). The noise observed in the curves

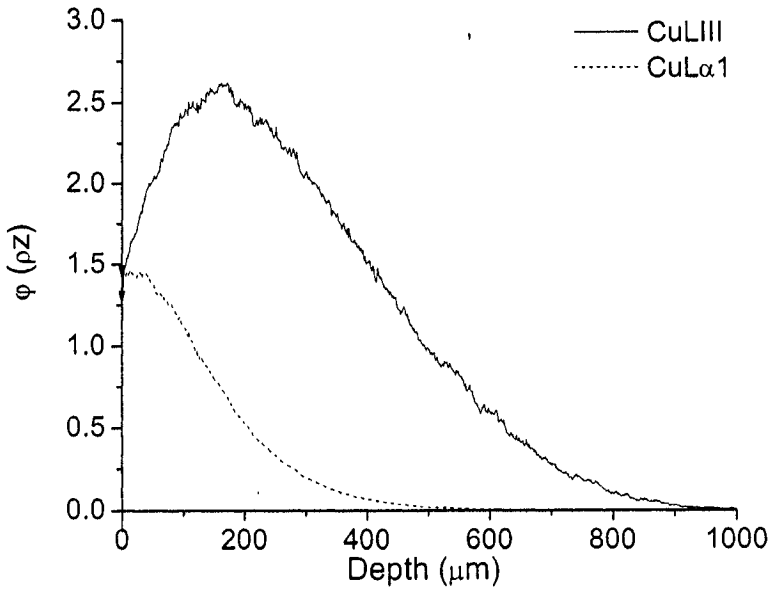

Figure 2–7: Calculated $\varphi(\rho z)$ curves for Cu LIII and Cu Lα in the $Au_{40}Cu_{60}$ standard alloy at 20 keV

is due to the statistical process of x-ray intensity generation. In order to reduce this noise, the number of calculated electron trajectories could be increased (10 000

electrons here) but it is time consuming (around 30 minutes for 10 000 electrons at 15 keV in an AuCu alloy). This phenomenon is important in the $\varphi(\rho z)$ curves because the signal is divided into the number of slices used to calculate the depth distribution of x-ray generation, therefore the number of calculated photons in each slice is small and then creating statistical noise. But when the curve is integrated to determine the characteristic x-ray intensity, this statistical noise is much reduced, and usually negligible. When an electron enters the specimen, the deflection of the trajectory increases the electron fly in the layers close to the surface. Moreover, backscattered electrons also ionize atoms and produce x-rays. Thus, the x-ray production close to the surface increases with the depth until the maximum R_m. At greater depth, the x-ray generation slows down because of backscattering, which reduces the number of available electrons and also because of energy loss, which decreases the electron's power of ionization. Finally, at depth R_x, the electron energy is below the ionization energy of the subshell and the curve has an horizontal tangent. The value for $(\rho z) = 0$ is called φ_0 and is the surface layer production of x-rays. This value is always larger than 1 in a bulk specimen, because of the backscattering effect, if the film and the bulk specimen have the same composition. The $\varphi(\rho z)$ shape is mostly influenced by the beam energy E_0 and the average atomic number ρ of the specimen [37]. $\varphi(\rho z)$ describes the emission of x-rays within the depth as shown in figure 2–8. The area below the curve is related to the intensity of the generated or emitted x-ray, to be multiplied by parameters as shown in equation 2.6. For further simplification, the

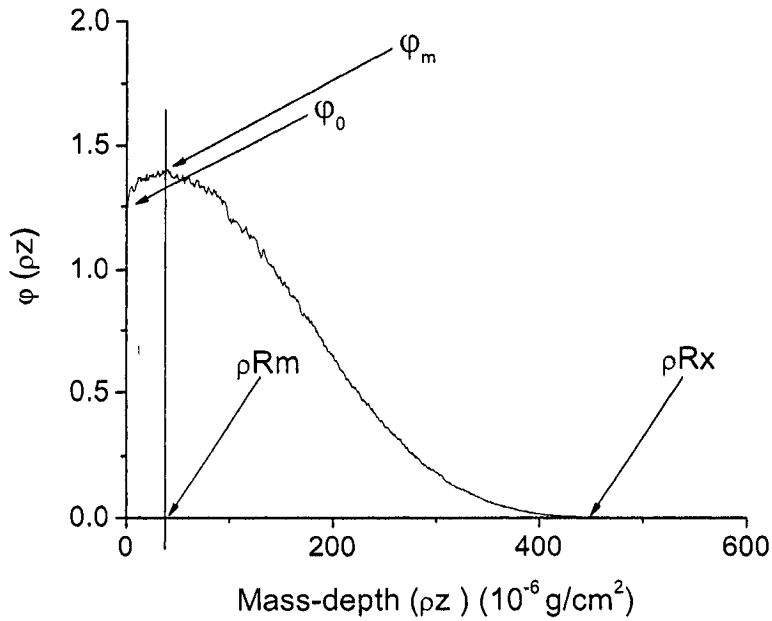

Figure 2–8: Typical $\varphi(\rho z)$ curve with main parameters

parameter γ_i for element i (see equation 2.6) is defined as:

$$\gamma_i = \int_0^\infty \phi_i(\rho z) \cdot e^{-\chi_i \rho z} d(\rho z) \tag{2.11}$$

For a thin film, $\phi(\rho z) \cong 1$, hence if $\frac{\mu}{\rho}]_i^{spec}$ is low, γ_i and a correction absorption is readily obtained.

With the analytical description of characteristic x-ray intensity in equation 2.6, the Castaing ratio is formulated for characteristic line intensities I_i and I_j, where i and j indicate two characteristic lines :

$$\frac{I_i}{I_j} = \frac{n_E^i(\Omega/4\pi)_i A_j \epsilon_i \sigma_i \varpi_i P_i (1+\delta_i)(1+T_{CK,i})\gamma_i}{n_E^j(\Omega/4\pi)_i A_i \epsilon_j \sigma_j \varpi_j P_j (1+\delta_j)(1+T_{CK,j})\gamma_j} \frac{C_i}{C_j} \tag{2.12}$$

Characteristic x-rays are emitted relative to the ionization cross-sections σ, the fluorescence yield ϖ, the transition probability P, are modified by Coster-Kronig transition $T_{CK,j}$ and fluorescence correction δ and are absorbed according to the mass-absorption coefficient χ (through the calculation of γ). Most of these physical models are essentially described by empirical, semi-empirical or theoretical equations for which the accuracy has not been systematically verified by experimental measurements, because no measurement was ever made in some cases (for the M shell ionization cross-section for instance). Moreover, the intensity of the collected x-rays is dependent on the x-ray detector parameters (window type, thickness and size, Au film thickness, detector efficiency and solid angle of detection see appendix A) which are not always known. Because of all these uncertainties, the best method for quantitative microanalysis consists of correcting the ratio empirically with standards.

2.4 Matrix correction in quantification

In the case of microanalysis with standards, in equation 2.12, i and j are the same element in the specimen and in the standard respectively. This theoretically makes the ratio dependent on beam current fluctuations. However, at the time of the beginning of microanalysis, the thermal field emitters offered stable beam current, so the ratio of current intensity was expected to cancel out. Because of this formulation, the ionization cross-section σ, fluorescence yield ϖ, Coster-Kronig factor T_{CK} and line fraction P cancel because they depend only on the element, as well as the detector efficiency ϵ and solid angle Ω (identical microanalysis conditions):

$$\frac{I_i}{I_i^0} = \frac{(1+\delta_i)}{(1+\delta_i^0)} \frac{\gamma_i}{\gamma_i^0} \frac{C_i}{C_i^0} \tag{2.13}$$

The fluorescence correction $(1+\delta)$ and the absorption term γ do not cancel because they depend on the composition of the material, which is not the same for the standard and the specimen. The conditions of the microanalysis must be rigorously the same for both standard and specimen, particularly beam current, but also specimen surface, electron beam energy, working distance and take-off angle. The microanalyses must also be done in the same microscope, since the detector efficiency ratio is also expected to be cancelled out. In order to make accurate quantification with the Castaing equation 2.3, a correction must be applied to the ratio according to equation 2.13 [37]. Then the equation 2.3 is rewritten as:

$$\begin{aligned} \frac{C_i}{C_i^0} &= [ZAF]_i \frac{I_i}{I_i^0} \\ &= [ZAF]_i \, k_i \end{aligned} \tag{2.14}$$

where ZAF is the most common correction and k_i as shown in equation 2.3. In fact, as explained above, the path of electrons, and consequently the generation volume of x-rays in the material, are modified by the other elements in the specimen. In comparison with the standard, there may also occur fluorescence. This matrix effect is conveniently divided into three dominant effects: the atomic number Z, the absorption A and the fluorescence effect F. The ZAF correction is the basis of quantitative x-ray microanalysis, and includes the δ and γ parameters of equation 2.13.

The correction terms Z, A and F are classically given by different sets of equations taking into account the estimated composition and density, as well as the atomic numbers of the elements as explained by Goldstein et al. [37] (see chapter 4). The atomic number effect Z is parameterized by Duncumb and Reed [26]:

$$Z_i = \frac{R_i^0 \int_{E_c}^{E_0} \frac{\sigma}{S^0} dE}{R_i \int_{E_c}^{E_0} \frac{\sigma}{S} dE} \tag{2.15}$$

where R_i^0 and R_i are the backscattering correction factors for the standard and specimen respectively. R is the fraction of ionization remaining in a target after the loss due to the backscattering of the beam electrons. σ is the ionization cross-section and S the stopping power $(-1/\rho)(dE/dx)$. The absorption correction A was first formulated by Castaing [13]. The emitted intensity is then calculated from the generated intensity:

$$A_i = \frac{f^0(\chi_i)}{f(\chi_i)}, \tag{2.16}$$

where $f^0(\chi)$ and $f(\chi)$ are the absorption terms [76] which is the ratio of the emitted intensity by the absorbed intensities in the standard and the specimen:

$$f(\chi_i) = \frac{\int_0^\infty \phi_i(\rho z) e^{-\chi_i \rho z} d(\rho z)}{\int_0^\infty \phi_i(\rho z) d(\rho z)} \tag{2.17}$$

Finally the fluorescence correction F is based on the work of Reed [84] (see section 4.4).

To obtain the atomic number and absorption correction, a different expression of the matrix effect is proposed by the $\varphi(\rho z)$ method. The atomic number and absorption effect are determined as follows:

$$\begin{aligned} [ZA]_i &= \frac{\int_0^\infty \phi_i(\rho z)\, e^{-\chi \rho z} d\rho z}{\int_0^\infty \phi_i^0(\rho z)\, e^{-\chi \rho z} d\rho z} \\ &= \frac{\gamma_i}{\gamma_i^0} \end{aligned} \tag{2.18}$$

where $\phi_i(\rho z)$ and $\phi_i^0(\rho z)$ are the functions describing the depth distribution of x-ray generation (without absorption), χ is the mass-absorption coefficient equal to $\mu/\rho \csc \psi$ (equation 2.8) and ψ is the detector take-off angle.

The $\varphi(\rho z)$ or $\phi(\rho z)$ curve have been parameterized by many researchers. Conveniently, φ will later signify both generated and emitted curves, for simplication, unless specified differently. One interesting description was gven by Brown and Packwood [9] who described the curve as Gaussian:

$$\varphi(\rho z) = \gamma e^{-\alpha^2(\rho z)^2} \left[1 - \left(\frac{\gamma - \varphi(0)}{\gamma}\right) e^{-\beta \rho z}\right] \tag{2.19}$$

where γ, α and β are parameters which depend on the target composition and the beam energy. $\varphi(0)$ is the value of the $\varphi(\rho z)$ at the surface. That equation does not work for targets of low average atomic number and low values of the parameter

γ because this parameterization does not permit the adjustment of the curve with a maximum far from the surface (for low atomic number elements) [78]. Another analytical calculation of $\varphi(\rho z)$ curves has been made by Pouchou and Pichoir [77] (PAP model) as described in section 5.2. Merlet [68] also worked on a double partial Gaussian correction. Continuing Merlet's work, Bastin et al. [3] proposed a modified Gaussian approach, in their program Proza96, as the sum of two Gaussian curves on each side of the maximum φ_m of the $\varphi(\rho z)$ curve maximum at ρz_m:

$$\begin{aligned} \varphi_l(\rho z) &= \varphi_m e^{-\beta^2(\rho z - \rho z_m)^2} \quad \text{for} \quad 0 \leqslant \rho z \leqslant \rho z_m \\ \varphi_r(\rho z) &= \varphi_m e^{-a^2(\rho z - \rho z_m)^2} \quad \text{for} \quad \rho z_m \leqslant \rho z \leqslant \infty \end{aligned} \tag{2.20}$$

(2.21)

where α and β are mathematical parameters of the Gaussian shape.

However, they are limited to homogeneous and multilayered materials. Another approach for the calculation of $\varphi(\rho z)$ is the Monte Carlo simulation, which can be adapted to any geometry in any conditions, without changing anything but the conditions of simulation. The Monte Carlo simulation program developed for this project is described in section 5.1.

In order to avoid the use of standards, most EDS manufacturers propose the standardless feature. Instead of using a real standard, it calculates a theoretical value of standard intensity as shown in equation 2.13 or uses a hidden standard. The reliability of this tool is however questionable as Newbury criticized [72].

When the method for quantitative microanalysis has to be chosen, the ZAF or $\varphi(\rho z)$ methods with standards, as explained above, are the best choice. However, this

does not offer the same accuracy in the FEG-SEM as in the microprobe, because of the beam current fluctuations. Figure 2–9 shows the frequency distribution of beam current fluctuations in the cold FE-SEM S-4700, in percentage of the beam current before the microanalysis, for 235 microanalyses of 100s livetime. One out of three microanalyses suffer a beam current variation larger than ±1%.

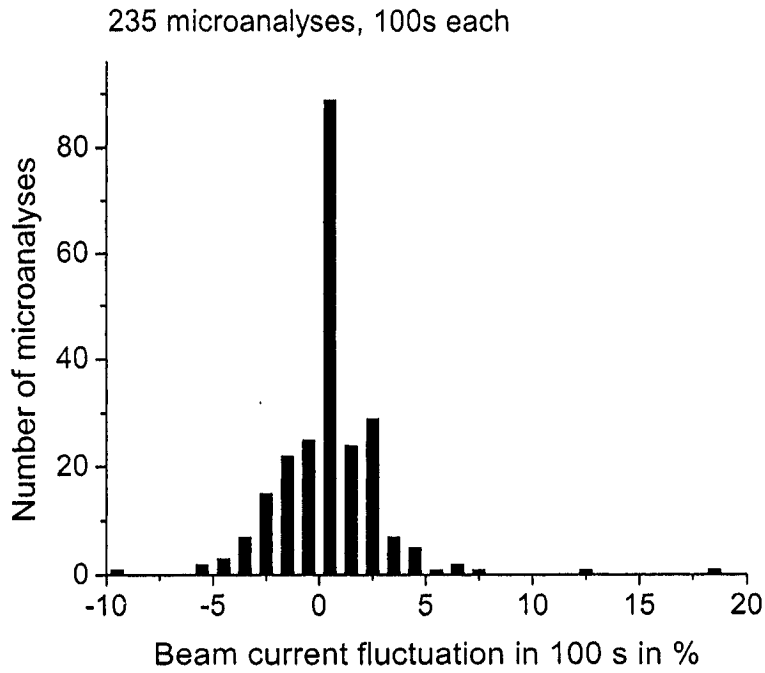

Figure 2–9: Beam current fluctuations for 235 microanalysis of 100 s livetime, in the Fe-SEM S4700

For all these reasons, this work proposes a method that in independent of the beam current fluctuations. However, the question of model accuracy arises again.

2.5 Cliff and Lorimer method for the analytical electron microscope

The method proposed here is an adaptation of the Cliff and Lorimer method [20, 15], first developed for x-ray microanalysis in a transmission electron microscope. For a target containing elements A and B, the ratio of the x-ray intensities I_A and I_B can be converted into a ratio of concentration by multiplying a proportionality factor K_{A-B}, tabulated or calculated for the couple A-B, the so-called Cliff and Lorimer factor:

$$\frac{C_A}{C_B} = K_{A-B} \cdot \frac{I_A}{I_B} \tag{2.22}$$

This is deduced from equation 2.12 where elements i and j are two different elements in the same spectrum, where the beam current cancels because it is the same for the two lines. For a very thin specimen, some assumptions can be made; the energy loss of the electrons is very small [35], so the ionization cross-section can be considered as constant and the absorption of the photons is negligible. In most cases, using K-shel characteristic x-rays, fluorescence effect can be neglected. The K_{A-B} factor is independent of the composition. Moreover, because of the high energy of the electron beam, most of time the user can work with K shell x-rays, and then there is no Coster-Kronig transition. With these simplifications, the Cliff and Lorimer factor is expressed from equation 2.12:

$$K_{A-B} = \frac{\sigma_B \varpi_B P_B \epsilon_B A_A}{\sigma_A \varpi_A P_A \epsilon_A A_B} \tag{2.23}$$

The ratio γ_A/γ_B are equal to one because of the characteristic of thin films. There is no absorption, therefore $e^{-\chi\rho z} \simeq 1$ because $\rho z \simeq 0$. Moreover, $\phi(\rho z) = \phi_0$, and because there is no backscattering (thin free standing film), $\phi_0 = 1$.

The following section will present how the Cliff and Lorimer ratio can be applied to bulk materials in an electron microscope.

Chapter 3
New quantification method for x-ray microanalysis

3.1 Development of the method

The Cliff and Lorimer method described in the previous section can be applied to a scanning electron microscope and bulk materials by introducing the effects of absorption, Coster-Kronig transitions and fluorescence in x-ray generation. The Coster-Kronig factor is added for L and M families of lines. The ratio of the net intensities of elements A and B can therefore be written according to the equation:

$$\frac{I_A}{I_B} = \frac{\sigma_A \varpi_A P_A \epsilon_A A_B (1 + T_{CK,A})(1 + \delta_A)}{\sigma_B \varpi_B P_B \epsilon_B A_A (1 + T_{CK,B})(1 + \delta_B)} \frac{\gamma_A}{\gamma_B} \frac{C_A}{C_B} \tag{3.1}$$

The Cliff and Lorimer equation can then be expressed in relation to equation 3.1:

$$\begin{aligned} \frac{C_A}{C_B} &= \frac{\sigma_B \varpi_B P_B \epsilon_B A_A (1 + T_{CK,B})(1 + \delta_B)}{\sigma_A \varpi_A P_A \epsilon_A A_B (1 + T_{CK,A})(1 + \delta_A)} \frac{\gamma_B}{\gamma_A} \frac{I_A}{C_B} \\ &= K_{A-B} \frac{F_B}{F_A} \frac{(1 + T_{CK,B})}{(1 + T_{CK,A})} \frac{\gamma_B}{\gamma_A} \frac{I_A}{I_B} \end{aligned} \tag{3.2}$$

where K_{A-B} is defined in equation 2.23. When the intensity of the element B is close to 0, the ratio increases rapidly and tends to diverge. In this work, another expression is proposed in order to prevent this problem. It consists of the normalization of the ratio between 0 and 1, as follows for a binary system A and B:

$$f_A = \frac{I_A}{I_A + I_B}$$

$$f_B = \frac{I_B}{I_A + I_B} \tag{3.3}$$

This method assumes that $C_A + C_B = 1$ as in the Cliff and Lorimer method [15]. The ratio in equation 3.3 can be simply linked to the Cliff and Lorimer expression as:

$$\begin{aligned} f_A &= \frac{1}{1 + \frac{I_B}{I_A}} \\ &= \frac{1}{1 + K_{A-B}\frac{F_B}{F_A}\frac{(1+T_{CK,B})}{(1+T_{CK,A})}\frac{\gamma_B}{\gamma_A}\frac{C_B}{C_A}} \end{aligned} \tag{3.4}$$

where γ is defined by equation 2.18 and F_i describes the fluorescence effect, most often according the Reed relation [84] and described by Goldstein et al. [37]. It can be shown that equation ?? can be reduced to equation 2.22:

$$\begin{aligned} 1 &= f_A(1 + K_{A-B}\frac{F_B}{F_A}\frac{(1+T_{CK,B})}{(1+T_{CK,A})}\frac{\gamma_B}{\gamma_A}\frac{C_B}{C_A}) \\ \frac{C_A}{C_B} &= \frac{f_A}{1-f_A}K_{A-B}\frac{F_B}{F_A}\frac{(1+T_{CK,B})}{(1+T_{CK,A})}\frac{\gamma_B}{\gamma_A} \\ &= K_{A-B}\frac{F_B}{F_A}\frac{(1+T_{CK,B})}{(1+T_{CK,A})}\frac{\gamma_B}{\gamma_A}\frac{I_A}{I_B} \end{aligned} \tag{3.5}$$

If there is no absorption, in a thin film for instance, if the Coster-Kronig transition can be neglected and if there is no fluorescence, or if γF product is equal to 1 and the equation simplifies into the Cliff and Lorimer equation. In some cases, simplifications can be made to equation 3.4, for instance if there is no absorption (high x-ray energy), no Coster-Kronig transitions (K lines), no fluorescence (the difference between the energy of the characteristic x-ray and the ionization energy of a subshell of the other

element is large) or if the product of all these terms is equal to 1. In that case:

$$K_{A-B}\frac{F_B}{F_A}\frac{(1+T_{CK,B})}{(1+T_{CK,A})}\frac{\gamma_B}{\gamma_A}=1 \tag{3.6}$$

and the ratio can be written as :

$$f_A=\frac{1}{1+\frac{C_B}{C_A}}=C_A \tag{3.7}$$

because $C_A+C_B=1$ as in the Cliff and Lorimer model [15]. There is no correction needed. If there is no absorption, no Coster-Kronig transition, no fluorescence,

$$\begin{aligned} f_A &= \frac{1}{1+K_{A-B}\frac{C_B}{C_A}} \\ &= \frac{1}{1+K_{A-B}\frac{(1-C_A)}{C_A}} \\ &= \frac{C_A}{C_A(1-K_{A-B})+K_{A-B}} \end{aligned} \tag{3.8}$$

and if $K_{A-B}\simeq 1$, then

$$C_A\simeq K_{A-B}f_A \tag{3.9}$$

Then, the ratio is proportional to the concentration of the element and the Cliff and Lorimer factor. On the other hand, if $C_A\rightarrow 0$, then equation 3.4 is rewritten :

$$C_A\simeq K_{A-B}\frac{\gamma_B}{\gamma_A}f_A \tag{3.10}$$

Once again, the ratio is proportional to the concentration, but the absorption effect must be included. The system can be solved in many ways, in cases of specific materials. The point is that it can be linked to the concentrations of the elements.

Figure 3–1 compares the line ratio and the k-ratio according to Castaing's principle. The standard is a pure Au specimen and the microanalyses are done at 4, 5, 10 and 15 keV, using four NIST standards, AuCu alloys (SRM 482). The straight line is the ideal trend where K_{A-B} is equal to 1. The ratio proposed here presents curves almost parallel to the straight ideal line, while the k-ratio do not.

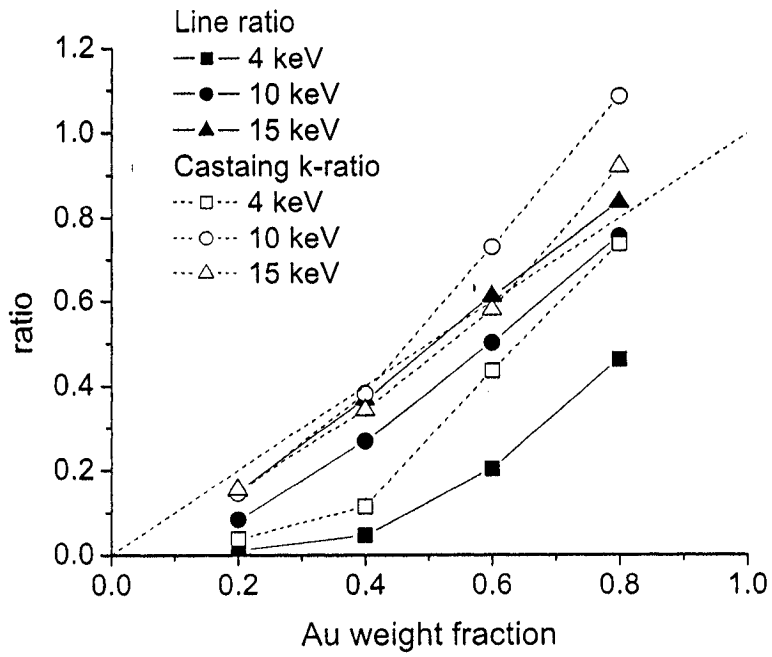

Figure 3–1: Comparison of the intensity ratio $I_{AuM}/(I_{AuM} + I_{CuL})$ with the k-ratio $I_{AuM\alpha}/I^0_{AuM\alpha}$ in a pure Au standard

Another aspect is the calculation of errors propagated by this method. There are many possible causes of errors, some are intrinsic to the method, some are dependent on microanalysis techniques and are found in any quantification method [46]. The

statistical error is directly related to the nature of x-rays. The measurement error is related to the inaccuracy of the electronics and counting process. The extraction error is caused by the method used to subtract the background. These three errors are difficult to evaluate independently, because they cannot be avoided. Only the statistical error [37, section 9.9] can be evaluated mathematically. The number of generated x-rays is completely random with time but has a fixed average value. The distribution of the number of measurements follows a Gaussian distribution with a certain standard deviation equal to $\sqrt{I}$ where I is the mean value. The standard deviation results from fluctuations that cannot be eliminated and therefore has a predictable and irreducible minimum. Thus the statistical error in percentage of total counts can be given as :

$$\Delta I = \frac{300}{\sqrt{I}} \tag{3.11}$$

where I is the measured signal at 99 % confidence level. Figure 3–2 shows an example of x-ray intensity of the $AuM\alpha$ and $CuL\alpha$ lines, as well as the statistical error on the signal. The bars indicate the statistical error calculated from equation 3.11. When an element has a low concentration and high absorption, then, usually, it emits low characteristic x-ray intensity, and the statistical error increases, as demonstrated in figure 3–2. For instance, at 30 keV, the $M\alpha$ peak of Au produces low intensity, and the statistical error goes up to 4 % for 40 % of Au. Therefore, the lower signal is related to higher beam energy (in relation to the ionization cross-section) and the smaller weight fraction.

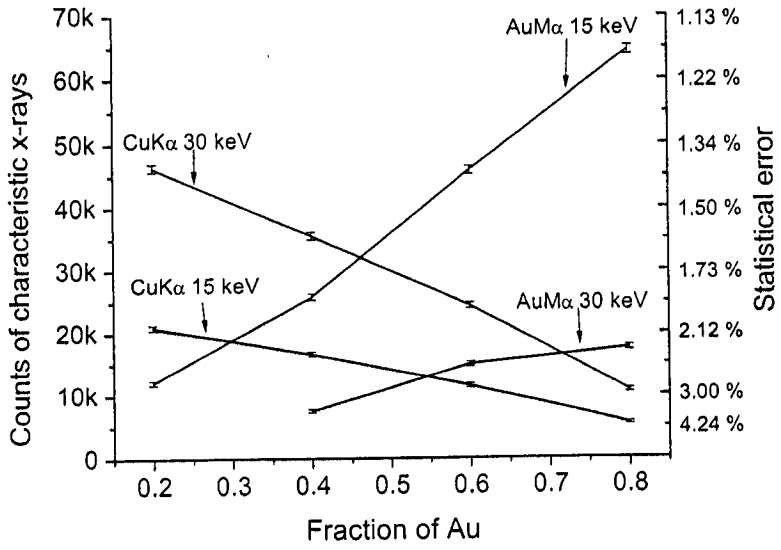

Figure 3–2: Extracted intensity of Au (Mα + Mβ) at 2.12 keV and Cu (Kα1 + Kα2) at 8.05 keV lines with the weight fraction of Au at 15 and 30 keV, statistical error 300 / $\sqrt{I}$ on the right hand scale

Another source, and the main, of error, which cannot be completely erased is the error due to background subtraction as explained in section 5.4 and detailed by Statham [106]. The deconvolution of overlapped peaks can also cause errors. The theoretical width, center, and relative height of the different peaks, may differ from the real values, and then introduce errors in deconvolution. Other types of errors are directly related to the method, and are due to the uncertainties in the physical models that affect the value of the ratio, such as the ionization cross-section, fluorescence yield, line ratio, mass-absorption coefficient that are not very well known for L- and M- subshells. Therefore any differences in the nominal values may affect the accuracy of the quantification. These last errors are not calculated in this work, so the analysis will be focused on the statistical error. Any error in the measurement of characteristic x-ray intensity is propagated to the determination of the calibration factor, and furthermore to the calculation of weight fraction. The derivative of the ratio permits the analysis of the propagation of errors from measured x-ray intensity through the equation $f(x) = x/(x+y)$:

$$\begin{aligned} \Delta f &= \frac{\partial f}{\partial x}dx + \frac{\partial f}{\partial y}dy \\ &= \frac{y}{(x+y)^2}dx - \frac{x}{(x+y)^2}dy \\ &= \frac{1}{(x+y)^2}\left(ydx - xdy\right) \end{aligned} \tag{3.12}$$

For the Cliff and Lorimer ratio, for the function $g(x) = x/y$:

$$\Delta g = \frac{1}{y^2}\left(ydx - xdy\right) \tag{3.13}$$

It is clear that when y, that is to say one of the characteristic x-ray intensities, decreases to 0, the propagated error diverges for the Cliff and Lorimer ratio, contrary to the line ratio in this work. The propagation of error is calculated as $\Delta f/f$, then :

$$\frac{\Delta f}{f} = \frac{1}{x(x+y)}(y\Delta x - x\Delta y) \tag{3.14}$$

This equation shows that conditions may exist where the error reaches an optimum. Although this relation is developed for a continuous function which describes a phenomenon, it is used later to roughly estimate the propagation of the errors, estimated from the standard deviation of measurements, as recommended by Heinrich [45]. Equation 3.13 applied to statistical error is given by:

$$\frac{\Delta f}{f} = \frac{300}{I_x(I_x+I_y)}(\frac{I_y}{\sqrt{I_x}} - \frac{I_x}{\sqrt{I_y}}) \tag{3.15}$$

And applied to the Cliff and Lorimer ratio, equation 3.13 with the statistical error is:

$$\frac{\Delta f}{f} = \frac{300}{I_x I_y}(\frac{I_y}{\sqrt{I_x}} - \frac{I_x}{\sqrt{I_y}}) \tag{3.16}$$

In a scanning electron microscope, using an energy dispersive spectrometer, the peak-to-background ratio is lower than in a transmission electron microscope. Therefore, the probability of introducing error in the evaluation of the characteristic x-ray is higher in a SEM. The formulation of this ratios thus permits the reduction of the propagation of error to the calculation of the composition as shown

in figure 3–3, which compares the propagation of the statistical error to the ratios AuLα/(AuLα+CuKα) (according to equation 3.15) and AuLα/CuKα (equation 3.16), in a cold field emission scanning electron microscope at 15 keV, for the AuCu standard alloy SRM482. The error, calculated by derivation of the ratio func-

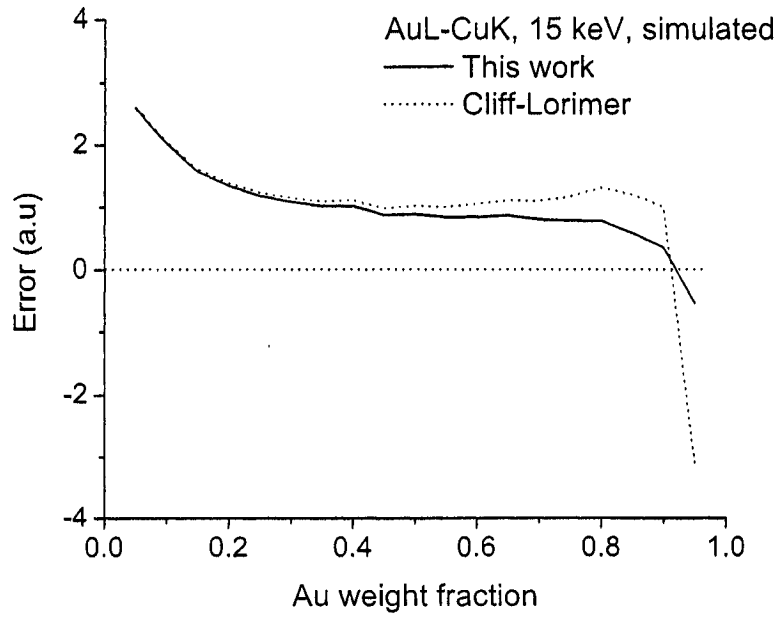

Figure 3–3: Comparison of the propagation of statistical error to the calculation of the ratio with the Cliff-Lorimer ratio and this work

tion, is consistently smaller in this work, especially at low concentration of the Cu. The error studied here is the statistical error, but the trend is valid for all errors in the process.

3.2 Insertion of a calibration factor in the ratio

As shown in section 2.4, ZAF correction cancels the fundamental parameters (equation 2.13), and therefore reduces the uncertainties about these parameters. In the method introduced here, some uncertainties remain, particularly concerning the detector efficiency and the accuracy of the fundamental parameters concerning x-ray generation. A calibration factor Λ is introduced into the definition of the ratio as follows, for a binary system:

$$\begin{aligned} f_A &= \frac{I_A^{th}}{I_A^{th} + \Lambda_{A-B} I_B^{th}} \\ f_B &= \frac{\Lambda_{A-B} I_B^{th}}{I_A^{th} + \Lambda_{A-B} I_B^{th}} \\ &= \frac{I_B^{th}}{I_B^{th} + \Lambda_{B-A} I_A^{th}} \end{aligned} \tag{3.17}$$

where f is the calculated ratio. The calibration factors Λ_{A-B} and Λ_{B-A} are related:

$$(\Lambda_{B-A})(\Lambda_{A-B}) = 1 \tag{3.18}$$

This Λ_{A-B} factor depends only on the physical parameters of the x-ray emission of the element and on the detector efficiency. In order to calculate Λ_{A-B}, a microanalysis is done on a binary specimen of known composition with two elements A and B. The experimental ratios f_A^{exp} and f_B^{exp} are calculated with measured x-ray characteristic intensities I_A^{exp} and I_B^{exp} as in equation 3.3. In order to estimate the calibration factor, the theoretical intensities of emitted x-rays I_A^{th} and I_B^{th} are calculated with a model of x-ray generation. The theoretical ratio f_A^{th} and f_B^{th} are calculated without a calibration factor, according equation 3.3. The calibration factor Λ_{A-B} is determined

as:

$$f_A^{exp} = \frac{I_A^{exp}}{I_A^{exp} + I_B^{exp}} = \frac{I_A^{th}}{I_A^{th} + \Lambda_{A-B} I_B^{th}}$$
$$f_A^{th} = \frac{I_A^{th}}{I_A^{th} + I_B^{th}} \tag{3.19}$$

Finally, the correction factor can then be expressed as the combination of the computed and measured x-ray characteristic intensities:

$$\Lambda_{A-B} = \frac{I_A^{th}}{I_B^{th}} \frac{I_B^{exp}}{I_A^{exp}}$$
$$= \frac{f_A^{th}}{1 - f_A^{th}} \frac{1 - f_A^{exp}}{f_A^{exp}} \tag{3.20}$$

The Λ_{A-B} factor for this binary system is calculated and used in any microanalysis involving the A-B system. The error of estimation of this factor is directly dependent on the error of determination of the intensities of the characteristic lines used for calibration:

$$\Delta\Lambda_{A-B} = \frac{f_A^{th}}{f_B^{th}} \frac{f_B^{exp}}{f_A^{exp}} \left(\frac{\Delta f_B^{exp}}{f_B^{exp}} - \frac{\Delta f_A^{exp}}{f_A^{exp}} \right) \tag{3.21}$$

Thus, the error of measurement of the intensity of lines linearly propagates to the calculation of the calibration factor. Special care must be taken for the estimation of this factor. However, since this factor is intended to correct uncertainties in physical models and microscope parameters, it can be calculated for any element periodically. This is one interesting feature of this method, which has the advantage of using real standards, to correct theoretical uncertainties, and the ease of the standardless

method, since the standards do not need to be analyzed for each quantitative x-ray microanalysis.

The correction factor was alleged to depend only on the microscope parameters and the characteristic energy of the photons involved. This is based on the hypothesis that the correction of the models is independent of the beam energy. The calibration factor can be related to the intensity ratio as follows :

$$\begin{aligned} \frac{I_B^{exp}}{I_A^{exp}} &= \Lambda_{A-B}\frac{I_B^{th}}{I_A^{th}} \\ &= \Lambda_{A-B}K_{A-B}\frac{F_B}{F_A}\frac{(1+T_{CK,B})}{(1+T_{CK,A})}\frac{\gamma_B}{\gamma_A}\frac{C_B}{C_A} \end{aligned} \tag{3.22}$$

Since all the parameters, except for the fluorescence correction F, the absorption term γ and the ionization cross-section, exclusively depend on the atomic numbers of elements A and B, and not on the beam energy, this equation can be rewritten as:

$$\frac{I_B^{exp}}{I_A^{exp}} = \Lambda_{A-B}\frac{\Pi_B}{\Pi_A}\frac{\sigma_A}{\sigma_A}\frac{F_B}{F_A}\frac{\gamma_B}{\gamma_A}\frac{C_B}{C_A} \tag{3.23}$$

where Π is a calculated parameter and is equal to:

$$\Pi = \frac{\varpi P\epsilon}{A}(1+T_{CK}) \tag{3.24}$$

and depends exclusively on the element and the excited line. The other term of the right hand side of the equation is dependent on the material and conditions of microanalysis. The Λ_{A-B} is exclusively dependent on the ratio of physical parameters of elements A and B only if there is no fluorescence in the specimen and if the $\varphi(\rho z)$ curve is independent of the specimen (low mass-absorption coefficient and density) or if it is known accurately. The ionization cross-section depends on the

beam energy, therefore if the theoretical shape is not accurate, the calibration factor may depend on the beam energy. A typical calibration element, Cu for instance, can be chosen to calculate the calibration factors for different elements. Standards with known concentrations of elements A and Cu and B and Cu are needed but the microanalysis can be done periodically, for example if icing of the EDS detector is suspected. The microanalyses are ideally performed at the same beam energy for all the specimens, in order to reduce the possible beam dependency of the factor. The energy of the characteristic lines can be chosen between 10 and 15 keV, typically when the detector efficiency is close to 1 or constant, above 1 keV (see figure 3–4). The calibration is unique for each microscope, since it includes uncertainties about

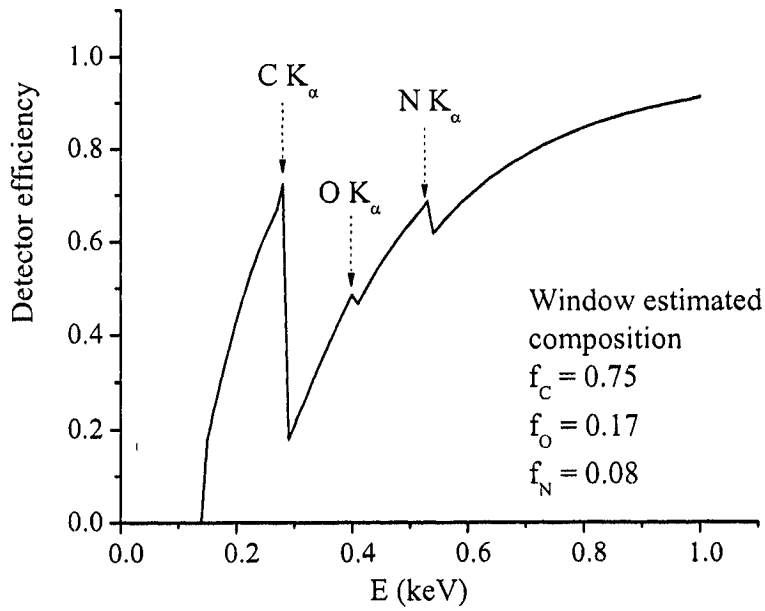

Figure 3–4: Calculated detector efficiency with current specifications

the detector efficiency, particularly for characteristic lines of energy below 3 keV approximately.

Thus, if the product $F\gamma = 1$ or is specimen independent, the calibration factor can be calculated for each element with respect to a common standard or a combination of elements which establishes the ratio for each couple :

$$\Lambda_{A-B} = \frac{\Lambda_{A-C}}{\Lambda_{B-C}} \tag{3.25}$$

where the two specimens are (A-C) and (B-C). The condition for γ to be specimen independent is that the difference in mass-absorption coefficient of C in (A-C) and in (B-C) are not very different, as well as the density.

3.3 Extension of the method to real materials

This method can be applied to any type of material, heterogeneous, rough, multilayers and particles in as much as there is a way to calculate the emitted x-ray intensities in these materials, for instance by Monte Carlo simulation which can treat almost all cases.

The method to calculate concentration can be either interpolation or iteration. Interpolation is easy for a binary system, since there is only one independent variable. For more than 2 elements, it may be more complicated. Another approach is iteration. From equations 3.3 and 3.4, the ratio for binary systems can be rewritten for the j^{th} iteration as:

$$C_A^j = \left(C_A + (1 - C_A) K_{A-B} \frac{F_B}{F_A} \frac{(1 + T_{CK,B})}{(1 + T_{CK,A})} \frac{\gamma_B}{\gamma_A} \right)^{j-1} f_A \tag{3.26}$$

For a multiple-component material, a calibration factor is needed for each component and the ratio is calculated:

$$f_i = \frac{I_i}{I_i + \sum_{j \neq i} \Lambda_{i-j} I_j} \tag{3.27}$$

where Λ_{i-j} is the calibration factor for the pair i-j.

In the case of a ternary material, for instance, there are three components A, B and C and three calibrations factors:

$$\begin{aligned} f_A &= \frac{1}{1 + \Lambda_{A-B}\frac{I_B}{I_A} + \Lambda_{A-C}\frac{I_C}{I_A}} \\ f_B &= \frac{1}{1 + \Lambda_{B-A}\frac{I_A}{I_B} + \Lambda_{B-C}\frac{I_C}{I_B}} \\ f_C &= \frac{1}{1 + \Lambda_{C-A}\frac{I_A}{I_C} + \Lambda_{C-B}\frac{I_B}{I_C}} \end{aligned} \tag{3.28}$$

with $\Lambda_{A-B}\Lambda_{B-A} = 1$, $\Lambda_{A-C}\Lambda_{C-A} = 1$ and $\Lambda_{C-B}\Lambda_{B-C} = 1$ in best conditions as explained in equation 3.25. This means that equations 3.28 are linked in the case that equation 3.25 is true. Moreover, it can be explained by the fact that $f_A + f_B + f_C = 1$ as explained by equation 3.25. Then:

$$\frac{I_B}{I_A} = \Lambda_{B-A}\frac{f_B}{f_A}\frac{I_C}{I_A} = \Lambda_{C-A}\frac{1 - f_A - f_B}{f_A} \tag{3.29}$$

For more than two elements, it is also suggested to proceed by calculations of a set of conditions, for a gradient of concentration of each component. Then, a surface can be obtained by interpolation, and the composition determined by a least square calculation. Another approach is the iterative determination of concentration. For

instance, the starting concentration is set as 1/n, where n is the number of elements and calculations similar to equation 3.27 are iterated.

Chapter 4
Calculation of theoretical emitted x-ray intensity

The emitted characteristic x-ray intensity for element i is calculated as follows (see equation 2.6):

$$I_i = n_E \frac{\Omega}{4\pi} \frac{N_A C_i}{A_i} \epsilon_i \sigma_i \varpi_i P_i (1+\delta_i)(1+T_{CK,i}) \int_0^\infty \varphi(\rho z) e^{-\chi_i \rho z} d(\rho z) \qquad (4.1)$$

The physical parameters that must be evaluated from literature are the ionization cross-section σ_i (see section 4.1), the fluorescence yield ϖ_i, the line fraction P_i, the fluorescence correction $(1+\delta_i)$ and the Coster-Kronig correction coefficient $(1+T_{CK,i})$ (see section 4.2). The $\varphi(\rho z)$ curve is calculated with all these parameters, as explained in section 4.5.

4.1 Ionization cross-section

Most of the characteristic x-rays are generated by interaction with the incident electrons. This is described essentially by the ionization cross-section $\sigma_l(E)$ which is related to the probability of ionizing a certain inner-shell of an atom.

In fact, there are many obstacles in the determination of ionization cross-sections either by experimental measurements or calculations, particularly for conditions close to the ionization edge [67] because the plane-wave Born approximation is no longer valid. Near the threshold, the atomic field causes distortion of the wave function of the electron. There are many semi-empirical models but they usually depend on the system and method of measurement. On the other hand, the completely theoretical

approach is very time-consuming. For instance, Rez calculated the ionization cross-section with the plane wave Born approximations modified by the Ochkur expression for exchange [87, 88, 89]. The many different approximations cause a large scattering of results. In some cases the uncertainties can reach 50% and the cross-section discrepancies are of the order of the cross-section values [60]. Moreover, the experimental measurement of cross-section has been continuously ongoing for decades, and the database is not yet complete, particularly for the L- and M- shells. For instance, only values of the L-shell ionization cross-sections of Ar, Kr, Xe, Ge, Au, W and Pt [67] were reported in 2004, and this is worse for the M-shell. In 2001, Joy [55] found no measurements for M-shell ionization cross-sections. Therefore the amount of data available for the other generation parameters is small for K-shells, negligible for the L-shells, and all but non-existent for the M- and higher shells. Furthermore, even extremely careful measurements cannot be expected to give accuracy better than 10 % for the K-shell ionization cross-section [60], and it is worse for higher-level shells. However, the discrepancy of measurements is usually much larger than this ideal minimum.

The ionization cross-section depends on the atomic number and the energy of the incident electron, as Bethe established in the 30's [7, 8]. $\sigma(E)$ is the ionization cross-section in (cm^2) given by:

$$\sigma(E) = 6.51 \times 10^{-20} \frac{n_s b_s}{U E_c^2} \ln_e(c_s U) \tag{4.2}$$

where n_s is the number of electrons in a shell or subshell, b_s and c_s are constants for a particular shell, E_c is the critical ionization energy and U is the overvoltage.

The overvoltage is defined as the ratio of the instantaneous beam energy E and the ionization energy of the shell E_c:

$$U = \frac{E}{E_c} \tag{4.3}$$

Powell [80, 81] noted that, even if many models have been developped and measurements made for the K-line ionisation cross-section, discrepancies are important. He recommended that for the K line, $b_K = 0.9$ and $c_K = 0.65$ for the overvoltage range $4 \leq U \leq 25$. It appears to be very difficult to estimate a general formula that would be convenient for any peak family and any atomic number and any overvoltage. In order to have a better approximation of the cross-section, it has been suggested that it depends on a power of the overvoltage:

$$\sigma \propto \frac{\ln(U)}{U^m E^2} \tag{4.4}$$

The main difficulty is the evaluation of the constant m, which may or may not be dependent on the atomic number.

Another used formulae has been given by Gryzinski [40]:

$$Q_l(E) = \frac{\sigma_0 z_{nl}}{E_l^2} \frac{(\frac{U-1}{U+1})^{3/2}}{U} 1 + \frac{2}{3}(1 - \frac{1}{2U}) ln(2.7 + (U-1)^{1/2}) \tag{4.5}$$

where $\sigma_0 = 6.5610^{-14} eV^2 cm^2$ and z_{nl} the number of ionization of the ionized l shell. The ionization cross-section are systematically lower than experimental measurements by 10 to 15 % [80]

The most used semi-empirical model for ionization cross-section was developed by Casnati et al. in 1982 [12] for the K-shell. This was a semi-empirical expression based on the Bethe expression and experiment for atomic numbers between 6 an 79

and an overvoltage between 1 and 20. The cross-section is expressed as follows:

$$\begin{aligned} \sigma_K &= n_K a_0^2 R \left(\frac{I_0}{I_K}\right) \psi\phi \frac{lnU}{U} \\ \psi &= \left(\frac{I_K}{I_0}\right)^{d_0+d_1/U+d_2/U^2} \\ \phi &= b_0 e^{\frac{b_1}{U}+\frac{b_2}{U^2}} \end{aligned} \tag{4.6}$$

where n_K is the number of electrons in the subshell and with:

$$\begin{aligned} d_0 &= -0.0317, d_1 = 0.3160, d_2 = -0.1135 \\ b_0 &= 10.57, b_1 = -1.736, b_2 = 0.317 \end{aligned} \tag{4.7}$$

determined from tabulated measured values for Kα peaks. Compared to Auger Electron Spectroscopy measurements, the Casnati model was proven to give consistent results for K, L and M lines ionization at high overvoltage [100]. Therefore n_s is changed as in table 4–1 to apply Casnati ionization cross-sections to L- and M-shells ionization.

Table 4–1: Table of electron subshells

Name line	Number of free electrons
K	2
LI	2
LII	2
LIII	4
MI	2
MI	2
MIII	4
MIV	4
MV	6

More recently, Salvat et al. [93] have developed a new model for ionization cross-section for their Monte Carlo program Penelope) based on the atomic generalized oscillator strength $df_i(W,Q)/dW$(GOS) (W is the energy loss due to the inelastic interaction and Q the recoil energy), which completely determines the effect of inelastic interactions on the projectile, within the Born approximation. The recoil energy is equal to the energy of an electron in which the GOS can be represented as a surface over the (Q, W) plane, and which is called the Bethe surface. The physics of inelastic collisions is determined by only a few features of the Bethe surface. Therefore relatively simple GOS models describe quite realistically the inelastic interactions [91]. The inner-shell ionization is considered as an independent interaction process that does not affect the state of the incident electron. For the simulation of the K-, L- and M-subshells (with ionization energies above 200 eV), the total ionization cross-section is obtained from an optical-data model of the GOS (see Mayol et al. [64]). The GOS is related to the photoelectric cross-section $\sigma_{ph,i}(Z,W)$ as follows:

$$\frac{df_i(W)}{dW} = \frac{m_e c}{2\pi^2 e^2 \hbar}\sigma_{ph,i}(Z,W) \tag{4.8}$$

where m_e is the electron mass, c the velocity of light, e the electron charge and $\hbar$ the Planck's constant. Z is the number of electrons in ground state in the target. W is the energy loss of the electron. In order to compute the inner-shell ionization $\sigma_{si,i}$ for electron of energy E, the differential cross-section is first calculated as :

$$\begin{aligned}\frac{d\sigma^{\pm}_{si,i}}{dW}(E) &= \frac{2\pi e^4}{m_e v^2}\left\{\frac{df_i(W)}{dW}\frac{1}{W}\left[\ln\left(\frac{W}{Q_-}\frac{Q_- + 2m_e c^2}{W + 2m_e c^2}\right) + \ln\left(\frac{1}{1-\beta^2}\right) - \beta^2\right]\right. \\ &\left. + \left(Z_r + \int_{U_i}^{W}\frac{df_i(W')}{dW'}dW'\right)\frac{1}{W^2}F^{(\pm)}(E,W)\right\}\end{aligned}$$

$$\times\Theta(W - U_i)\Theta(W_{max} - U_i) \tag{4.9}$$

where v is the electron velocity, Q_- is the minimum recoil energy, β is equal to $(v/c)^2$, Z_r is calculated from the number of electrons in the active shell Z_i:

$$Z_r = Z_i - \int_{U_i}^{\infty} \frac{df_i(W')}{dW'} \tag{4.10}$$

$F^{(-)}(E, W)$ is the Møller factor:

$$F^{(-)}(E, W) = 1 + \left(\frac{W}{E - W}\right)^2 - \frac{W}{E - W} + a\left(\frac{W}{E - W} + \frac{W^2}{E^2}\right) \tag{4.11}$$

$F^{(+)}(E, W)$ is the Bhabha factor:

$$F^{(+)}(E, W) = 1 - b_1\frac{W}{E} + b_2(\frac{W}{E})^2 - b_3(\frac{W}{E})^3 + b_4(\frac{W}{E})^4 \tag{4.12}$$

where a and b_i factors are functions of the $\gamma = \sqrt{1 - (v)^2}$ factor of relativity. $\Theta(x)$ is the step function.

Salvat et al. [93] tabulated the ionization cross-sections and made them available with their Penelope program for K and L lines. Figure 4–1 compares the Salvat K-shell ionization cross-section with Casnati's model [12], which agree quite accurately with the experimental measurements as shown by the comparison with a set of values collected in the literature by David C. Joy [54] and shown in figure 4–1. The scattering of experimental measurements makes hazardous the choice of the best model.

During this project, a method was proposed to estimate the ionization cross-section for the L lines. Llovet et al. [61] recently proposed a general formula for the relative subshells ionization cross-section since its shape is alleged to be independent

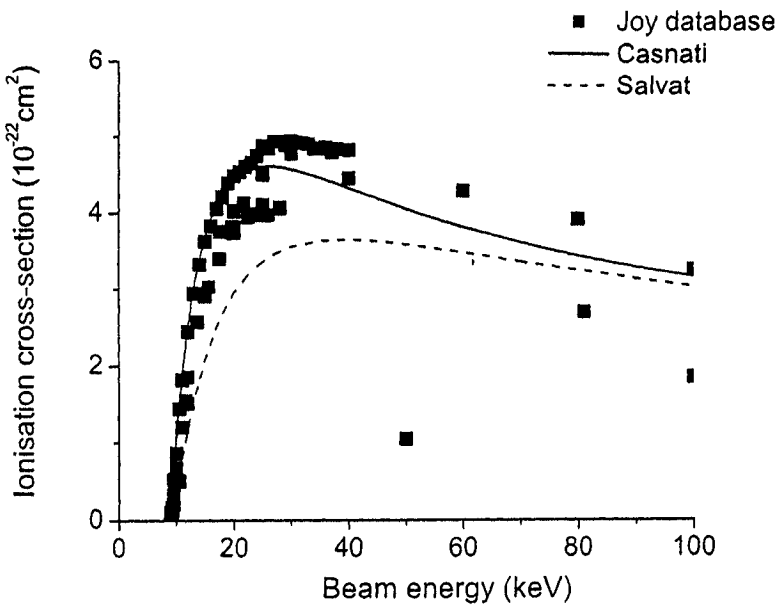

Figure 4–1: Comparison of Casnati [12], Salvat [93] and measured [54] ionization cross-section for pure Cu K shell

of the atomic number:

$$\frac{\sigma}{\sigma_{max}} = \left(a_1 + \frac{a_2}{U}\right) \frac{1}{U^{a_3}} ln(U) \tag{4.13}$$

where U is the overvoltage, $a_1 = 2.56$, $a_2 = 0.14$ and $a_3 = 0.97$ are parameters determined from a numerical fit of all the measured data. For the L subshells, Scofield ionization cross-sections [99] are interpolated by an exponential fit. Then the ionization cross-section at 50 keV (high over-voltage and lower value given by Scofield) is calculated. Then, from equation 4.13 the maximum σ_{max} is calculated. Absolute ionization cross-sections are calculated from this value and equation 4.13. Values for LIII subshells are drawn in figure 4–2 which compare the ionization cross-section for AuLIII with the present work, Casnati [12] and Salvat [93] models. Joy [55] made an exhaustive review of measurements of x-ray ionization cross-section presented by the symbols. For AuLIII, he noted five different series of measurements [90, 38, 22, 39, 96]. The scattering of experimental data reaches 400 % at the maximum, therefore it is difficult to predict the most accurate model, particularly at the beam energy concerned in a scanning electron microscope, below 30 keV. The model developped in this work overestimates the ionization cross-section above 20 keV, probably due to the inaccuracy of Scofield ionization cross-section at 50 keV. Salvat's model was preferred since it is developped for L-subshells contrary to Casnati's equations. The shape of Casnati and Salvat ionization cross-section is not the same in respect with the photon energy.

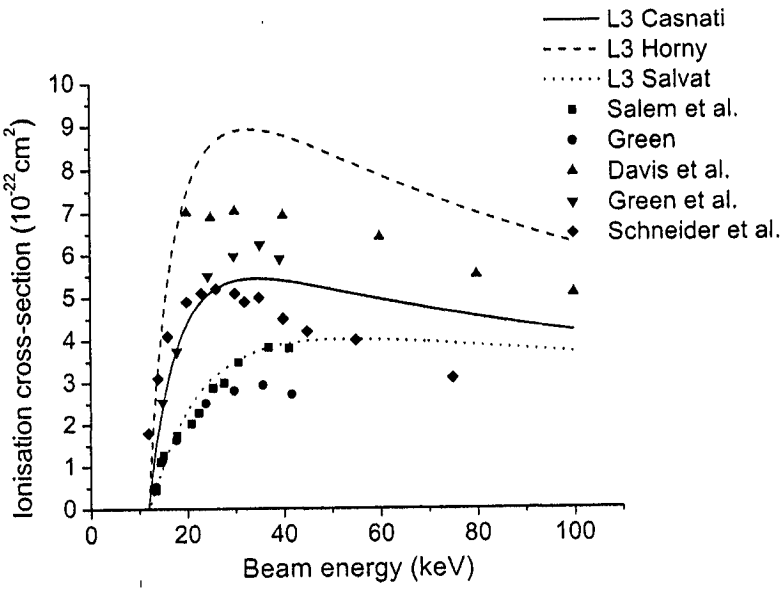

Figure 4–2: Compared ionization cross-section for Au LIII by this work, Casnati's [12] and Salvat's [93] models, and with measurement collected in Joy's database [54]

Figure 4–3 shows the difference between the Casnati and Salvat models for the MV subshells of Au. Future works should include Salvat M-shells ionization cross-sections, which are in preparation. It is however interesting to observe the 25 % of error, which is not so bad, between the Casnati and Salvat ionization cross-sections for M shells, when it is remembered that the Casnati model is a semi-empirical model developed for K-shell ionization.

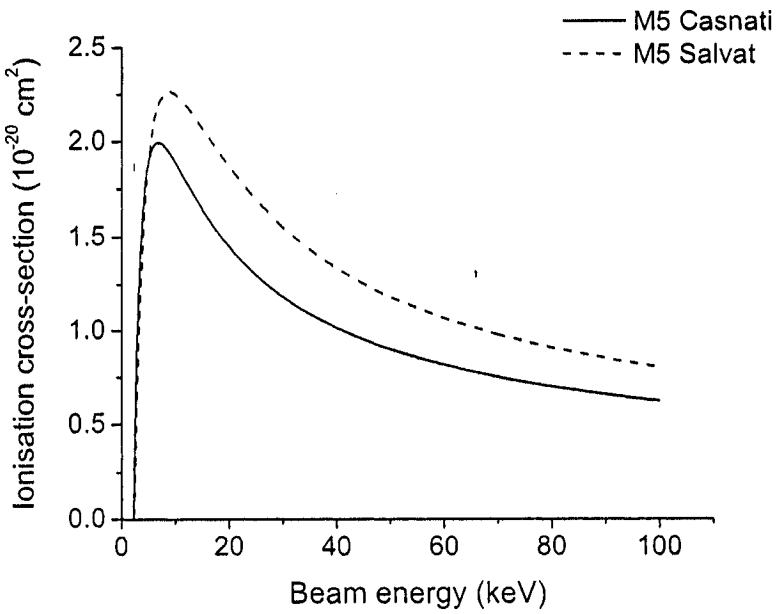

Figure 4–3: Compared ionization cross-sections for Au MV by Casnati's [12] and Salvat's [93] models

Different ionization cross-sections are used here to evaluate the independency of the method regarding the different models used. That is why two different methods have been arbitrarily chosen, one semi-empirical with a proven reliability (Casnati)

Table 4–2: Table of generated x-ray transitions and characteristic lines names

Line name	Transitions	Line name	Transitions
$K\alpha 1$	K-L3	$L\alpha 1$	L3-M5
$K\alpha 2$	K-L2	$L\alpha 2$	L3-M4
$K\beta 1$	K-M3	$L\beta 2$	L3-N4,5
$K\beta 2$	K-N2,N3	$L\beta 5$	L3-O4,5
$K\beta 3$	K-M2	$L\beta 6$	L3-N1
$L\beta 3$	L1-M3	Ll	L3-M1
$L\beta 4$	L1-M2	$M\gamma$	M3-N5
$L\gamma 3$	L1-N3	M3N1	M3-N1
$L\gamma 4$	L1-O2,3	M3N4	M3-N4
$L\beta 1$	L2-M4	M3O4	M3-O4
$L\gamma 1$	L2-N4	M3O5	M3-O5
$L2N1$	L2-N1	$M\beta$	M4-N6
$L\gamma 6$	L2-N1	$M\alpha$	M5-N6,7
$L\eta$	L2-M1	$M\zeta$	M5-N3

and the other one which is new and completely calculated according the most recent knowledge (Salvat).

In this work, nine subshells are simulated : K, LI, LII, LIII, MI, MII, MIII, MIV and MV. Most of the characteristic lines are represented by these subshells as shown in table 4–2. The choice has been made to use the Salvat ionization cross-section [93] for the K and L lines, and the Casnati [12] K-shell semi-empirical model adapted for the M lines, which was the only one available at this time.

4.2 Main x-ray emission parameters

As explained at the beginning of the section, there is no exhaustive description of any of the physical parameters, which are empirical, semi-empirical or totally theoretical. Since the systematic errors are corrected by a calibration factor in the method presented here, these parameters need to follow a correct shape but not necessarily have the exact absolute value. Moreover, the only way to estimate the different parameters consists of measuring the characteristic x-ray intensity, and then using values for all the parameters except the one to be determined, from equation 4.14:

$$I = n_E \frac{\Omega}{4\pi} \frac{N_A C_i}{A_i} \epsilon_i \sigma_i \varpi_i P_i (1 + \delta_i)(1 + T_{CK,i}) \int_0^\infty \varphi(\rho z) e^{-\chi_i \rho z} d(\rho z) \qquad (4.14)$$

The multiplication of the different parameters makes the separation of the parameters difficult. That is why experimental determination of these parameters usually shows wide discrepancy, depending on the methodology and the parameters used.

One of the first parameters is the fluorescence yield ϖ which determines the probability of generating a characteristic photon or an Auger electron. Many articles present different values of fluorescence yields, from purely theoretical to completely empirical. The first author to establish a complete review was Bambynek in 1972 [2] who compared theoretical and experimental values for fluorescence yield and Coster-Kronig transition probabilities. He proposed tables of recommended values, by refinement of theoretical approaches and comparison of experimental techniques. Experimental information is confined mostly to the K and L subshells. Some other authors recalculated the values later. In particular, Krause [57] made semi-empirical

calculations. Chen [17] worked on a Dirac-Hartree-Slater model. Puri [82] made Dirac-Hartree-Slater calculations for fluorescence yield and Coster-Kronig transition factors. Tawara [108] and Hubbel [51] worked on average L subshells fluorescence yield, not useful for this work. Fluorescence yields were measured for some elements [65, 75, 28, 11] and produced variable agreement with each other. In the most recent work, Campbell [11] compared the semi-empirical tabulation by Krause [57] and calculations by Dirac-Hartree-Slater predictions [82]. His recommended values are used in this work, for the three L subshells. Since any method of measurements has its own drawbacks, Campbell's database was chosen, however the differences were not huge, from 10 to 15 %, compared with the other measurements as shown in figure 4–4 which compares the fluorescence yield for the L3 subshell of Au for different authors.

For the M subshells, the only exhaustive values found in the literature were in a paper by McGuire [66] for the five M-subshells and by Chen et al. [18] for the MI, MII and MIII subshells. McGuire used an approximate Hartree-Slater wave function while Chen gave values calculated by the relativistic theory (Dirac-Hartree-Slater wave functions) for ten elements with atomic numbers $67 \leq Z \leq 95$. Puri [83] compared these two methods with his experimental results and showed that the average fluorescence yields are both in quite good agreement with the measurements for $71 \leq Z \leq 92$ as shown in figure 4–5. Values tabulated by Chen [18] were chosen for this work for the MI, MII and MIII subshells, and by McGuire for the MIV and MV subshells.

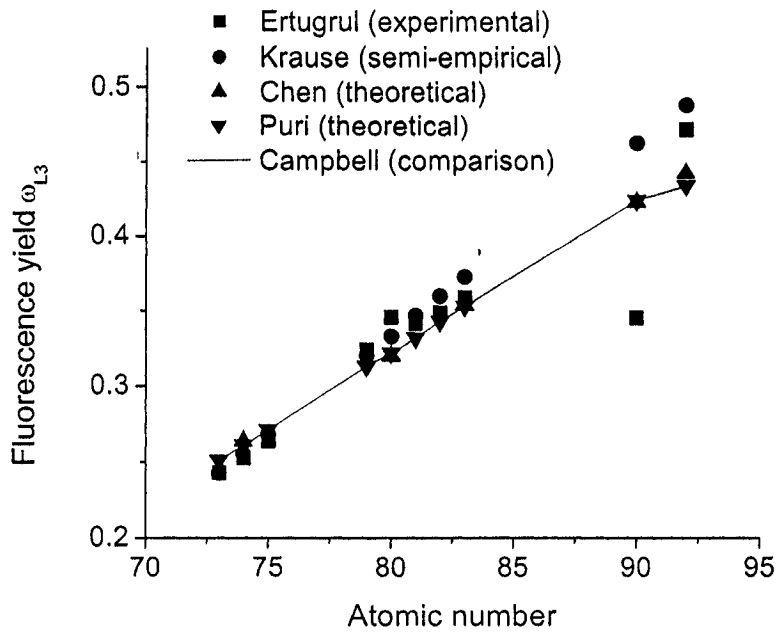

Figure 4–4: Comparison of different fluorescence yields for the LIII subshell: Ertugrul [28], Krause [57], Chen [17], Puri [82], Campbell [11]

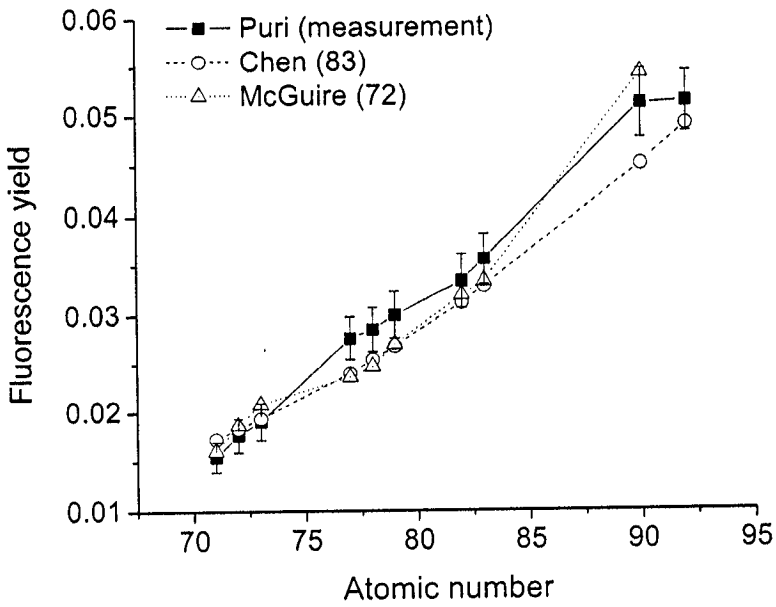

Figure 4–5: Comparison of average fluorescence yields for the M-subshells : experimental measurements [83], and calculations by Chen [18] and McGuire [66]

The x-ray transition probabilities are related to the emission of a specific line when a subshell is ionized, for instance the probability of emitting an Lα photon when the L3 subshell is ionized (see table 4–2). For the K lines, the values are taken from the work of Schreiber et al. [97]. For the L lines, Scofield [98] established a theoretical list of transition probabilities. In order to take into account all the possible atomic numbers (21 atomic numbers tabulated from Argon (18) to Plutonium (94)), polynomial or exponential interpolation of 1^{st} to 5^{th} orders have been done. The line transition probabilities are given relative to the major line for each subshell, as $L\alpha 1$ for the L3 subshell, $L\beta 1$ for L2 and $L\beta 3$ for L1. Depending on the shape of the curve, the type and order of the interpolation has been chosen in order to get the lowest R^2 correlation coefficient with the best accuracy. Figure 4–6 shows an example of interpolation for the $L\alpha 2$ line ratio with respect to the $L\alpha 1$, for the LIII subshells. The ratio is then equal to :

$$\begin{aligned} P_{L\alpha 1} &= \frac{1}{1 + f_{L\alpha 2} + f_{L3N1} + f_{Ll} + f_{L\beta 2} + f_{L3O1}} \\ P_{L\alpha 2} &= \frac{f_{L\alpha 2}}{1 + f_{L\alpha 2} + f_{L3N1} + f_{Ll} + f_{L\beta 2} + f_{L3O1}} \end{aligned} \tag{4.15}$$

where f are here the absolute rate of line transition.

The calculated values are interpolated by a third order polynomial with a determination factor R^2:

$$\begin{aligned} P_{L\alpha 2} &= 0.11933 - 2.73128 \times 10^{-4} Z + 3.88028 \times 10^{-6} Z^2 - 1.66989 \times 10^{-8} Z^3 \\ R_2 &= 0.97181 \end{aligned} \tag{4.16}$$

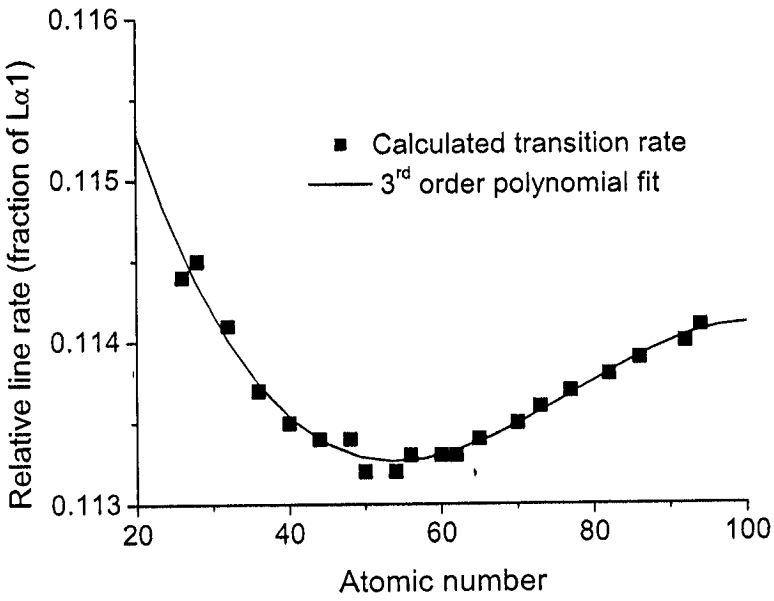

Figure 4–6: Calculated and interpolated probabilities of radiative transition [98] for the Lα2 line in fraction of Lα1 line

For the M lines, the transition probabilities have been calculated from the work of Chen et al. [19] who gave the calculated probability of radiative transition of filling a subshell from another subshell. These values (in atomic units) are given for 10 atomic numbers ranging from Cadmium (48) to Uranium (92) and the interpolations have been done as for the L lines described above. However only polynomial fit up to the third order has been needed as shown in figure 4–7, for the Mα line (transition MV-NVI).

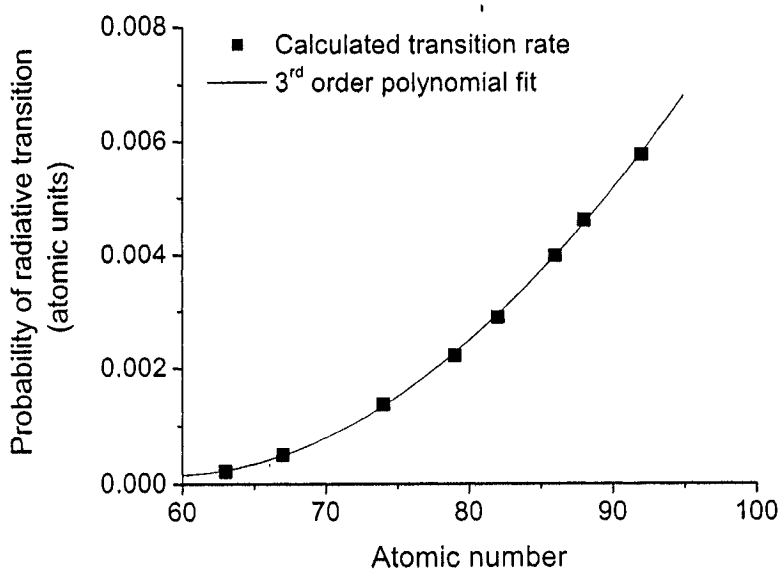

Figure 4–7: Calculated and interpolated probabilities of radiative transition [19] in atomic units for the Mα line (MV-NVI)

The symbols are the calculated values with Dirac-Fock wave functions. The line is the interpolated 3^{rd} order function with the coefficient of determination R^2:

$$\begin{aligned} P(Z) &= 0.02224 - 7.87076 \times 10^{-4} Z + 7.67378 \times 10^{-6} Z^2 - 1.15275 \times 10^{-8} Z^3 \\ R^2 &= 0.99962 \end{aligned} \tag{4.17}$$

The main emitted line for each subshell is $M\alpha$ for the MV subshell, $M\beta$ for the MIV and $M\gamma$ for the MIII. No line is calculated for the MII and MI subshells, because of the low fraction of lines, below 0.01 % of the Mα line [19].

In certain cases, a non-negligible fraction of the characteristic x-rays is generated by other mechanisms, such as Coster Kronig radiationless transition or fluorescence. These transitions are radiationless and occur when a vacancy jumps between the sub-shells of a specific shell and emit an x-ray. For instance, an LI vacancy can jump to the LIII subshell and the de-excitation energy may free a MIV electron. Coster-Kronig transition occurs on L and M shells only. For this transition to be possible, the ejected electron must obey the following for the previous case [85]:

$$E(L_x) - E(L_y) > E(M_z) \tag{4.18}$$

where E is the energy of the x, y and z subshells. In the above example, $L_x = LI$, $L_y = LIII$ and $M_z = MIV$. That means a vacancy from the x level jumps to the y level, emitting a photon from the z level. The probability of transition is given by the so-called Coster-Kronig yield. Both analytical [69] and emiprical [2] methods have been proposed to estimate these values. To that effect, the possibility

of intershell transitions is added, as shown by Merlet [67]. Most of time, the Coster-Kronig transition factor is calculated with the fluorescence yield, since these two elements are intimately related. For instance, to calculate the intensity emitted by LIII subshell ionization, the emission is calculated as follows:

$$T_{CK} = n_{KL3}\frac{\sigma_K}{\sigma_{L3}} + (f_{13} + f_{12}f_{23})\frac{\sigma_{L1}}{\sigma_{L3}} + f_{23}\frac{\sigma_{L2}}{\sigma_{L3}} \tag{4.19}$$

where n_{KL3} is the intershell probability of the line K to ionize the lines LIII, the f_{ij} terms are Coster-Kronig transition factors for the different L-subshells and σ_K, σ_{L1}, σ_{L2} and σ_{L3} are the subshell ionization cross-sections. As for all the other physical parameters, there are few exhaustive lists of values for Coster-Kronig factors. For this work, the intershell probabilities for K, L and M lines are taken from Bambynek [2] who calculated these values for all concerned atomic numbers. The Coster-Kronig transition factors for L lines and all elements are taken from the work of Campbell [11] who presented a complete table for all concerned atomic numbers as shown in figure 4–8 for the f_{12} parameter of the AuL3 subshell. The scattering of the measured data complicates the choice of a reference database. However, to ensure continuity of the values, the theoretical values recommended by Campbell (Dirac-Hatree-Fock method) were used in this work.

For the M lines, the only exhaustive work was done by Chen et al. [18] for the MI, MII and MIII-subshells and by McGuire [66] for the MIV and MV-subshells. The values for all the atomic numbers are obtained by polynomial interpolation of 10 calculated values as shown in figure 4–9 for the f_{45} Coster-Kronig coefficient from McGuire.

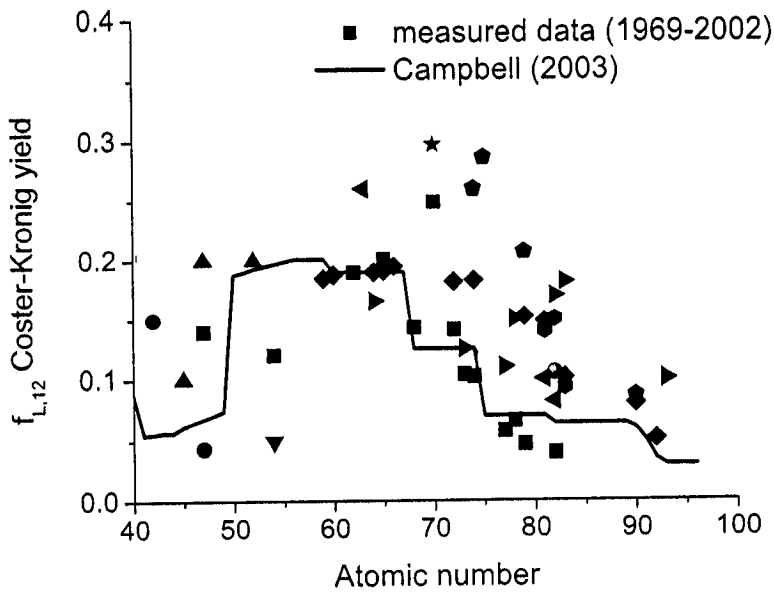

Figure 4–8: Measured and calculated values [11] of f_{12} for the AuL3 subshell

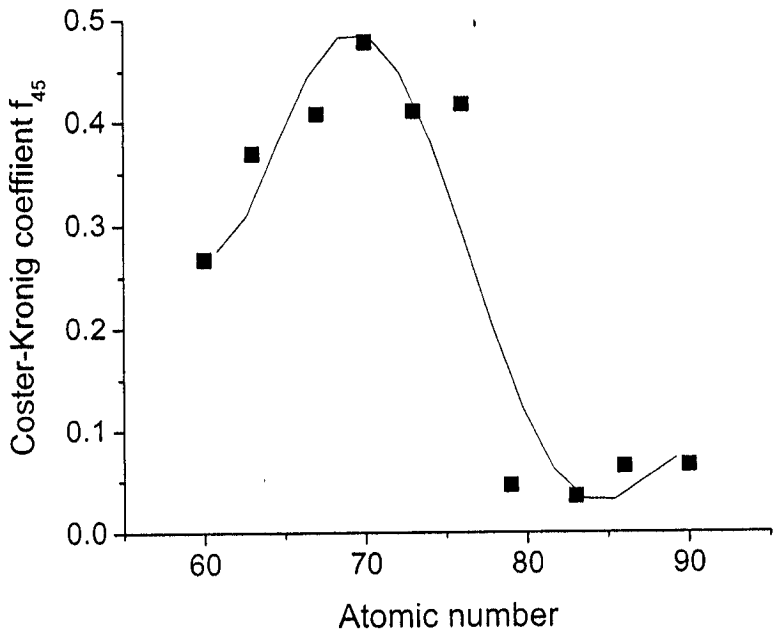

Figure 4–9: Interpolation of the Coster-Kronig factor [66] f_{45} for the M-subshell

The polynomial regression is done to the fifth order with a determination factor R^2 of 0.89006:

$$\begin{aligned} Y &= 1938.82613 - 131.58061Z + 3.54305Z^2 - 0.04731Z^3 \\ &+ 3.13309 \times 10^{-4}Z^4 - 8.23559 \times 10^{-7}Z^5 \end{aligned} \tag{4.20}$$

4.3 X-ray mass-absorption coefficient

Another physical parameter is the mass-absorption coefficient. This function is dependent on the energy of the photon and the density (and atomic number) of the material. There are a large uncertainty on mass-absorption coefficient for low energy x-rays, typically below 1 keV [52] as shown in table 4–3.

Table 4–3: Estimated uncertainties in photoionization cross-section component in SEM conditions [52]

Photon energy range	Estimated error (%)
10 eV - 100 eV	1000
100 eV- 0.5 keV	100-200
0.5 keV- 1 keV	10-20
1 keV- 5 keV	5
5 keV - 100 keV	2

Heinrich [41], [44], and [42] established different tabulated values of absorption coefficients. Henke [47] noticed problems for low energy photons and proposed corrected tables as compared in figure 4–10 for the Mα line of Au. Moreover, large uncertainties due to old measurements and calculations with rudimentary computers [52, 50] would require the use of a completely reviewed database.

Table 4–4 presents the coefficient for Au, Cu and Ag used as standards in the validation of the method from the database established by Golstein et al. [37]. Mass-absorption coefficients are higher for low energy x-ray characteristic peaks, so the effect is more important for these lines as shown in figure 4–11. The effect of mass-absorption coefficient is calculated from a small layer. The elemental generated x-ray intensity dI is absorbed in the small layer of thickness dx according to the equation:

$$dI = -\mu I dx$$

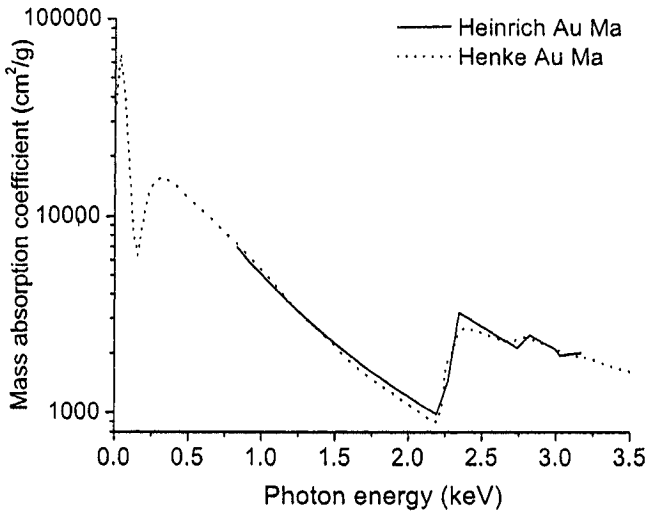

Figure 4–10: Comparison of mass-absorption coefficient for Au by Heinrich [44] and Henke [47]

Table 4–4: Goldstein [37] mass-absorption coefficient (cm^2/g) of Au and main characteristic x-ray lines in the AuCu and AuAg alloys

	Au	Cu	Ag
Au Lα	127.3	238.9	131.3
Au Mα	1145	1955	1225
Cu Kα	52.4	209.3	
Cu Lα	5774	1582	
Ag Lα	2141		6517

$$\begin{aligned} \frac{dI}{I} &= -\mu dx \\ ln\left(\frac{I}{I_0}\right) &= -\mu x \\ I &= I_0 e^{-\frac{\mu}{\rho}\rho x} \end{aligned} \tag{4.21}$$

The absorption parameter in figure 4–11 is multiplied by the x-ray generated intensity $I_{generated}(z)$ to obtain the emitted intensity. This parameter is given by Beer's law at a given depth z:

$$I_{emitted}(z) = I_{generated}(z) \cdot e^{-\chi\rho z} \tag{4.22}$$

where χ is defined in section 2.3.

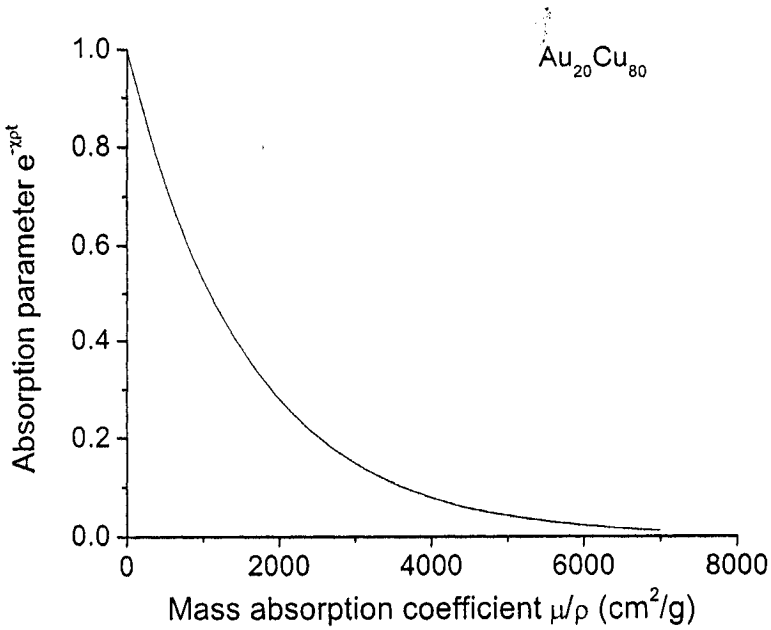

Figure 4–11: Mass-absorption coefficient effect on the x-ray emission in $Au_{20}Cu_{80}$ standard at 500 nm of depth with a take-off angle of 30 degrees

From figure 4–11, the higher is the mass-absorption coefficient, the lower is the parameter, therefore the emitted intensity is much lower than the generated intensity. High absorption coefficient is due to high average atomic number.

The geometry used for the energy dispersive spectrometer is given in appendix A.

4.4 X-ray fluorescence correction

If an x-ray traveling in the material has an energy higher than any critical ionization energy of an atom, it may cause fluorescence, that is to say ionize an atom making it emit another x-ray. There are two types of fluorescence, caused either by a characteristic photon or by bremsstrahlung. Typically, the most significant is the characteristic fluorescence which is modeled here. Fluorescence significantly occurs when the energy of the photon is close to the ionization energy of the subshell. Reed [84] proposed a simple and efficient modeling. When fluorescence occurs, the effect is calculated from the total intensity emitted by the atom B that fluoresces a subshell of element A. The intensity of radiation of element A produced by fluorescence by element B I^f_{AB} is linked to the electron-generated intensity of radiation from element A I_A [37]:

$$I^f_{AB} = 0.5 \cdot C_B \cdot \frac{A_A}{A_B} \cdot \left(\frac{U_B - 1}{U_A - 1}\right)^{1.67} \cdot \frac{(\mu/\rho)^B_A}{(\mu/\rho)_B} \cdot \frac{r_A - 1}{r_A} \cdot \varpi_B \cdot I_A \left[g(x) + g(y)\right] \quad (4.23)$$

where C_A is the concentration of the atom A, $(\mu/\rho)^B_A$ the mass-absorption coefficient of the element A for the B radiation, $(\mu/\rho)_B$ the absorption of the specimen for the B radiation, g(x) and g(y) describe the absorption of the fluoresced x-ray.

$$g(u) = \frac{ln(1+u)}{u} \quad (4.24)$$

The variables x and y are:

$$\begin{aligned} x &= \frac{(\mu/\rho)_A}{(\mu/\rho)_B} \csc\psi \\ y &= \frac{\sigma}{(\mu/\rho)_B} \end{aligned} \quad (4.25)$$

where $(\mu/\rho)_A$ is the absorption of the specimen for the A radiation and σ the Lenard absorption coefficient [37]. If only a line of a family excites another subshell, equation 4.23 must be multiplied by the transition probability of this line.

The fraction absorbed by element A is $C_A((\mu/\rho)_A^B/(\mu/\rho)_B)$. From this intensity, a fraction $(r_A-1)/r_A$ is absorbed by shell ionization of atom A, where r_A characterizes the jump at the aborption edge of the mass-absorption coefficient. The absorption edge can be approximated as 0.88 for a K line and 0.75 for a L line although it slightly depends of the atomic number [1] And finally a fraction ϖ produces a characteristic x-ray. This is a simple approach for the modeling of the fluorescence effect. In fact, fluorescence is much more complex because it a cascade phenomenon. The most comprehensive method of calculation is a cascade tridimensional model, but it generates many calculations and is even uncontrolable.

The coefficient δ in equation 2.6 is equal to:

$$\delta = \frac{I_{AB}^f}{I_A} \tag{4.26}$$

Then if there is fluorescence of the K shell of A by the Kβ1 x-ray of B, for instance, the Kα1 x-ray emitted is computed as follows:

$$I_{K\alpha 1}^F(A) = I_{K\alpha 1}(A)(1 + \delta_{Characteristic} + \delta_{Continuum}) \tag{4.27}$$

where $P_{K\alpha 1}$ is the fraction of $K\alpha 1$ emission. Emitted values (including absorption effect) are used, since the A and B and fluorescence are supposed to have been generated at the same location.

The fluorescence due to the continuum, which may have a consequent effect in the case of high energy characteristic x-rays and if $f(\chi) \leq 0$ (equation 2.17). The bremsstrahlung fluoerescence can be approximated by an equation similar to the characteristic fluorescence for the element A:

$$\frac{I_f}{I_A} = \alpha \cdot \frac{1 - r_A}{r_A} A_A \cdot \bar{Z} \cdot G \tag{4.28}$$

where

$$\alpha = 4.34 \cdot 10^{-6} \tag{4.29}$$

for Kα line,

$$\alpha = 3.31 \cdot 10^{-6} \tag{4.30}$$

for $L\alpha$ line. and

$$G = E_c(\Lambda) \cdot \frac{(\mu/\rho)_e^A}{(\mu/\rho)_e} \frac{ln(1 + wU_0)}{wU_0} \tag{4.31}$$

$\bar{Z}$ is the average atomic number, $(\mu/\rho)_e$ is the mass absorption coefficient of element A on the high energy side of the absorption edge, $(\mu/\rho)_e^A$ is in pure element A, $(\mu/\rho)_e$ in the specimen.

w is an integration factor:

$$w = \frac{(\mu/\rho)_A}{(\mu/\rho)_K} \csc\psi \tag{4.32}$$

If there is peaks between the line A and the beam energy, G must be calculated for each energy interval between $E_c(A)$ and E_0:

4.5 Calculation of the $\varphi(\rho z)$ curves

4.5.1 Electron-matter interaction

In order to determine the composition using the proposed method, the calculation of the ratio must be computed in order to compare it with the experimental results. The next chapter will present a brief overview of the electron-matter interaction models. The electron scattering in a material results in changes in the electron direction and energy due to the interaction of the incident electron with the atoms one by one. The most important concept of electron-particle interaction is the cross-section Q. It can be seen as a quantity proportional to the probability of a particle to enter the interaction field of another particle, and then to scatter it.

The most general definition for the cross-section for any event involving particle interaction [37] is:

$$Q = \frac{N}{n_i n_t} \tag{4.33}$$

in cm^2, where N is the number of events of a certain type per unit volume, n_i is the number of incident particles per unit area and n_t is the number of target sites per unit area. The cross-section may be understood as the effective size of the scattering process of an effective atom. The probability of interaction on a infinitesimal path Δx of density ρ is linked to the cross-section by :

$$P = \frac{Q N_A \rho \Delta x}{A} \tag{4.34}$$

For instance, the elastic cross-section is related to the electron mean free path, the average length an electron travels between events of the same type, by:

$$\lambda = \frac{A}{N_A \rho Q} \tag{4.35}$$

When an electron impinges on a material, it suffers interactions with the atoms which can be separated into two types: inelastic and elastic scattering [37]. Elastic scattering represents the interaction between the incident electron and the atomic nucleus. The small mass of the incident electron with respect to the mass of the atom makes the energy transfer extremely low. However, a fraction of the incident electrons suffers scattering through non negligible angles. Hence elastic scattering produces significant electron trajectory deviation but low energy loss. In practice, the energy loss is considered nil. Inelastic scattering is responsible for the transfer of energy from the incident electron to the specimen and then causes the generation of secondary electrons, characteristic x-rays, Auger electrons and bremsstrahlung x-rays essentially as well as intrabond transitions, plasmons and thermally diffuse phonons. Inelastic scattering causes energy loss and low angular deviation. The modeled inelastic interaction is in practice only described by an energy loss. In that case, the direction of the electron trajectory is essentially determined by elastic scattering.

Usually the cross-section depends on the incident electron energy, the scattering angle of its deviation and the energy of the secondary product created by the inelastic interaction. The differential cross-section is expressed in terms of a derivative

function, for example the scattering solid angle:

$$dn = J\frac{dQ(\theta)}{d\Omega}d(\Omega) \tag{4.36}$$

where n is the number of electrons from the flux J deflected in the angle θ, represented by the solid angle Ω.

$$d\Omega = \sin(\theta)d\theta d\varphi \tag{4.37}$$

where φ is the azimuthal angle. The integration with respect to θ of the partial elastic cross-section σ (in cm^2) gives the total cross-section σ_T:

$$\sigma_T = 2\pi \int \frac{d\sigma}{d\Omega} sin(\theta)d(\theta) \tag{4.38}$$

4.5.2 Electron trajectory and elastic cross-section

The oldest model of elastic cross-section relies on Rutherford's theory presented in 1911, after the famous experiment of scattering alpha particles through thin Au foil. The model suggested the mass of the atom is concentrated in a very small nucleus and is based on the particulate theory of electrons. Rutherford derived his equation from the equation of movement of a negatively charged electron in the positive electric field of the nucleus, according the rules of classical mechanics. Up to 50 keV, the relativistic effect can be ignored, causing an error less than 1 % in the cross-section. This expression was later improved, starting from quantum physics and including the effect of screening (effect of the atomic electrons in reducing the effective potential of the nucleus). The partial cross-section is related to the angular

distribution of scattering, the solid angle Ω and is given by Newbury et al. [71]:

$$\frac{d\sigma^{el}}{d\Omega} = |f(\theta)|^2 = \frac{e^4 Z^2}{4(4\pi\varepsilon_0)^2 E^2} \frac{1}{\left(\sin^2(\theta/2) + \alpha\right)^2} \tag{4.39}$$

where $f(\theta)$ is the resulting scattering amplitude depending on the scattering angle θ, e the electron charge, Z the atomic number of the scatter element, E the energy of the incident electron, ε_0 the dielectric constant and α the screening parameter, related to the effect of the atomic electrons on the net potential of the atom:

$$\alpha = \frac{\theta_0^2}{4} \tag{4.40}$$

where θ_0 is linked to the screening parameter of Wentzel $a = a_H Z^{-1/3}$ by the relation $\theta_0 = 2\lambda/4\pi a$, $\lambda = h/mv$ and a_H is the Bohr radius. The total screened elastic cross-section is given by integration:

$$\sigma^T = 2\pi \int_0^\pi \frac{d\sigma^{el}}{d\Omega} \sin\theta d\theta = 5.21 \times 10^{21} \frac{Z^2}{E^2} \frac{4\pi}{\alpha(1+\alpha)} \tag{4.41}$$

Rutherford's formula is only valid for a very low scattering angle, at high energy and for low atomic number elements [27], when the electron wave can be approximated as a plane wave after elastic scattering (known as the first Born approximation), usually between 10 to 50 keV for targets of low to intermediate atomic number. If the atom is too large, the wave shift becomes no longer negligible, because the interaction deforms the wave that becomes spherical [30]. Therefore, the Rutherford elastic cross-section is no longer valid if:

$$E \ll \frac{1}{2}\left(\frac{Z}{137}\right)^2 mc^2 \tag{4.42}$$

where E is the non-relativistic kinetic energy of the particle, m the particle mass and c the speed of light.

In fact this equation does not take into account the electron spin and the spin-orbit coupling in diffusion. A more accurate cross-section was later calculated from the iterative resolution of the Pauli-Dirac equation, based on quantum mechanics, in order to take into account spin and relativistic effect. The partial cross-section is established for a unpolarized electron beam:

$$\begin{aligned} \frac{d\sigma}{d\Omega_{\theta,\chi}} &= |f(\theta,\chi)|^2 + |g(\theta,\chi)|^2 \\ \theta_1 &= e^{ikz} + f(\theta)\frac{e^{ikr}}{r} \\ \theta_2 &= g(\theta)\frac{e^{ikr}}{r} \end{aligned} \tag{4.43}$$

where $f(\theta,\chi)$ is the scattering amplitude and $g(\theta,\chi)$ is the spin-flip amplitude related to the effect on the second spin director, both functions dependent on the azimuth angle χ [86]. The solution of these equations produces the so-called Mott cross-sections, which cannot be expressed by a simple analytical formula like the Rutherford elastic cross-section. The comparison between the Rutherford and Mott cross-sections shows important discrepancy for high atomic number elements and low acceleration voltage. But independently of the model, the elastic cross-section increase with the atomc number and backscattering increases with the beam energy because $d\sigma/d\Omega \propto Z^2/E^2$.

These equations were numerically solved to get tabulated elastic cross-sections [70, 21]. Because equations are simpler to manipulate, analytical fitting was developed by Gauvin et al. [34] and Browning et al. [10]. The total Mott-Browning cross-sections

were found to fit with the function:

$$\sigma^T = 4.7 \times 10^{-18} \times \frac{Z^{1.33} + 0.02Z^2}{E + 0.0155Z^{1.33}E^{0.5}} \frac{1}{1 - 0.02Z^{0.5}e^{-u^2}} \tag{4.44}$$

in cm^2 and with

$$u = \log_{10}\left(8EZ^{-1.33}\right) \tag{4.45}$$

The Mott-Browning model is based on the idea that a portion of the scattered electrons is Rutherford-like and another portion is scattered isotropically. The ratio of the Rutherford and isotropic cross-section is evaluated and it is then possible to determine a new scattering angle.

$$\frac{\sigma_{rutherford}}{\sigma_{isotropic}} = \frac{300 \cdot E^{1-\frac{Z}{2000}}}{Z} + \frac{Z^3}{3 \times 10^5 E} \tag{4.46}$$

Mott-Browning elastic cross-sections show quite a good agreement with calculated and measured values, such as Mott's tables; they are easy to use [25]. Nevertheless, this model underestimates backscattered yields for high-Z elements at low energy, and needs adjustment to produce a better correlation with experimental results.

4.5.3 Inelastic electron interaction

This scattering mode is a consequence of the interaction with inner or outer shell electrons [40]. Inelastic interactions are represented by energy loss ΔE and very small trajectory deviation because of the low weight of the particle. When the electron enters the Coulombic field around the atom, it transfers energy to the electrons of the atom. It is common to assume that electrons lose energy in straight lines between elastic collisions. Usually inelastic scattering events are modeled as a continuous rate of energy loss since the inelastic cross-sections are not accurately

known. The mean energy loss on the trajectory segment s is given by the equation:

$$dE_m = \frac{\rho N_A Z}{A} ds \int_{\epsilon_i}^{\epsilon_f} \epsilon \frac{d\sigma}{d\epsilon} d\epsilon \tag{4.47}$$

Since 1930, all inelastic effects have been included in the classical Bethe equation [8]:

$$\frac{dE}{dS} = -\frac{2\pi e^4 \rho N_A}{(4\pi\epsilon_0)^2 E} \sum_{i=1}^{n} \frac{c_i Z_i}{A_i} \cdot \ln\left(\frac{1.166E}{J_i}\right) \tag{4.48}$$

where ρ is the specimen density, c_i and A_i are respectively the concentration and the atomic weight of the element i and J_i is the mean ionization potential of element i. This last expression is only valid when $E > 6J$. Below 6Z, J becomes dependent on the electron energy and the atomic number of the element. In that case, J can be roughly expressed as 0.115Z (in keV) but a more exact empirical formula is given by Berger et al. [6]:

$$J(keV) = (9.76Z + 58.5Z^{-0.19}) \times 10^{-3} \tag{4.49}$$

Joy and Luo [53] developed a fitting of the Bethe stopping power function, by using the modified mean ionization potential J^* in order to improve the modelling of the potential J shown in equation 4.50:

$$J^* = \frac{J}{1 + k\frac{J}{E}} \tag{4.50}$$

They introduced a variation of J with E in order to take into account the fact that with an energy below the K shell critical energy, the electron does not have enough energy to ionize it and J decreases. Gauvin et al. [32] also established a fitting from

the published values of Joy and Luo for the k term:

$$k = 0.7344 \cdot Z^{0.0367} \tag{4.51}$$

The continuous energy loss rate includes the generation of secondary electrons as well as all inelastic events. It has been proved to be quite a good approach for electron-matter interaction, particularly with the comparison of simulated backscattered yield of pure homogeneous materials with experimental results [49]. On the other hand, energy fluctuation is neglected, because, in reality, the electron discretely loses energy as demonstrated by Fernández-Varea et al. [30]. The calculated energy loss on a path of length L, given by $\Delta E = (dE/ds) \cdot L$ is an average. When the distance between elastic scattering events L becomes too small, statistical effects are no longer negligible and may have an important effect on total electron path and local electron energy loss, but this is not the case for most materials, except in the case of the microelectronics industry, where the features may be a few nanometers in size.

Chapter 5
Calculation and processing of spectrum

5.1 Monte Carlo simulation

Much work has been done on the calculation of the emitted x-ray intensity. The analytical methods like the $\varphi(\rho z)$ models introduced in section 2.4 have the advantage of speed and ease. However, they are mostly limited to homogeneous materials, or limited geometry. The most versatile method is the single-scattering Monte Carlo method, which describes the electron-matter interaction as a statistical process. The interaction of the electron beam with the matter is reduced to the simulation of multiple trajectories of electrons, one by one, and reproduced thousands of time in order to ensure statistical stability. Then the calculations are repeated thousands of times, with the help of random numbers to describe the real phenomenon. Finally, the values are estimated with the average over all the simulated trajectories. Usually, a few thousand trajectories are sufficient to reach good statistical stability. In the present work, new models for the x-ray generation parameters are used as described in section 4, full spectrum with bremsstrahlung simulation. Moreover, new models have been implemented, more characteristic lines and the Coster-Kronig phenomenon have been added.

In a single-scattering Monte Carlo simulation, many individual electron trajectories are independently computed until each electron either exits the sample or is

completely absorbed in the material. Kyser et al. [58], Newbury et al. [71], Gauvin [33, 48, 25, 49] and Shimizu et al. [102, 101] have developed classical Monte Carlo programs by single-scattering trajectory simulation. Salvat et al. [94], [92] developed a more sophisticated program, where each scattering event is simulated one by one and by using a discrete energy loss model. The energy loss model is essential in the definition of a Monte Carlo model, because the discrete model considers elements separately while the continuous model makes an average. This method, if expected to give more accurate results, is extremely time consuming. Therefore, the continuous energy loss model is used in the present single-scattering program. It can be run on a personal computer and gives results in a reasonable amount of time.

The interaction of an incident electron with the material is computed when the total elastic or inelastic cross-section shows that it experiences an interaction with a lattice atom, by computing the mean free path of the electron. The occurrence of the event is calculated with a random number, allowing quite good representation of the real distribution of physical values. Statistical averages are calculated to compute output signals (secondary and backscattered electron yields, x-ray spectrum) as well as quantities that cannot be directly measured (distribution of energy loss in the sample, various spatial distributions).

An essential equation of Monte Carlo simulation is the distribution equation 5.1 [86] where $P(X)$ is given as a probability of a specific event.

$$P(X) = \frac{\int_{x_1}^{X} p(x)\,dx}{\int_{x_1}^{x_2} p(x)\,dx} \tag{5.1}$$

where $p(x)\,dx$ is the probability that this event occurs between x and $x + dx$ and is defined on $[x_1; x_2]$. In the case of Monte Carlo simulation, $P(X)$ is generated as a random number R in the range $[0; 1]$ and X is calculated as a solution of the equation 5.1, which needs then to be inverted to extract the parameter X related to the probability $P(X)$. In some cases, an analytical function permits computation of the value of X, but in most cases a numerical solution must be used. The electron scattering is modeled and shown in figure 5–1.

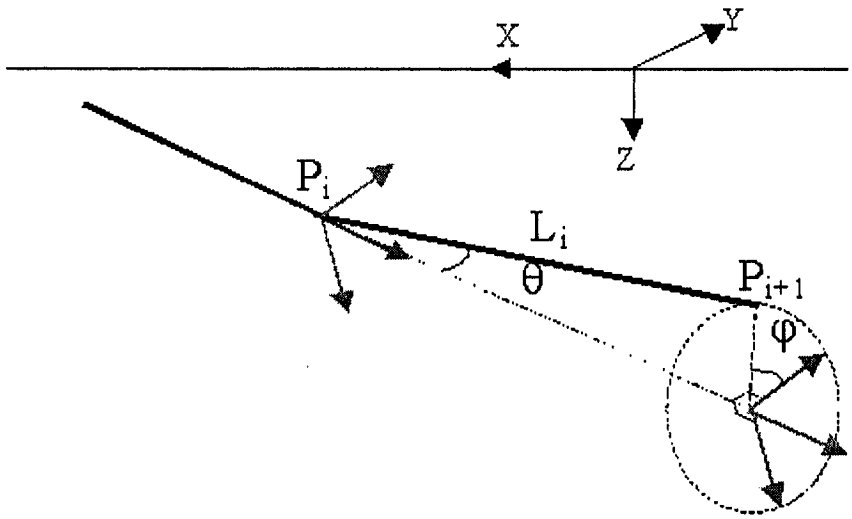

Figure 5–1: Theory of elastic collision of an electron in Monte Carlo simulation

L_i is the distance between the two collisions or elastic interactions $P(i)$ and $P(i+1)$, θ is the polar angle and φ is the azimuthal angle of the new electron direction after the scattering. Each of these parameters is computed independently, with random numbers and distribution equations. The developed Monte Carlo program is based on classical and proven physical principles [71, 33, 36].

Elastic scattering represents the interaction between the incident electron and the atomic nucleus. Elastic scattering is modeled by electron trajectory deviation (θ, φ) and no energy loss. Inelastic scattering causes energy loss ΔE and small trajectory deviation. The first step consists of calculating the distance L to the next elastic scattering event:

$$L = -\lambda \ln R_1 \tag{5.2}$$

where R_1 is a random number in $[0; 1]$, the probability of the electron to travel the path L to the next elastic collision and λ is the electron elastic mean free path:

$$\lambda = \frac{1}{\sum_{i=1}^{n} \frac{C_i \rho N_A}{A_i} \sigma_i^{el}} \tag{5.3}$$

C_i and A_i being respectively the concentration and the atomic weight of the element i, ρ the density of the material and N_A the Avogrado's number. The next step consists of computing the deviation angle of the electron trajectory, with respect to its previous direction. An azimuthal angle φ, of probability R_2, uniformly distributed from 0 to 2π, is needed:

$$\varphi = 2\pi R_2 \tag{5.4}$$

as well as a polar angle θ_e distributed between 0 and π, according a distribution determined by the probability R_3 related to the partial elastic cross-section:

$$R_3 = \frac{\int_0^{\theta_e} \frac{d\sigma}{d\Omega} \sin\theta d\theta}{\int_0^{\pi} \frac{d\sigma}{d\Omega} \sin\theta d\theta} \tag{5.5}$$

Equation 5.5 can be inverted with the Rutherford cross-section model for scattering of a charged particle by a nucleus of charge Ze [6]:

$$\frac{d\sigma_R}{d\Omega} = \frac{Z^2 e^4}{p^2 v^2 \left(1 - \cos\theta\right)^2} \tag{5.6}$$

where p is the momentum and v the electron velocity. But an analytical inversion is impossible using Mott cross-sections; then, numerical solutions give tabulated Mott cross-sections.

The element i concerned in the elastic interaction is chosen with the help of another random number R_4. The element i is chosen when $N_{i-1} < R_4 < N_i$, where:

$$N_i = \frac{\sum_{j=1}^{i} \frac{c_i \rho N_A}{A_i} \sigma_i^{el}}{\sum_{j=1}^{n} \frac{c_i \rho N_A}{A_i} \sigma_i^{el}} \tag{5.7}$$

with $N_0 = 0$.

The energy loss of the electron is then calculated by computing the inelastic events occurring between two elastic interactions. In a very thin sample, since the electron travels only a very short distance, the inelastic interactions are negligible, as happens in the transmission electron microscope. But, samples for scanning electron microscopes are mostly bulk. Energy loss ΔE is no longer low. The energy E' of the incident electron at the next elastic event can be calculated:

$$E' = E + \Delta E \tag{5.8}$$

where ΔE is negative. The computation of ΔE can be perfomed in two different ways, the continuous energy loss rate and the discrete model. In the first case,

$$\Delta E = \frac{dE}{dS} \cdot L \tag{5.9}$$

assuming that dE/dS is the average energy loss given by the Bethe continuous stopping power and that the electron travels in straight lines between elastic interactions. In the case of the discrete model, the energy loss ΔE is directly computed from the integration of a complex partial cross-section.

The Monte Carlo program calculates generated $\varphi(\rho z)$ values for each slice of thickness $\Delta\rho z$ at depth z in the interaction volume of the specimen. For each element and x-ray characteristic line, the function is normalized by a slice containing the pure element. The absorption is also calculated for each thickness, then the emitted $\varphi(\rho z)$ curve is computed and integrated. In order to produce the generated and emitted intensities, this last value is multiplied by all the physical parameters as shown in equation 2.6. The obtained intensity is convoluted with a Gaussian distribution in order to achieve the shape of a real x-ray spectrum.

Finally, the complete simulated spectrum can be compared with an experimentally-obtained spectrum as in figures 5–3 and 5–2.

Figure

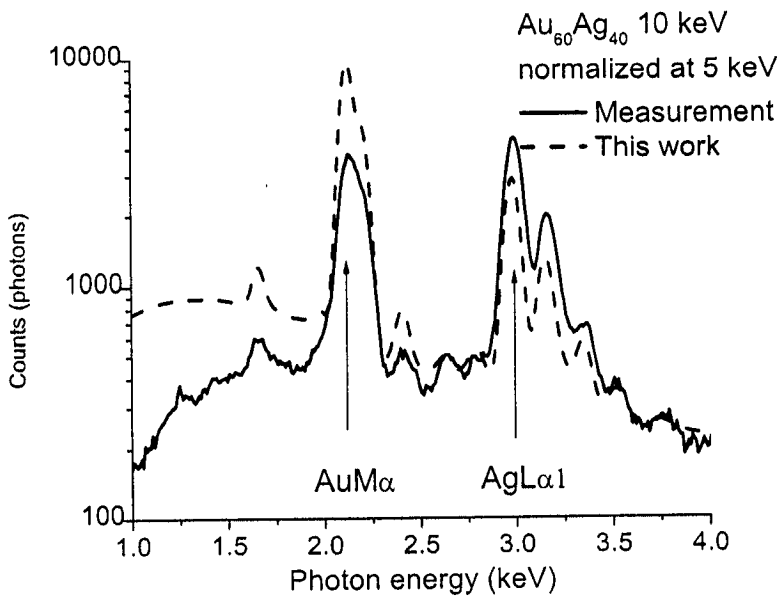

Figure 5–2: Comparison of complete simulated and experimental spectra of the $Au_{40}Cu_{60}$ alloy at 15 keV

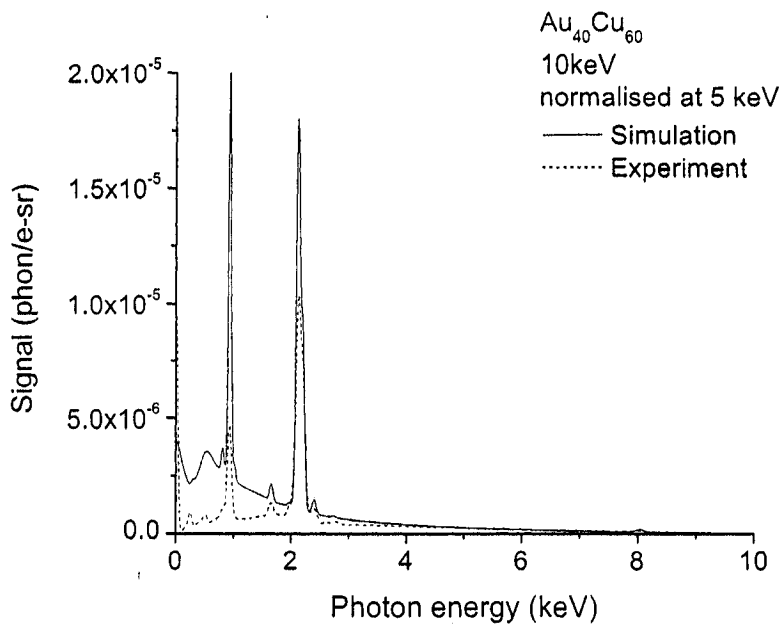

Figure 5–3: Comparison of complete simulated and experimental spectra of the $Au_{40}Cu_{60}$ alloy at 15 keV

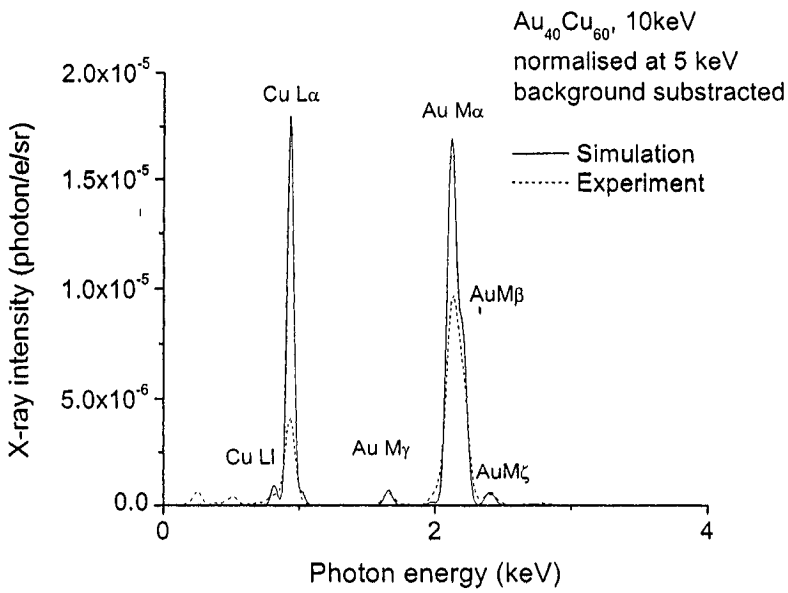

Figure 5–4: Comparison of complete simulated and experimental spectra with background subtraction of the $Au_{40}Cu_{60}$ alloy at 15 keV

5.2 Pouchou and Pichoir model

Pouchou and Pichoir (PAP) described the $\varphi(\rho z)$ curve as the sum of two parabolic functions [77]. They first identified the area F below the $\varphi(\rho z)$ curve as the number of ionizations:

$$F = \left(\frac{R}{S}\right) \frac{1}{\sigma(E_0)}, \tag{5.10}$$

where R is the backscattering coefficient, describing the ionization loss due to backscattered electrons, S is the stopping power and σ the ionization cross-section. R is expressed as a function of the mean backscatter coefficient and the mean reduced energy of the backscattered electron $\overline{W}$:

$$R = 1 - \cdot \overline{W}\,[1 - G(U_0] \tag{5.11}$$

where the needed parameters are explained in the paper [77]. Then they developed the parameterization description of the function:

$$\varphi_1(\rho z) = A_1\,(\rho z - R_m)^2 + B_1 \quad \text{for} \quad 0 \leq \rho z \leq R_c \tag{5.12}$$

$$\varphi_2(\rho z) = A_2\,(\rho z - R_x)^2 \quad \text{for} \quad R_c \leq \rho z \leq R_x \tag{5.13}$$

where A_1, B_1 and A_2 are parameters, and R_m is the mass depth where the curve reaches a maximum, R_c where the two curves are equal and R_x where the tangent is horizontal. The description of the distribution at $\rho z = 0$, $\rho z = R_c$ and $\rho z = R_x$ allows the solution of the equation 5.13 and to get the root R_c

$$R_c = \frac{2}{3 \cdot \varphi_0}\left(F - \frac{\varphi_0 R_x}{3} - \frac{d^{1/2}}{(R_x - R_m)}\right)$$

$$d = (R_x - R_m)\left[F - \varphi_0\frac{R_x}{3}\right] \cdot \left[(R_x - R_m) \cdot F - \varphi_0 \cdot R_x\left(R_m + \frac{R_x}{3}\right)\right] \quad (5.14)$$

Using this root and the form parameters R_x, R_m and R_c of the distribution, the parameters of the parabolic functions are obtained:

$$\begin{aligned} A_1 &= \frac{\varphi_0}{R_m\left(R_c - R_x(\frac{R_c}{R_m} - 1)\right)} \\ B_1 &= \varphi_0 - A_1 \cdot R_m^2 \\ A_2 &= A_1\frac{R_c - R_m}{R_c - R_x} \end{aligned} \quad (5.15)$$

where φ_0, R_x and R_m are given in paper [77].

In order to validate the Monte Carlo simulation for the generation of x-rays, some $\varphi(\rho z)$ curves were compared with the PAP model. The chosen material is one of the standards used for the validation of the method, a $Au_{40}Cu_{60}$ alloy, at 20 keV. Figures 5–5 and 5–6 present the $\varphi(\rho z)$ curves for the main subshells of Cu and Au respectively. Despite the fact that the modeling (particularly for the ionization cross-section) is completely different, the curves show a good agreement, except for the CuK curve. The maxima of the curves are not identical, due to the different modeling of the ionization cross-section.

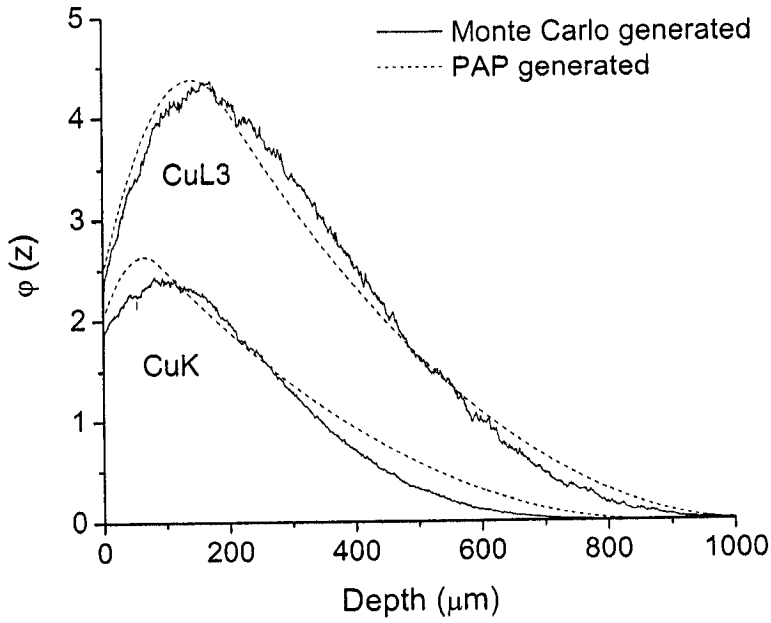

Figure 5–5: Comparison of Cu K and Cu LIII PAP and Monte Carlo generated $\varphi(\rho z)$, for the $Au_{40}Cu_{60}$ standard at 20 keV

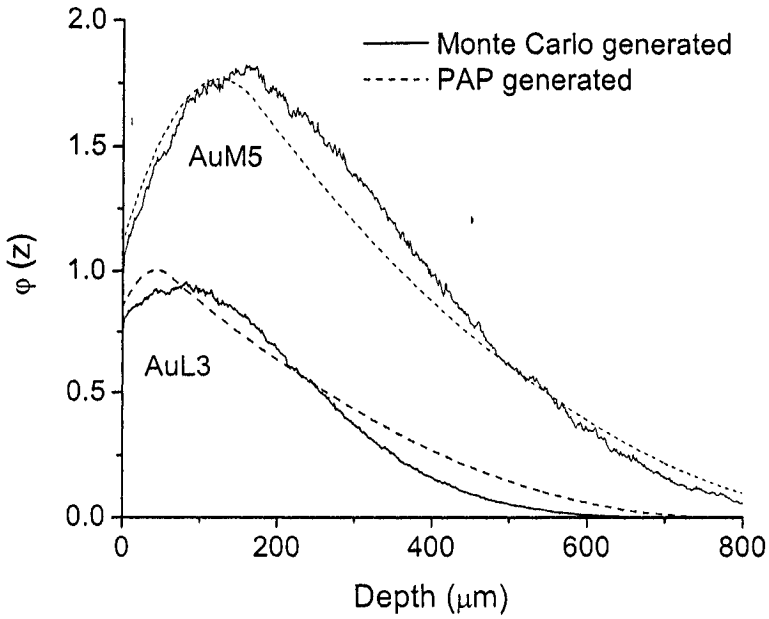

Figure 5–6: Comparison of AuL3 and AuM5 PAP and Monte Carlo generated $\varphi(\rho z)$, for the $Au_{40}Cu_{60}$ standard at 20 keV

5.3 Bremsstrahlung generation

The incident electrons may also be decelerated in the Coulombic field of a nucleus. This can result in the emission of a background x-ray. This is the same process as for elastic scattering, but the energy transfer is not sufficient to deviate the electron trajectory because of the low probability of the event. Then an x-ray quantum of energy E_x is generated and the incident electron energy is decreased by E_x. The rate of deceleration of the electron is statistically spread between 0 and the electron energy. The atomic number of the atoms affects the bremsstrahlung intensity, especially at the position of the ionization edge. Bremsstrahlung ionization generates a photon of which the energy is proportional to the energy loss, therefore to the mean atomic number of the specimen. This phenomenon generates background x-rays, distributed in the energy range from 0 to the incident beam energy. The generated background intensity is approximately proportional to $1/E$ in the largest part of the spectrum. Its typical shape is energy dependent, because x-ray absorption varies with x-ray energy, and the intensity of generated x-rays depends on the energy.

The most used cross-section has been fitted by Kirkpatrick et al. [56] from calculations made with the non-relativistic Sommerfeld theory, which was corrected with an approximate correction for retardation and an approximate screening correction. Despite a problem noted for high atomic number and low electron energy, Chapman et al. [16] concluded that the comparison of various models precludes the recommendation of the use of one model or another, and moreover, due to the lack of a relevant and easy-to-use model, the Kirkpartick-Wiedman model for total bremsstrahlung cross-section σ (in millibarn by steradian) is implemented according

to the equations:

$$\sigma = 0.887\left\{I_x'\frac{\sin^2\theta_0}{(1-\beta_0\cos\theta_0)^4} + I_y'\left[1+\frac{\cos^2\theta_0}{(1-\beta_0\cos\theta_0)^4}\right]\right\} \tag{5.16}$$

where

$$I_x' = 0.252 + c_1\left(\frac{k}{T_0} - 0.135\right) - c_2\left(\frac{k}{T_0} - 0.135\right)^2 \tag{5.17}$$

$$c_1 = 1.47C_2 - 0.507C_1 - 0.833 \tag{5.18}$$

$$c_2 = 1.70C_2 - 1.09C_1 - 0.627 \tag{5.19}$$

$$C_1 = e^{-\frac{0.223V}{Z^2}} - e^{-57\frac{V}{Z^2}} \tag{5.20}$$

$$C_2 = e^{-\frac{0.0828V}{Z^2}} - e^{-84.9\frac{V}{Z^2}} \tag{5.21}$$

$$V = 1703T_0 \tag{5.22}$$

$$I_y' = -d_2 + \frac{d_3}{\frac{k}{T_0} + d_1} \tag{5.23}$$

$$d_1 = \frac{-0.214D_1 + 1.21D_2 - D_3}{1.43D_1 - 2.43D_2 + D_3} \tag{5.24}$$

$$d_2 = (1+2d_1)D_2 - 2(1+d_1)D_3 \tag{5.25}$$

$$d_3 = (1+d_1)(D_3+d_2) \tag{5.26}$$

$$D_1 = 0.220[1 - 0.390e^{-6.9\frac{V}{Z^2}}] \tag{5.27}$$

$$D_2 = 0.067 + \frac{0.023}{\frac{V}{Z^2} + 0.75} \tag{5.28}$$

$$D_3 = -0.00259 + \frac{0.00776}{\frac{V}{Z^2} + 0.116} \tag{5.29}$$

where θ_0 is the angle between the initial momentum of the incident electron and the momemtum of the emitted photon, β_0 is the ratio between the initial velocity of

the incident electron and the velocity of light, T_0 is the initial kinetic energy of the electron and k is the Boltzman constant.

5.4 Background subtraction

Many different methods exist to extract the peak intensity with different typed of filter, introducing extraction and deconvolution errors [5, 106]. Calculated spectra can also be used, if the models of bremsstrahlung generation are accurate enough. In order to separate the background and the characteristic peaks, the user can draw the background by himself, by a linear extrapolation of the background under the peak as shown in figure 5–7 where the function baseline of the software Origin^{TM}was used.

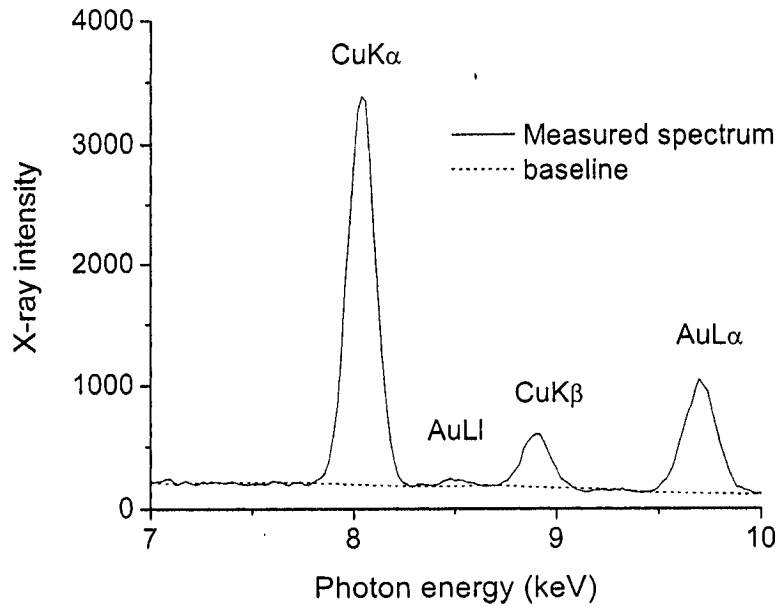

Figure 5–7: Example of baseline for background subtraction, $Au_{60}Cu_{40}$ at 20 keV, FEG-SEM Hitachi 4700, Oxford EDS detector

It is time-consuming to manually perform this on many spectra. Morevoer, this analytical extraction produces generally good accuracy above 3 keV, where the background shape is linear. Below this threshold, the results should be treated with caution. Because it does not account for the absorption discontinuities at low voltage, this empirical method does not provide excellent accuracy. The best choice is the subtraction of a calculated background, which should be more representative of the true background shape. The principal condition is the knowledge of the background generation parameters, which is not the case as it is shown in figures 5–3 and 5–4 for low photon energy. The simplest approach is the mathematical filtering, which considers the spectrum as an electronic signal, rather than a physical phenomenon. This method consists of using a band filter which averages a certain number of weighted channels. However, it does not account for the discontinuities in the background at low photon energy, at the absorption edges. Anomalies are partially compensated in the case of the Castaing ratio method [5]. In this work, the background is subtracted by the "top-hat" filter method, as proposed by Schamber [95] and applied by Statham [105]. This offers a good compromise between statistical accuracy, sensitivity to background shape and possible errors in peak models. There is no need to determine the continuum shape. The filter proposed by Statham is represented as three weighted squares, the central lobe (upper width) being weighted with a positive coefficient and the lower lobes containing negative coefficients as shown in figure 5–8.

As an example, a measured spectrum of the $Au_{20}Cu_{80}$ standard, microanalyzed at 20 keV (shown in figure 5–9) is filtered. When this filter is applied to a spectrum consisting of the sum of a Gaussian peak and a linear background, the straight line

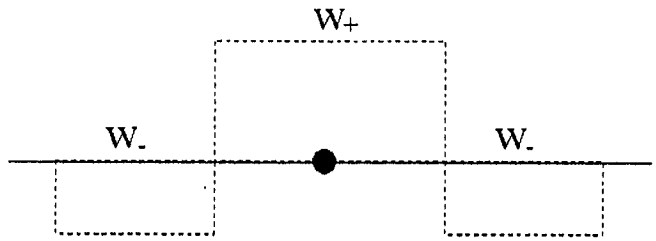

Figure 5–8: Top-hat filter for bremsstrahlung subtraction [105]

is suppressed and only the peak remains, with negative values on both sides. When the slope is low, the filter produces a null value. As soon as there is a change in the slope (sides of peaks), the resulting intensity is negative. The main part of the peak is positive as shown in figure 5–10. The program find the parameters of a filtered Gaussian function by fitting the filtered spectrum by the same Top-Hat filter. From these parameters, it computes a Gaussian function and then calculates the x-ray intensity by its integration as developped by Demers [23]. Figures 5–11 and 5–12 show the results for the peaks centered around the L and Mα peaks of Cu and Au respectively. In figure 5–11, the non-linear shape of the background is due to the overlapping of main Cu lines of the L family (Lα1, Lα2, Lβ1, Lβ4 and Lη+Ll). The effect is similar in figure 5–12 due to the overlapping of lines AuMα and AuMβ of Au.

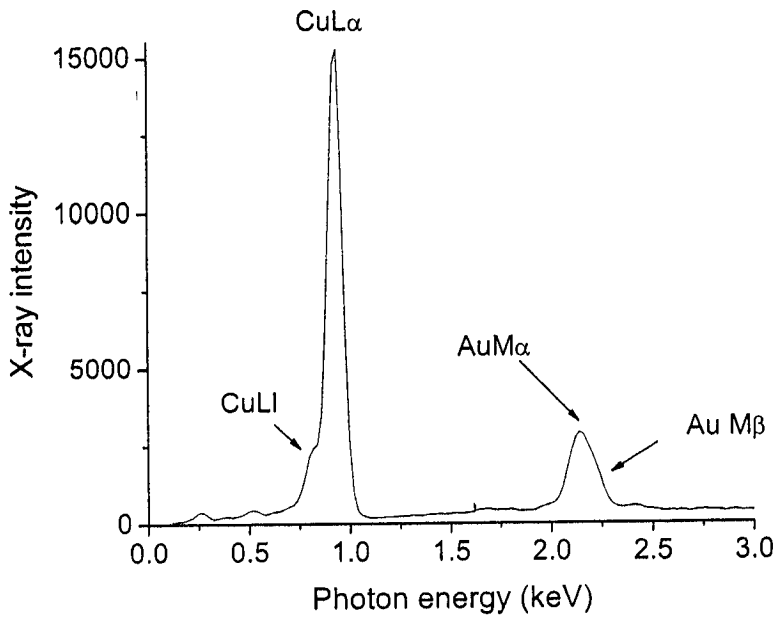

Figure 5–9: Measured spectrum of the $Au_{20}Cu_{80}$ standard alloy at 20 keV, 100 s live time

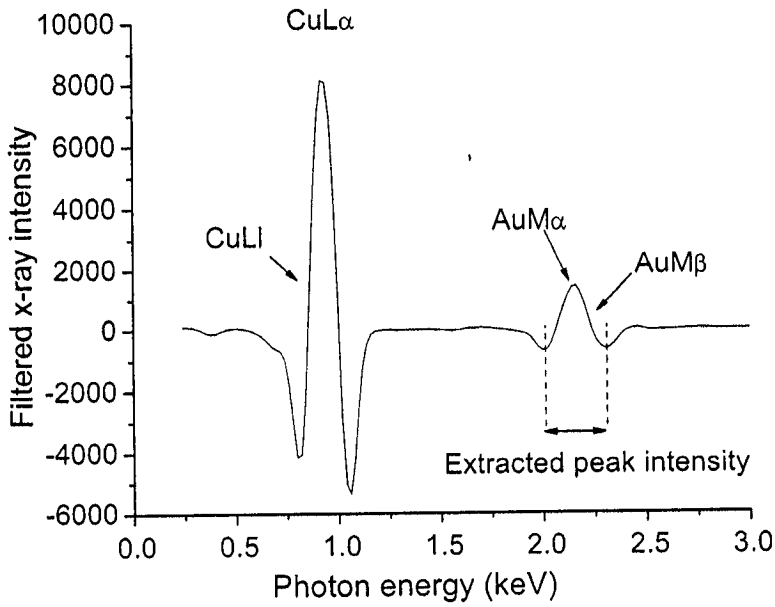

Figure 5–10: Spectrum of figure 5–9 filtered by the top-hat filter [105], zoom on the CuLα and AuMα peaks

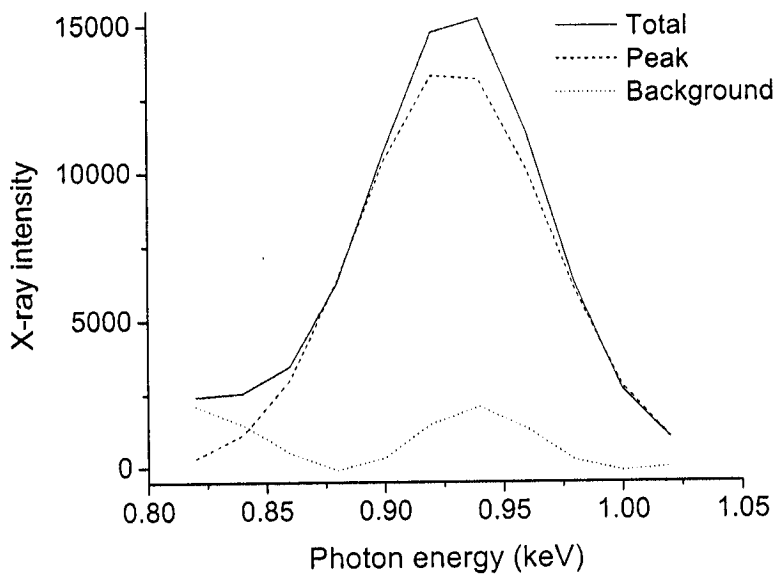

Figure 5–11: Extracted peak centered at 0.93 keV around the CuLα1 characteristic peak

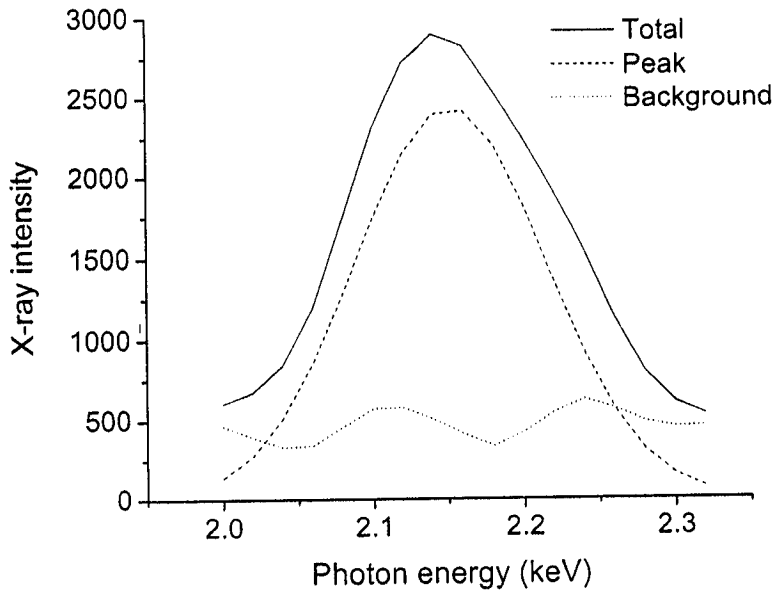

Figure 5–12: Extracted peak centered at 2.14keV around the AuMα and AuMβ characteristic peaks

Chapter 6
Validation of the quantification method

6.1 Experimental procedure

This quantification method was then applied to some standards of known composition, in order to validate the methodology. For that purpose, binary standards for microanalysis from the NIST were chosen. The first step consisted of determining the calibration factors. Afterwards, the concentration was calculated with the simulated and microanalyzed x-ray intensities. The behavior of the calibration factor with different parameters -such as beam energy and element concentration - was studied in order to evaluate the stability of the method.

The validation of the method was carried out on gold-copper standard alloys (SRM 482 [74], from NIST standards for the microprobe, mounted by Geller MicroÅnalytical Laboratory, Inc. in a silver matrix) and gold-silver standards (SRM 481 [73], same manufacturer and mounting as SRM482) of 20, 40, 60 and 80 % of gold. Figures 6–1 and 6–1 present the official certificates of the standards [104, 103]. Heinrich et al. [43] described the preparation and evaluation of these standards for microanalysis.

The nominal compositions of the standards are not exactly as the measured, as shown by the certificates of the alloys in figures 6–1 and 6–2 (the last pages are shown in the appendix B). For the calculations, the real values indicated on the certificate have been used. Furthermore Windsor et al. [111] observed copper oxide

U. S. Department of Commerce
Maurice H. Stans
Secretary

National Bureau of Standards
A. V. Astin, Director

Certificate of Analysis

STANDARD REFERENCE MATERIAL 482
Gold-Copper Wires for Microprobe Analysis

These standard reference materials are designed for use in quantitative elemental microprobe analysis. Although the selection of this particular system was circumscribed by the requirements of standard reference materials for electron probe microanalysis, the materials will be equally useful for other micro techniques. Accurate chemical characterization and the achievement of homogeneity on a microscopic scale were given special emphasis.

SRM 482 wire	Color code	Nominal composition	Cominco American[a]	U.S. Bureau of the Mint[b]		NBS[c]		Average value[d]	
			Au	Au	Cu	Au	Cu	Au	Cu
			Percent by weight						
A	Gold	Au100	—	—	—	—	—	100.0_0	—
B	Gray	Au80 – Cu20	80.10	80.13	19.81	80.21	19.85	80.1_5	19.8_3
C	Blue	Au60 – Cu40	60.30	60.37	39.66	60.41	39.62	60.3_6	39.6_4
D	Yellow	Au40 – Cu60	40.12	40.06	59.88	40.11	59.97	40.1_0	59.9_2
E	Red	Au20 – Cu80	20.04	20.12	79.84	20.21	79.86	20.1_2	79.8_8
F	Copper	Cu100	—	—	—	—	—	—	100.0_0

[a] The fire assay method was employed for the determination of Au by Cominco American.

[b] At the U. S. Bureau of the Mint, Au was determined by fire assay and Cu was determined by electrodeposition.

[c] At NBS, Au was determined by precipitation from solution; Cu was determined by electrodeposition.

[d] The results of individual laboratories agree within a range of ± 0.1% absolute from the average values. The agreement between results by the different methods and analysts, and the summation of results close to 100% for each binary alloy, indicate that the averages are free from significant bias.

The set of standard reference materials, SRM 482, consists of six wires each having a diameter of approximately 0.5 mm and a length of approximately 5 cm. For identification, the four alloy wires were covered with an easily removable colored coating.

The overall direction and coordination of technical measurements leading to certification were performed under the chairmanship of B. F. Scribner.

The technical and support aspects involved in the preparation, certification, and issuance of these standards were coordinated through the Office of Standard Reference Materials by R. E. Michaelis.

Washington, D. C. 20234
June 6, 1969

W. Wayne Meinke, Chief
Office of Standard Reference Materials

(over)

Figure 6–1: First page of certificate of analysis for the AuCu standards, SRM 482 [104]

U. S. Department of Commerce
Maurice H. Stans
Secretary

National Bureau of Standards
A. V. Astin, Director

Certificate of Analysis

Standard Reference Material 481
Gold-Silver Wires for Microprobe Analysis

These standard reference materials are designed for use in quantitative elemental microprobe analysis. Although the selection of this particular system was circumscribed by the requirements of standard reference materials for electron probe microanalysis, the materials will be equally useful for other micro techniques. Accurate chemical characterization and the achievement of homogeneity on a microscopic scale was given special emphasis.

SRM 481 wire	Color code	Nominal comp	Cominco American[a]	U.S. Bureau of the Mint[b]		NBS[c]		Average Value[d]	
			Au	Au	Ag	Au	Ag	Au	Ag
			Percent by weight						
A	Gold	Au100	---	---	---	---	---	100.0_0	---
B	Gray	Au80–Ag20	80.00	80.02	20.00	80.13	19.93	80.0_5	19.9_6
C	Yellow	Au60–Ag40	60.01	60.11	39.85	60.04	39.98	60.0_5	39.9_2
D	Blue	Au40–Ag60	39.99	40.03	59.90	40.06	59.96	40.0_3	59.9_3
E	Red	Au20–Ag80	22.42	22.42	77.59	22.46	77.56	22.4_3	77.5_8
F	Silver	Ag100	---	---	---	---	---	---	100.0_0

[a] The fire assay method was employed for the determination of Au by Cominco American.

[b] At the U.S. Bureau of the Mint, Au was determined by fire assay and Ag was determined by titration as AgCl.

[c] At NBS, Au was determined from the residue after treatment of the alloys with HNO_3. The Au residue was dissolved in aqua regia, filtered, the Au precipitated by sulfurous acid, and weighed. Ag was determined gravimetrically as AgCl in all four alloys, and also coulometrically in the 80 percent Ag alloy.

[d] The results of individual laboratories agree within a range of ± 0.1 percent absolute from the average values. The agreement between results by the different methods and analysts, and the summation of results close to 100 percent for each binary alloy, indicate that the averages are free from significant bias.

The set of standard reference materials, SRM 481, consists of six wires each having a diameter of approximately 0.5 mm and a length of approximately 5 cm. For identification, the four alloy wires were covered with an easily removable colored coating.

The overall direction and coordination of technical measurements leading to certification were performed under the chairmanship of B. F. Scribner.

The technical and support aspects involved in the preparation, certification, and issuance of these standards were coordinated through the Office of Standard Reference Materials by R. E. Michaelis.

Washington, D. C. 20234
February 14, 1969

(over)

W. Wayne Meinke, Chief
Office of Standard Reference Materials

Figure 6–2: First page of certificate of analysis for the AuAg standards, SRM 481 [103]

precipitates in all of the standards of SRM 482 (AuCu). The largest are in the $Au_{20}Cu_{80}$ wire with sizes up to 2 μm in diameter. The authors estimate that their occurrence depends on the specimen surface preparation. However, these precipitates have a low concentration (less than 1 % in area). In the case of microanalysis in a field emission scanning electron microscope, where the probe diameter is of few nm, the heterogeneity effect may affect the accuracy of the microanalysis since the beam may be hitting a precipitate.

The specimens are wire cross-sections inserted into a pure Ag matrix, in a steel specimen holder. They were microanalyzed at 5, 10, 15, 20, 25 and 30 keV, four times for each condition, with a live time of 100 seconds and a beam current ranging from 0.1 to 1 nA, in the Hitachi S-4700 cold FEG-SEM. Different beam energies were used, in order to evaluate its effect on the accuracy of the method. The beam current was measured with a Faraday cup inserted into the specimen chamber before and after each microanalysis. The calibration of the detector was regularly verified with a nickel specimen which would also detect icing problems. Where ice is present, the Ni Lα peak is lowered due to the absorption edge of the oxygen present in the ice and no longer has the same height as the Ni Kα peak.

The families of lines produced by the two types of standards are very complex, as shown in figure 6–3 for the $Au_{40}Cu_{60}$ alloy with many overlapped characteristic peaks of different families as shown in table 6–1.

The x-ray peak intensities were extracted from the spectrum by the top-hat filter as explained in section 5.4. The theoretical calculations of x-ray emission were made with our Monte Carlo program, which is described in section 5.1. Since

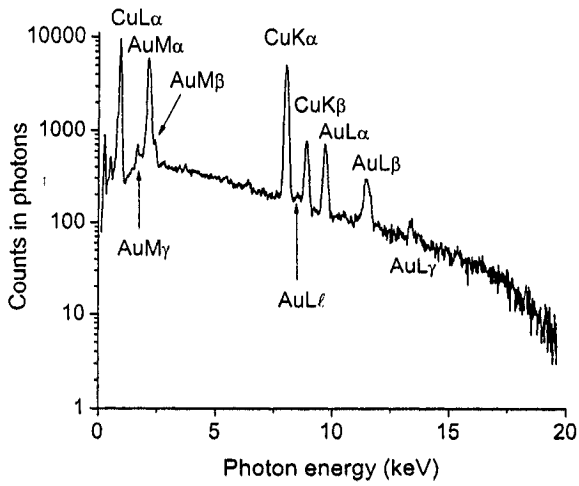

Figure 6–3: Full spectrum of the $Au_{40}Cu_{60}$ alloy at 20 keV

there are some overlapped peaks as shown in table 6–1, because of the typical low resolution of the EDS detector, the calculation of the ratio was done on the sum of the overlapped peaks in order to reduce the error introduced by peak deconvolution [106]. In table 6–1, the values were extracted from the Desktop Spectrum Analyzer (DTSA) program elaborated by the National Institute of Standards (NIST) available in their website [31]. These values were used a indicator of the absolute fraction of each characteristic lines, in order to determine which one must be computed.

The use of deconvolution programs adds errors, therefore it seemed interesting to check if it could be avoided. For simplification, that which is named the CuK line is the sum of $K\alpha 1$ and $K\alpha 2$ for Cu. For the same element, the CuL line in this work is Cu(Lα1+Lα2+Lβ1+Lβ4+Lη+Ll), AuL is Au(Lα1 + Lα2) and AgL is Ag(Lα1 + Lα2). Finally, AuM is for Au(Mα + Mβ). The number of lines included

Table 6–1: Table of computed characteristic x-rays [31]

Element	Subshell	Energy (keV)	Fraction	Subshell	Energy (keV)	Fraction
Au	Ma	2.12	1.0	Mb	2.20	0.60
Ag	La1	2.98	1.0	La2	2.98	0.11
Cu	Ka1	8.05	1.0	Ka2	8.03	0.50
Cu	La1	0.93	1.0	La2	0.93	0.12
Cu	Lb1	0.95	0.17	Lb4	1.02	0.02
Cu	Le	0.83	0.03	Ll	0.81	0.04

in the sum is determined by the difference in energy of the characteristic peaks, if it is included in the resolution of the EDS detector (around 150 eV) or not and as evaluated from measured spetra of the standards. The characteristic peaks of lower energy overlapped more x-rays lines than at higher energy. For instance:

$$f = \frac{AuM\alpha + AuM\beta}{AuM\alpha + AuM\beta + CuK\alpha 1 + CuK\alpha 2} \tag{6.1}$$

Since the $M\alpha$ line is generated by MV-subshell ionization, the $M\beta$ line by MIV ionization and the $K\alpha 1$ and the $K\alpha 2$ lines by K-shell ionization, the calibration factor for this system can be rewritten according equation 3.22:

$$\frac{I_{Cu}^{exp}}{I_{Au}^{exp}} = \Lambda_{Au-Cu} \frac{\sum_{peakCu} [\sigma_{Cu}\varpi_{Cu}P_{Cu}\epsilon_{Cu}F_{Cu}\gamma_{Cu}]}{\sum_{peakAu} [\sigma_{Au}\varpi_{Au}P_{Au}\epsilon_{Au}F_{Au}(1+T_{CK,Au})\gamma_{Au}]} \frac{A_{Au}}{A_{Cu}} \frac{C_{Cu}}{C_{Au}} \tag{6.2}$$

where $\sum_{peak}$ is the sum of emitted x-ray intensities of the overlapped peaks. The calibration factor Λ_{Au-Cu} accounts for the uncertainties of the parameters.

Figure 6–4 compares the ratio calculated with the theoretical line intensity and sum of line intensities as shown above. The vertical scale Y is the relative difference

between the ratios, for instance for AuM-CuK:

$$\begin{aligned} Y &= \frac{f_{line} - f_{peak}}{f_{peak}} \\ f_{line} &= \frac{I_{AuM\alpha}}{I_{AuM\alpha} + I_{CuK\alpha 1}} \\ f_{peak} &= \frac{I_{AuM\alpha} + I_{AuM\beta 1}}{I_{AuM\alpha} + I_{AuM\beta 1} + I_{CuK\alpha 1} + I_{CuK\alpha 2}} \end{aligned} \tag{6.3}$$

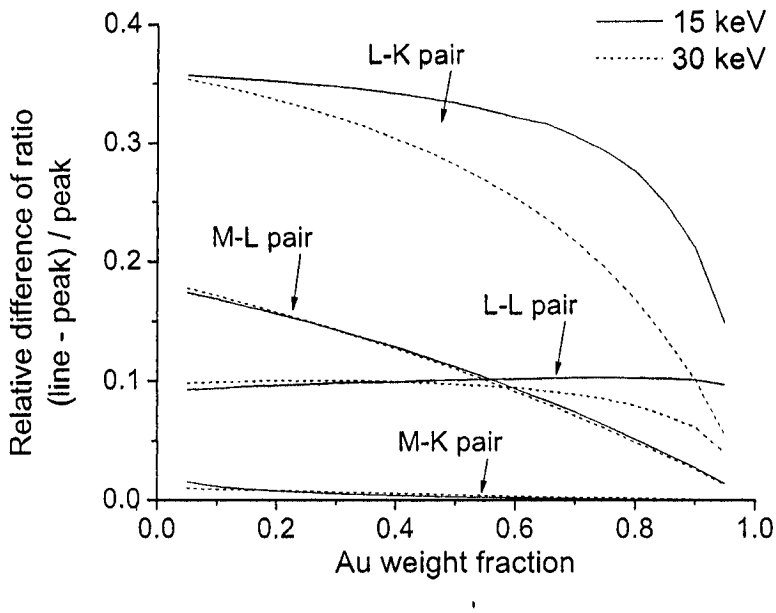

Figure 6–4: Calculated effect of the use of the overlapped peaks for the AuCu alloy, with respect to the composition and the electron beam energy, with theoretical ratios

In figure 6–4, the difference between 15 and 30 keV for the AuM-CuL and AuM-CuK pairs is negligible, while it progressively increases for the AuL-CuL pair for Au weight fraction above 50 % and is important for the AuL-CuK pair. The

minimum beam energy for each case is determine by the capability of extracting the characteristic x-ray intensity (10 keV for the lines below 5 keV and 15 keV for the higher energy lines). The beam energy effect due to the use of overlapped lines is negligible for the AuM-CuL and AuM-CuK pairs of lines. In order to reduce beam-energy dependency of the method, peak deconvolution should not therefore be necessary for the AuM-CuL and AuM-CuK pairs, while the use of the sum of the overlapped peaks instead of the deconvoluted characteristic lines is compensated by the calibration factor for the two other pairs.

Figure 6–5 shows the resolution flow-chart of the method. The first step is the qualitative microanalysis, in order to determine the elements in the materials. Then, the microanalysis conditions, such as the beam energy used for quantification, as well as the pair of lines to be used are determined, as well as the needed standards. Then calibration factors can be calculated. This can be done once, for a given material or element, or pair of element, and when needed. The theoretical calculations can be done also once for a certain material, with the same elements, in the case of binary systems. Then, the composition can be calculated using the calibration factor, the measured and calculated ratios.

With the different calibration factors calculated above, concentrations were calculated for the eight specimens at each beam energy. First, emitted x-ray intensities were calculated with the calculation program, either Monte Carlo or PAP, and for compositions ranging from 5 to 95 % of Au, with 5 % steps. Then, calibrated theoretical ratios were determined with the calculated x-ray intensities and with the

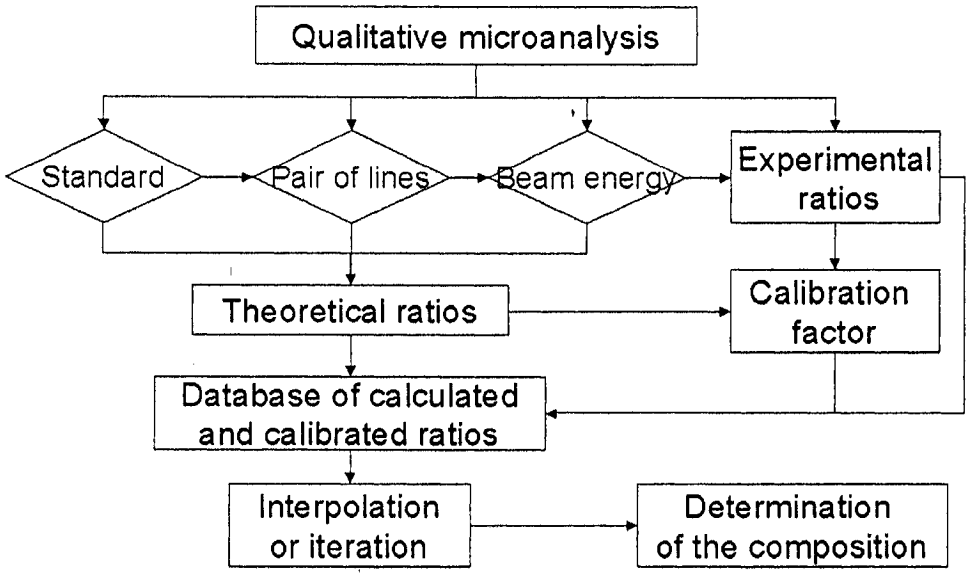

Figure 6–5: Resolution flow-chart of the method

calibration factor Λ:

$$f^{th} = \frac{I_A}{I_A + \Lambda I_B} \tag{6.4}$$

Then, the new theoretical calibrated ratios were compared with the experimental ratios, for each case, as in figure 6–6, in order to determine the Au weight fraction:

$$f^{th}(C) = f^{exp} \tag{6.5}$$

to calculate C by linear interpolation of the curve. f^{exp} is the calculated ratio. C is the researched weight fraction. If the ratio $f_1^{th}(C_1) \leq f^{th} \leq f_2^{th}(C_2)$, where 1 and 2 are two points in the calculated curve of the ratio versus the concentration, then:

$$C = \frac{f^{exp} \cdot (C_1 - C_2) - (f_2^{th} C_1 - f_1^{th} C_2)}{f_2^{th} - f_1^{th}} \tag{6.6}$$

considering that the curve is almost linear between C_1 and C_2, which must be close enough to respect this condition. Some calculation have been made with polynomial interpolation of the curves, and the calculated concentrations were found close to the value calculated with a linear interpolation.

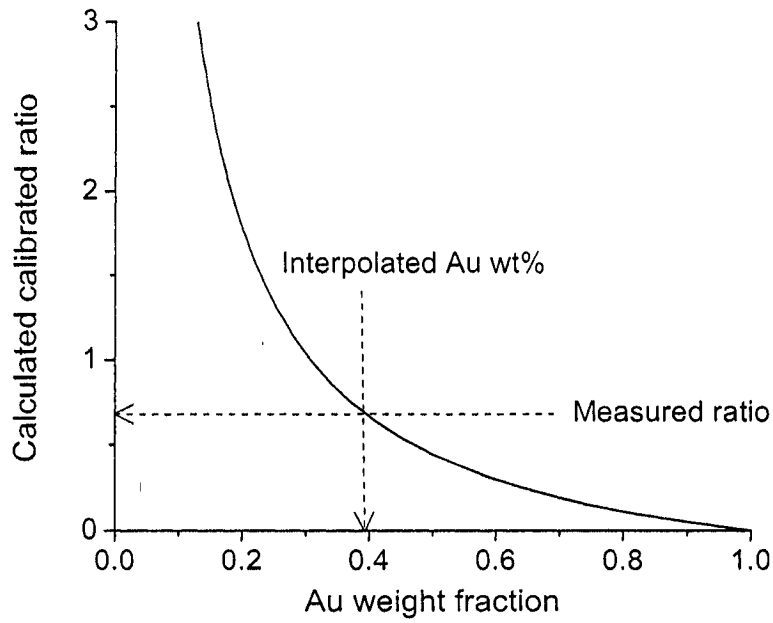

Figure 6–6: Interpolation of calculated theoretical ratios curve to determine the composition from an experimental measured ratio

6.2 Results

By default, and if not defined differently, x-ray intensities are calculated with the Monte Carlo program introduced in section 5.1. The fluorescence correction was not calculated. In appendix C, calculated weight fraction using the Monte Carlo program and the Salvat ionization cross-section for the L-shell ionization are shown. In appendix ??, the experimental characteristic intensities are presented.

In order to determine the effects of the beam energy, the composition of the standard and the type of x-ray characteristic lines, the calibration factors were calculated for the eight standards of AuCu and AuAg at different beam energies. The Au weight fraction was calculated with two types of calibration. The first set of calibration factors were the average of the calibration factors determined at each beam energy and for each standard. The second group of results used an energy-dependent calibration factor evaluated for one standard, $Au_{40}Cu_{60}$, because the use of only one standard is more practical and more realistic. Calibration factors are presented in section 6.2.4.

6.2.1 Relative error of estimation of the weight fraction

In the next tables, the average error $\overline{\varepsilon}$ is presented. The parameters are the beam energy, the energy of the peak used in the measurements and calculations:

$$\overline{\varepsilon} = \frac{1}{n} \sum_{n} |\varepsilon_i| \tag{6.7}$$

where n is the number of beam energies and ε_i is the relative error calculated for each beam energy and each standard calculated as in equation 6.8. For each measurement, the relative error ε_i was calculated with respect to the nominal Au weight fraction

and is given as the label above each column as:

$$\varepsilon_i = \frac{\left(C_{Au}^{calculated} - C_{Au}^{nominal}\right)}{C_{Au}^{nominal}} \tag{6.8}$$

Tables 6–2 and 6–3 show the comparison of the accuracy of the method in regard to the different possible pairs of peaks for the AuCu and AuAg alloys, as well as the Casnati [12] and the Salvat [93] models for the Cu K-shell ionization cross-sections. The composition was calculated with an average calibration factor, calculated from all the specimens at all the beam energies. The definition of the ratios is as follow:

$$AuL - CuK = f_{AuL} = \frac{AuL}{AuL + CuK} \tag{6.9}$$

All the ratios are similarly defined, depending of the pair of lines.

Table 6–2: Average total error of calculated Au weight fraction in AuCu with average calibration factors (S=Salvat, C=Casnati ionization cross-section)

	AuL-CuK (S-S)	AuL-CuK (S-C)	AuL-CuL (S-S)	AuM-CuK (C-S)	AuM-CuL (C-S)
20 % Au	9.68 %	18.76 %	15.56 %	25.1 %	10.96 %
40 % Au	6.92 %	13.06 %	12.73 %	18.47 %	17.67 %
60 % Au	5.92 %	9.77 %	7.98 %	12.68 %	16.56 %
80 % Au	2.62 %	4.58 %	3.73 %	5.18 %	9.56 %

Table 6–3: Average total error of calculated Au weight fraction in AuAg with average calibration factors (S=Salvat, C=Casnati ionization cross-section)

	AuL-AgL (S-S)	AuM-AgL (C-S)
20 % Au	11.75 %	12.14 %
40 % Au	5.02 %	8.16 %
60 % Au	4.06 %	7.07 %
80 % Au	3.92 %	4.74 %

Tables 6–4 and 6–6 present the compared average total error of estimation of the Au weight fraction with beam-dependent calibration factors, calculated with the $Au_{40}Cu_{60}$ alloy for the AuCu standards and the $Au_{60}Ag_{40}$ for the AuAg standards, because it is more experimentaly more practical to use one standard.

Table 6–4: Average total error of calculated Au weight fraction in AuCu with beam-energy-dependent calibration factors using Monte Carlo simulation (S=Salvat, C=Casnati ionization cross-section)

	AuL-CuK (S-S)	AuL-CuL (S-S)	AuM-CuK (C-S)	AuM-CuL (C-S)
20 % Au	2.85 %	9.01 %	6.70 %	15.27 %
60 % Au	2.15 %	7.24 %	7.42 %	6.23 %
80 % Au	0.83 %	3.58 %	5.95 %	5.52 %

Table 6–5: Average total error of calculated Au weight fraction in AuCu with beam-energy-dependent calibration factors using the Pouchou and Pichoir model (S=Salvat, C=Casnati ionization cross-section)

	AuL-CuK (S-S)	AuL-CuL (S-S)	AuM-CuK (C-S)	AuM-CuL (C-S)
20 % Au	2.81 %	14.09 %	8.11 %	20.60 %
60 % Au	2.62 %	7.73 %	8.22 %	8.03 %
80 % Au	5.84 %	4.60 %	6.74 %	6.90 %

Table 6–6: Average total error of calculated Au weight fraction in AuAg with beam-energy-dependent calibration factors (S=Salvat, C=Casnati ionization cross-section)

	AuL-AgL (S-S)	AuM-AgL (C-S)
20 % Au	15.92 %	17.76 %
40 % Au	3.24 %	9.58 %
80 % Au	2.32 %	3.43 %

The next tables presents the relative error to nominal composition of calculated Au weight fraction for the different pairs of lines, the AuCu and AgAg alloys, with

and without the continuum and characteristic fluorescence effect, with a constant and a beam-energy dependent calibration factor

Table 6–7: Relative error of calculated Au weight fraction using AuL-CuK pair of lines with average calibration factors without fluorescence correction

	15 keV	20 keV	25 keV	30 keV
20 % Au	20.52 %	-0.50 %	-1.41 %	-13.31 %
40 % Au	11.28 %	-1.28%	-5.42 %	-9.68 %
60 % Au	13.39 %	-0.89%	-3.59 %	-5.81 %
80 % Au	5.51 %	-0.49%	-1.93 %	-2.95 %

Table 6–8: Relative error of calculated Au weight fraction using the AuL-CuK pair of lines with an average calibration factor and with the fluorescence correction

	15 keV	20 keV	25 keV	30 keV
20 % Au	18.92 %	-2.78 %	-7.09 %	-15.85 %
40 % Au	8.89 %	-2.35%	-9.41 %	-13.87 %
60 % Au	8.43 %	-3.27%	-8.24 %	-10.90 %
80 % Au	3.99 %	-2.78%	-5.88 %	-7.52 %

Table 6–9: Relative error of calculated Au weight fraction using the AuL-CuL pair of lines with an average calibration factor and without the fluorescence correction

	15 keV	20 keV	25 keV	30 keV
20 % Au	-13.60 %	-27.39 %	4.42%	16.29%
40 % Au	-9.53 %	-14.90 %	12.91 %	23.58%
60 % Au	-0.12 %	-8.93 %	-3.40%	19.47%
80 % Au	1.10 %	-2.47%	0.33%	11.01%

Table 6–10: Relative error of calculated Au weight fraction using the AuL-CuL pair of lines with an average calibration factor and with the fluorescence correction

	15 keV	20 keV	25 keV	30 keV
20 % Au	-14.45 %	-29.19 %	1.58%	12.22%
40 % Au	-10.87 %	-17.52 %	6.71 %	17.07%
60 % Au	-2.06 %	-12.56%	-3.56%	2.64%
80 % Au	0.07 %	-5.48%	-1.01%	1.54%

Table 6–11: Relative error of calculated Au weight fraction using the AuM-CuK pair of lines with an average calibration factor and without the fluorescence correction

	15 keV	20 keV	25 keV	30 keV
20 % Au	18.73 %	23.64 %	-24.38 %	-33.65 %
40 % Au	16.42 %	20.05 %	-15.87 %	-21.55 %
60 % Au	12.44 %	14.42 %	12.13 %	-11.76 %
80 % Au	-1.14 %	8.07 %	7.14 %	-4.38 %

Table 6–12: Relative error of calculated Au weight fraction using the AuM-CuK pair of lines with an average calibration factor and with the fluorescence correction

	15 keV	20 keV	25 keV	30 keV
20 % Au	17.05 %	20.53 %	-26.10 %	-35.27 %
40 % Au	14.07 %	15.28 %	-19.19 %	-24.59 %
60 % Au	10.04 %	9.97 %	5.28 %	1.20 %
80 % Au	-2.87 %	5.36 %	3.05 %	0.38 %

Table 6–13: Relative error of calculated Au weight fraction using the AuM-CuL pair of lines with an average calibration factor

	10 keV	15 keV	20 keV	25 keV	30 keV
20 % Au	-11.47 %	7.33 %	15.33 %	7.48 %	13.18 %
40 % Au	0.82 %	14.61 %	20.96 %	20.98 %	30.96 %
60 % Au	2.95 %	13.21 %	17.54 %	26.76 %	31.31 %
80 % Au	2.63 %	7.95 %	10.60 %	13.78 %	15.13 %

Table 6–14: Relative error of calculated Au weight fraction using the AuM-AgL pair of lines with an average calibration factor

	10 keV	15 keV	20 keV	25 keV	30 keV
20 % Au	-16.28 %	-7.48 %	-19.11 %	-8.64 %	-9.21 %
40 % Au	-17.40 %	-11.92 %	-4.31 %	1.96%	-5.22 %
60 % Au	-20.13%	-1.83%	2.83 %	3.53 %	6.57 %
80 % Au	-4.73%	-1.29 %	4.53 %	5.83 %	6.93 %

Table 6–15: Relative error of calculated Au weight fraction using the AuL-AgL pair of lines with an average calibration factor and without the fluorescence correction

	15 keV	20 keV	25 keV	30 keV
20 % Au	-22.67 %	-18.21 %	3.01 %	3.11 %
40 % Au	-6.02 %	1.65 %	4.51 %	7.90 %
60 % Au	0.81 %	3.69 %	5.33 %	6.43 %
80 % Au	-0.83 %	2.91 %	5.44 %	3.49 %

Table 6–16: Relative error of calculated Au weight fraction using the AuL-AgL pair of lines with an average calibration factor and with the fluorescence correction

	15 keV	20 keV	25 keV	30 keV
20 % Au	-28.15 %	-22.19 %	-1.41 %	-0.33 %
40 % Au	20.53 %	-2.18 %	1.32 %	5.84 %
60 % Au	-3.43 %	0.92 %	2.82 %	4.45 %
80 % Au	-2.73 %	1.65 %	4.33 %	5.59 %

Table 6–17: Relative error of calculated Au weight fraction using the AuL-CuK pair of lines with a beam-energy-dependent calibration factor and without the fluorescence correction

	15 keV	20 keV	25 keV	30 keV
20 % Au	5.38 %	-2.45 %	2.78 %	0.81 %
60 % Au	7.29 %	0.00 %	0.15 %	1.16 %
80 % Au	2.56 %	0.08%	0.04 %	0.65 %

Table 6–18: Relative error of calculated Au weight fraction using the AuL-CuK pair of lines with a beam-energy-dependent calibration factor and with the fluorescence correction

	15 keV	20 keV	25 keV	30 keV
20 % Au	5.45 %	-3.61 %	1.1 %	-2.41 %
60 % Au	7.52 %	0.82 %	1.39 %	2.69 %
80 % Au	2.78 %	1.04 %	1.42 %	2.28 %

Table 6–19: Relative error of calculated Au weight fraction using the AuL-CuL pair of lines with a beam-energy-dependent calibration factor and without the fluorescence correction

	15 keV	20 keV	25 keV	30 keV
20 % Au	0.09 %	-11.24 %	9.13 %	15.59 %
60 % Au	10.38 %	2.19 %	-11.19 %	-5.22%
80 % Au	3.81 %	2.76%	-3.11 %	-4.64 %

Table 6–20: Relative error of calculated Au weight fraction using the AuL-CuL pair of lines with a beam-energy-dependent calibration factor and with the fluorescence correction

	15 keV	20 keV	25 keV	30 keV
20 % Au	0.02 %	-11.51 %	9.3 %	3.4 %
60 % Au	9.3 %	2.16 %	-6.06 %	-7.82%
80 % Au	3.4 %	2.65%	-1.04 %	-1.77 %

Table 6–21: Relative error of calculated Au weight fraction using the AuM-CuK pair of lines with a beam-energy-dependent calibration factor and without the fluorescence correction

	15 keV	20 keV	25 keV	30 keV
20 % Au	-4.19 %	-2.94 %	-5.74 %	-10.94 %
60 % Au	3.14 %	2.56 %	21.42 %	2.58 %
80 % Au	-6.9 %	2.74 %	11.00 %	3.18 %

Table 6–22: Relative error of calculated Au weight fraction using the AuM-CuK pair of lines with a beam-energy-dependent calibration factor and with the fluorescence correction

	15 keV	20 keV	25 keV	30 keV
20 % Au	-5.37 %	-5.31 %	-8.67 %	-13.84 %
60 % Au	3.98 %	4.12 %	24.08 %	4.90 %
80 % Au	-5.90 %	4.47 %	12.61 %	5.56 %

Table 6–23: Relative error of calculated Au weight fraction using the AuM-CuL pair of lines with a beam-energy-dependent calibration factor

	10 keV	15 keV	20 keV	25 keV	30 keV
20 % Au	-12.52 %	-9.34 %	-11.72 %	-17.43 %	-25.35 %
60 % Au	2.37 %	4.83 %	4.83 %	12.44 %	6.68 %
80 % Au	2.35 %	4.4 %	5.4 %	8.53 %	6.94 %

Table 6–24: Relative error of calculated Au weight fraction using the AuM-AgL pair of lines with a beam-energy-dependent calibration factor

	10 keV	15 keV	20 keV	25 keV	30 keV
20 % Au	23.97 %	-3.95 %	-24.14 %	-15.23 %	-24.54 %
40 % Au	11.53 %	9.17 %	-8.40 %	-3.38%	-15.41 %
80 % Au	4.98 %	-0.31%	3.24%	4.25 %	4.36 %

Table 6–25: Relative error of calculated Au weight fraction using the AuL-AgL pair of lines with a beam-energy-dependent calibration factor and without the fluorescence correction

	15 keV	20 keV	25 keV	30 keV
20 % Au	-23.94 %	-23.67 %	-6.92 %	-9.40 %
40 % Au	5.09 %	-3.69 %	-2.75 %	-1.43 %
80 % Au	-1.32 %	1.25 %	3.12 %	3.60 %

Table 6–26: Relative error of calculated Au weight fraction using the AuL-AgL pair of lines with a beam-energy-dependent calibration factor and with the fluorescence correction

	15 keV	20 keV	25 keV	30 keV
20 % Au	-23.59 %	-23.53 %	-6.66 %	-9.11 %
40 % Au	34.84 %	-3.59 %	-2.28 %	-1.31 %
80 % Au	-1.34 %	1.23 %	3.08 %	3.56 %

6.2.2 Calculated weight fraction with the Monte Carlo method

The following section presents the calculated Au weight fraction for different conditions and for the eight alloys.

AuL-CuK pair for the AuCu standards

The AuL-CuK pair of lines (Lα1 is centered around 9.71 keV and Cu$K\alpha$1 8.05 keV respectively) were used to calculate the Au weight fraction. This is shown in figure 6–7 with the Salvat ionization cross-section for both K and L lines. In order to observe the effect of the choice of ionization cross-section model on the accuracy, another set of results was computed with the Casnati ionization cross-section [12] for the K line and the Salvat cross-section [93] for the L lines (figure 6–8). Both were calculated with a constant calibration factor. Figure 6–9 presents the Au weight fraction computed with a beam-energy-dependent calibration factor. In this last, the relative estimation error ranges below 3 %, except at 15 keV.

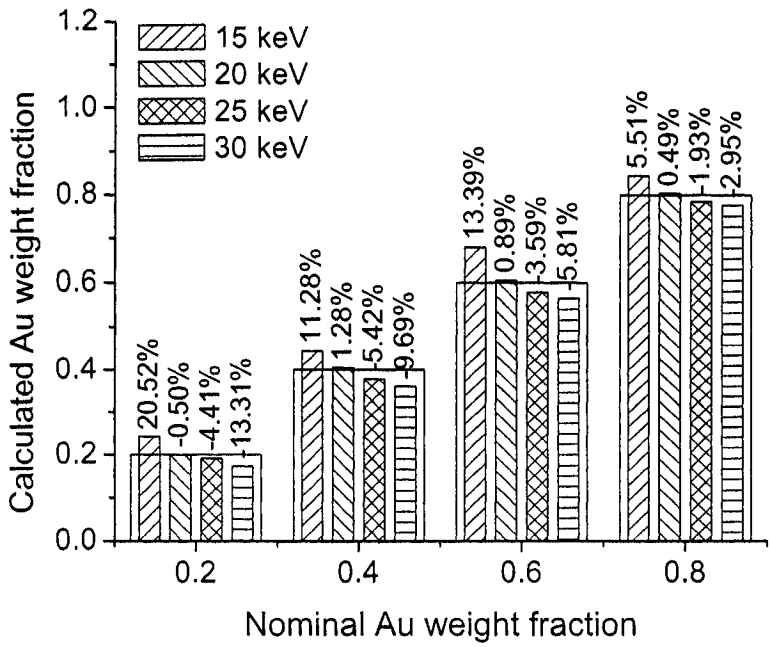

Figure 6–7: Calculated weight fraction of Au in the AuCu alloys for the pair AuL-CuK using the Salvat ionization cross-section [93] for the K and L lines, with an average calibration factor

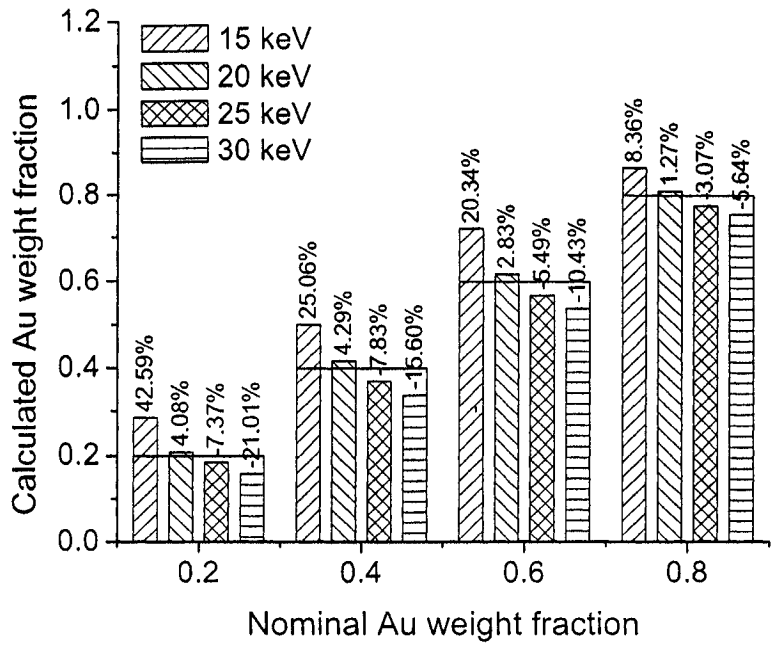

Figure 6–8: Calculated weight fraction of Au in the AuCu alloys for the pair AuL-CuK with the Casnati ionization cross-section [12] for the K line, and the Salvat ionization cross-section [93] for the L line, with an average calibration factor

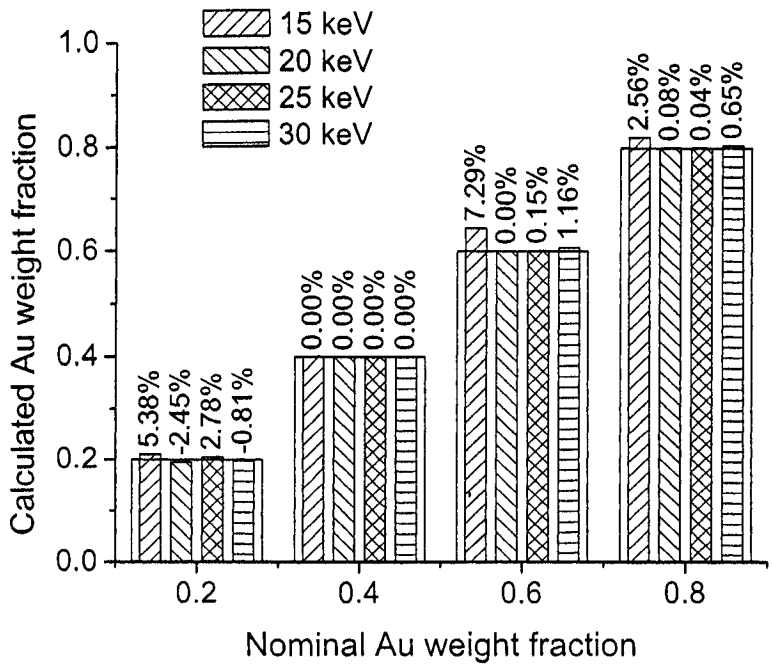

Figure 6–9: Calculated weight fraction of Au in the AuCu alloys for the pair AuL-CuK calibrated using the $Au_{40}Cu_{60}$ standard with a beam-energy-dependent calibration factor

AuL-CuL pair for the AuCu standards

Figure 6–10 presents the calculated Au weight fraction using the AuL-CuL pair (centered at 9,71 and 0.93 keV, respectively) in the AuCu alloys, with a constant calibration as in table 6–27. The percentage of Au is generally underestimated except at 30 keV. The errors of estimation are much larger than for the AuL-CuK pair and are also scattered from -27 % to +24 %.

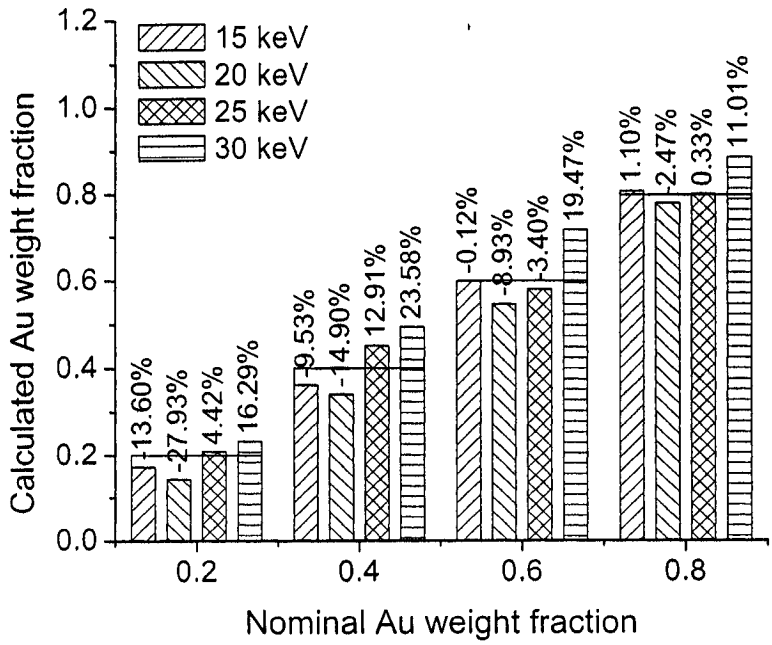

Figure 6–10: Calculated weight fraction of Au in the AuCu alloys for the pair AuL-CuL using an average calibration factor

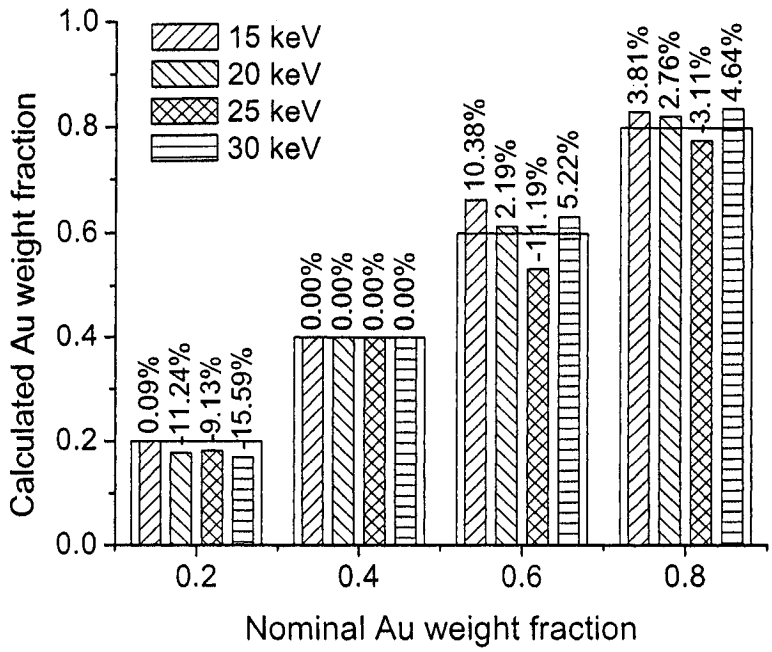

Figure 6–11: Calculated weight fraction of Au in the AuCu alloys for the pair AuL-CuL calibrated using the $Au_{40}Cu_{60}$ standard with a beam-energy-dependent calibration factor

Figure 6–11 presents the results for the AuL-CuL pair calculated with a beam-energy-dependent calibration factor. The relative error is higher than for the AuL-CuK pair, but below 12 % in most cases. The relative error of the Au weight fraction is much better than with a constant calibration factor, but inconsistency is observed at 15 keV for 60 and 80 % of Au.

AuM-CuK pair for the AuCu standards

The Au composition calculated using the Mα centered peak of Au (2.13 keV) and Kα1 centered peak of Cu (8.04 keV), with the CuK Salvat ionization cross-section [93] and an average calibration factor is shown in figure 6–12. Figure 6–13 shows the calculated Au fraction for the AuM-CuK pair with a beam-energy-dependent calibration factor.

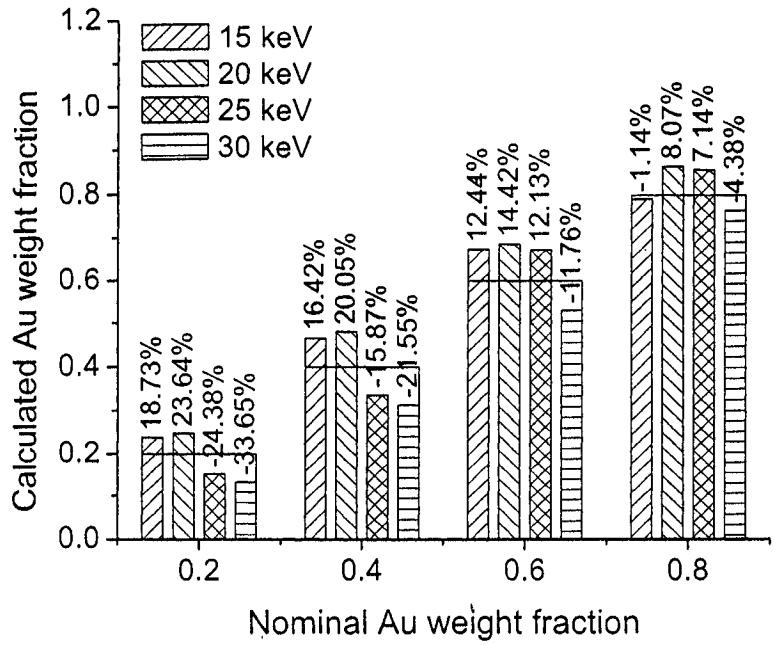

Figure 6–12: Calculated weight fraction of Au in the AuCu alloys for the pair AuM-CuK using the Casnati ionization cross-section [12] for the AuM line and Salvat ionization cross-section [93] for the CuK line, with an average calibration factor

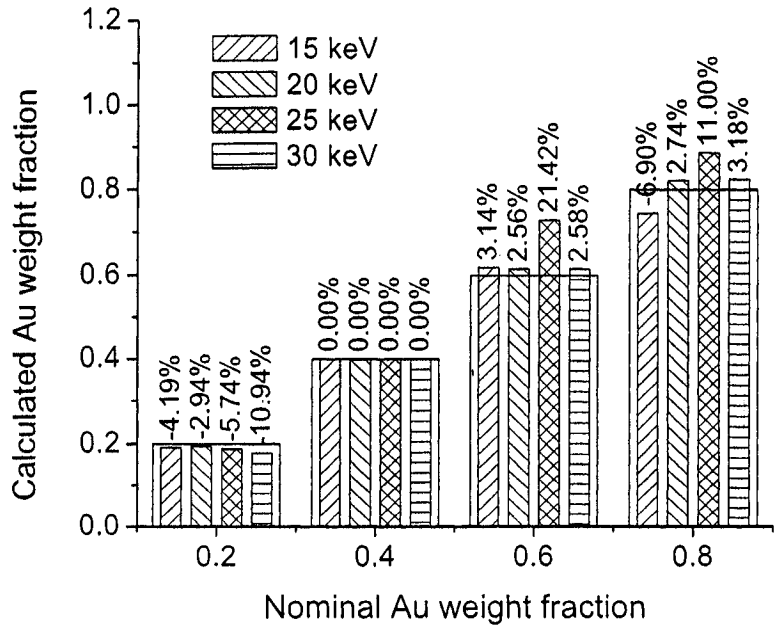

Figure 6–13: Calculated weight fraction of Au in the AuCu alloys for the pair AuM-CuK calibrated using the $Au_{40}Cu_{60}$ standard and with a beam-energy-dependent calibration factor

AuM-CuL pair for the AuCu standards

Figure 6–14 presents the calculated weight fraction of Au using the AuM-CuL pair. In this figure, the calibration factor is constant for all energies and specimens. Finally, figure 6–15 shows the results for the AuM-CuL pair with a beam-energy-dependent calibration factor.

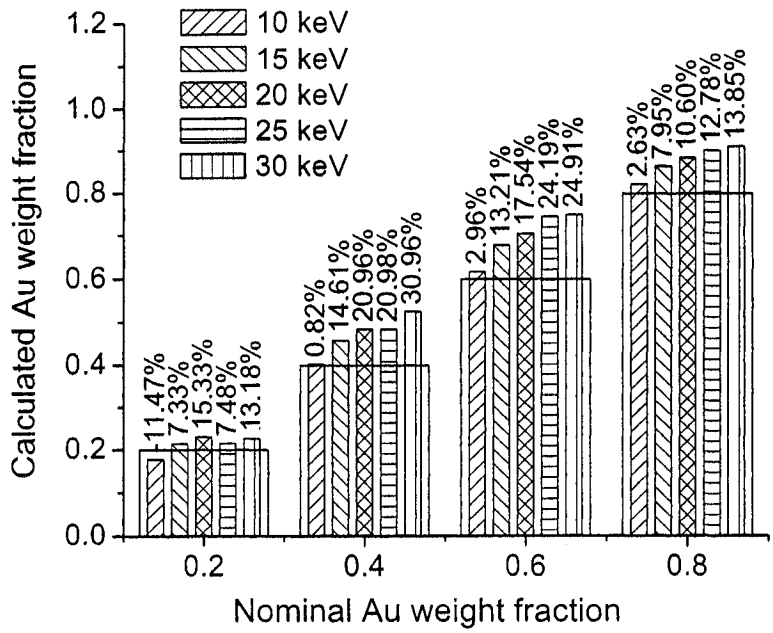

Figure 6–14: Calculated weight fraction of Au in the AuCu alloys for the pair AuM-CuL using an average calibration factor

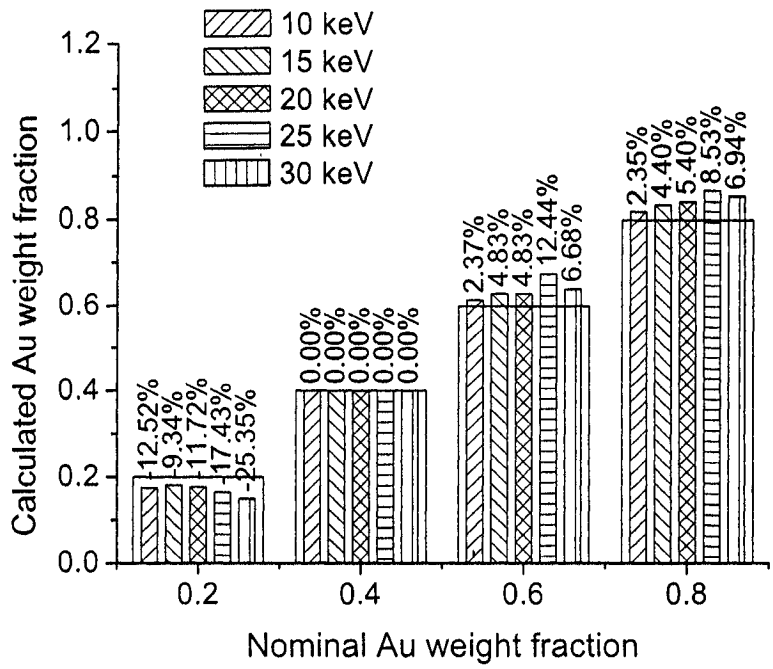

Figure 6–15: Calculated weight fraction of Au in the AuCu alloys for the pair AuM-CuL calibrated using the $Au_{40}Cu_{60}$ standard with a beam-energy-dependent calibration factor

AuL-AgL pair for the AuAg standards

Figure 6–16 presents the calculated Au weight fraction for the AuL-AgL pair of lines with a constant calibration factor. The beam-energy-dependent calibration factor was used to calculate the Au weight fraction in figure 6–17. The analysis of the measured peak intensities in the AuAg spectra showed large discrepancies in the measured ratios. In order to ensure statistical stability, seventeen values of the AuM or AgL peak intensities were taken out (from eighty spectra), where the ratios were lower than half and higher than twice the average value. Except for 20 % of Au weight fraction at 10 and 15 keV, one value maximum was eliminated (out of four measurements).

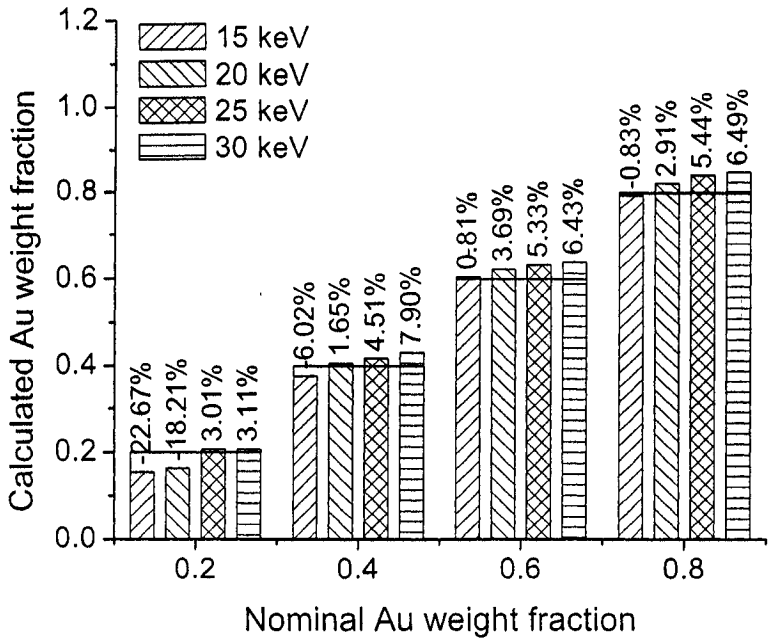

Figure 6–16: Calculated weight fraction of Au in the AuAg alloys for the pair AuL-AgL using an average calibration factor

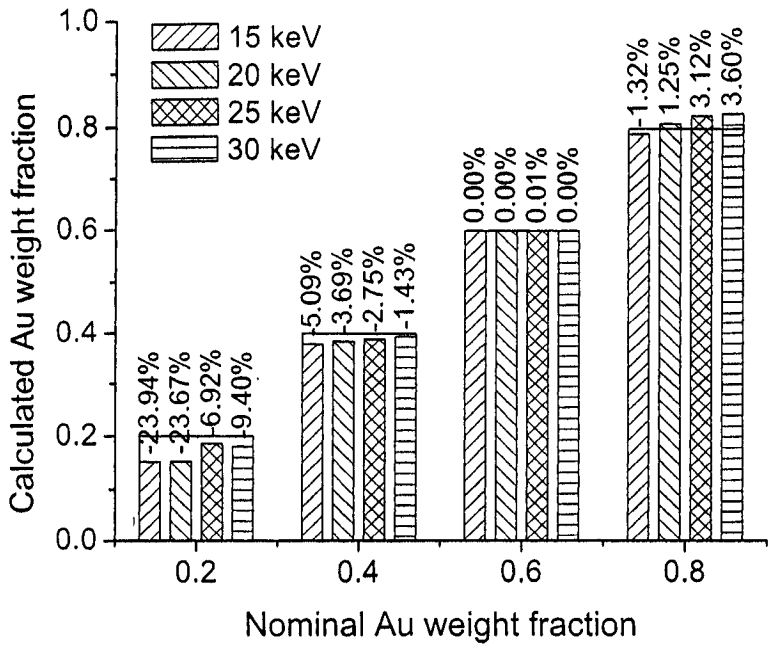

Figure 6–17: Calculated weight fraction of Au in the AuAg alloys for the pair AuL-AgL calibrated using the $Au_{60}Ag_{40}$ standard with a beam-energy-dependent calibration factor

AuM-AgL pair for the AuAg standards

Figure 6–18 displays the Au fraction calculated using the AuM-AgL pair with an average calibration. The calibration factor dependent on the beam energy is used to calculate the Au fraction for the results shown in figure 6–19. Seventeen values of the AuM or AgL peak intensities were taken out (from eighty spectra) if the measured ratio was lower than half and higher than twice the average value. Except for 20 % of Au weight fraction, one value at maximum among four measurements was discarded.

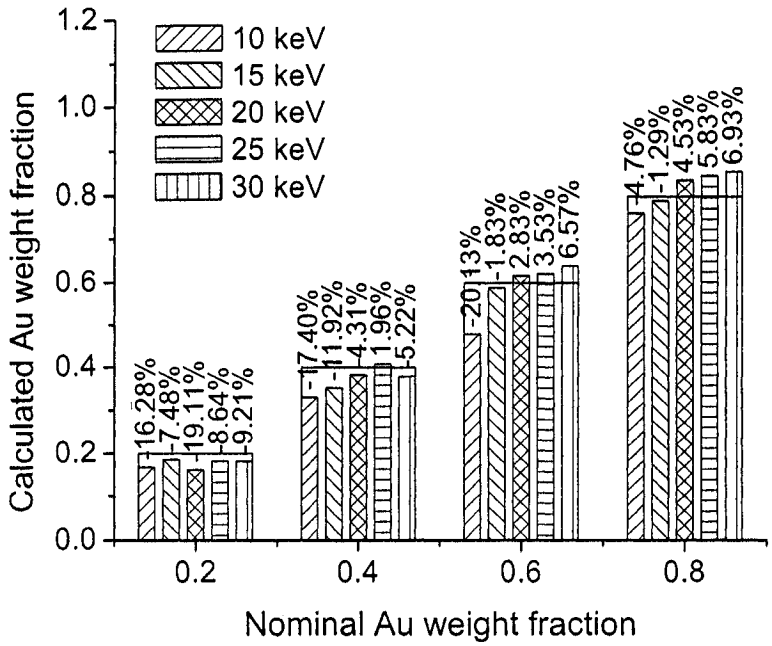

Figure 6–18: Calculated weight fraction of Au in the AuAg alloys for the pair AuM-AgL using an average calibration

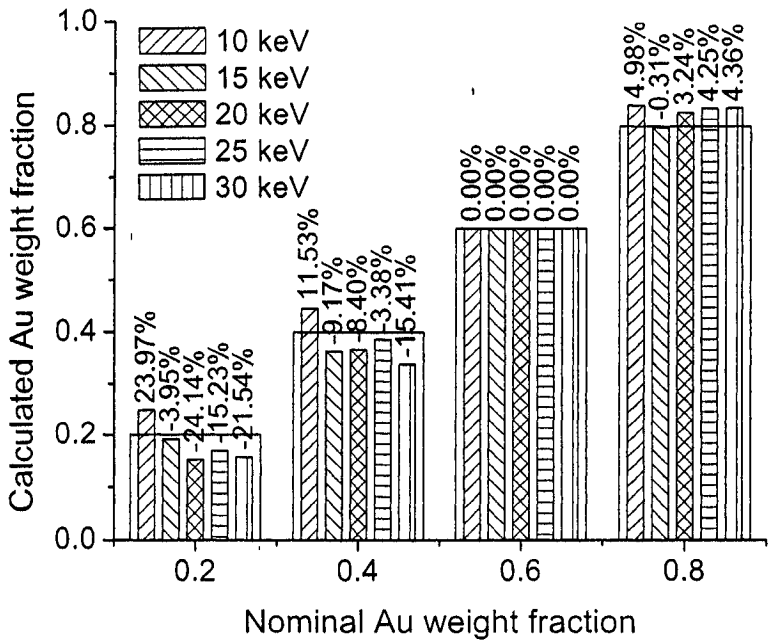

Figure 6–19: Calculated weight fraction of Au in the AuAg alloys for the pair AuM-AgL calibrated using the $Au_{60}Ag_{40}$ standard with a beam-energy-dependent calibration factor

6.2.3 Calculated weight fraction with the Pouchou and Pichoir model

In the next figures, the theoretical ratio was calculated with the Pouchou and Pichoir model [77] as described in section 5.2. Figures 6–20, 6–21, 6–22 and 6–23 present the Au weight fraction calculated with a beam-energy-dependent calibration factor.

AuL-CuK pair for the AuCu standards

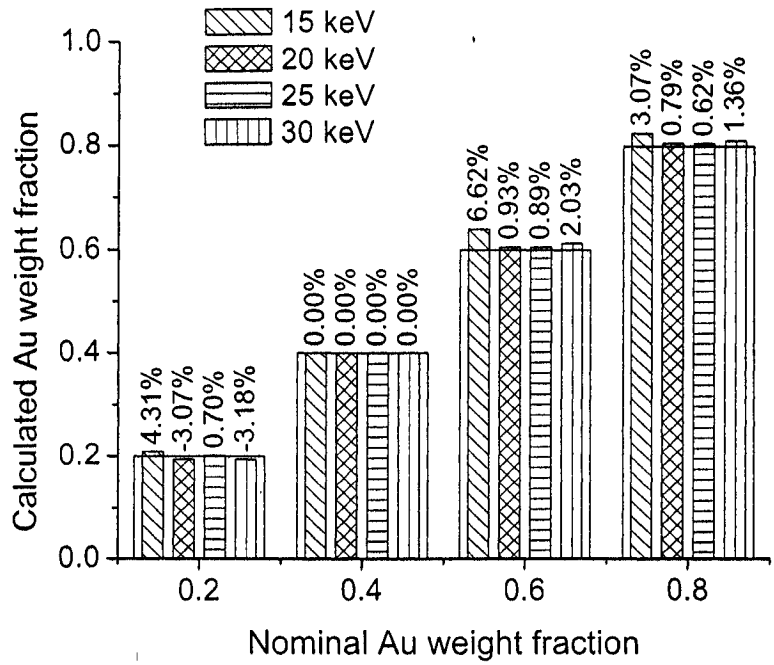

Figure 6–20: Calculated weight fraction of Au in the AuCu alloys for the pair AuL-CuK calibrated using the $Au_{40}Cu_{60}$ standard with the PAP model and with a beam-energy-dependent calibration factor

AuL-CuL pair for the AuCu standards

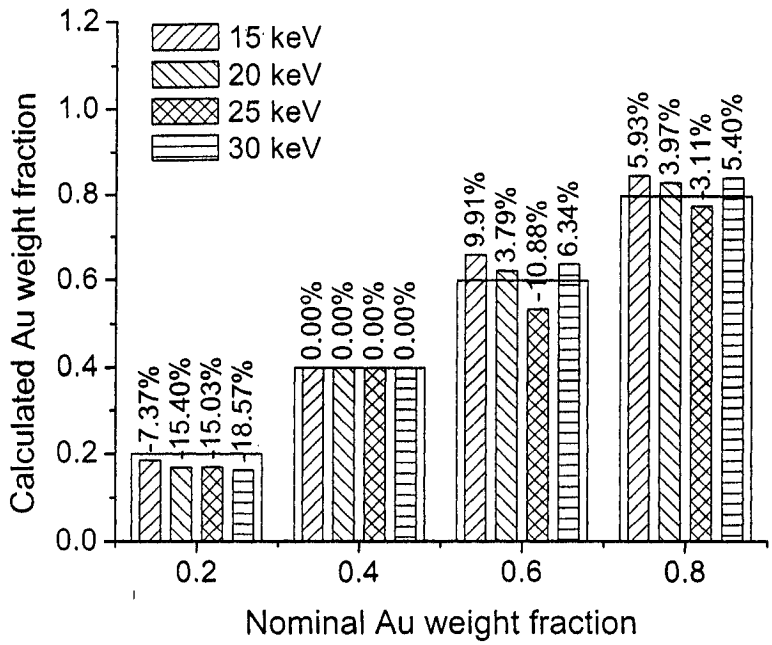

Figure 6–21: Calculated weight fraction of Au in the AuCu alloys for the pair AuL-CuL calibrated using the $Au_{40}Cu_{60}$ standard with the PAP model with a beam-energy-dependent calibration factor

AuM-CuK pair for the AuCu standards

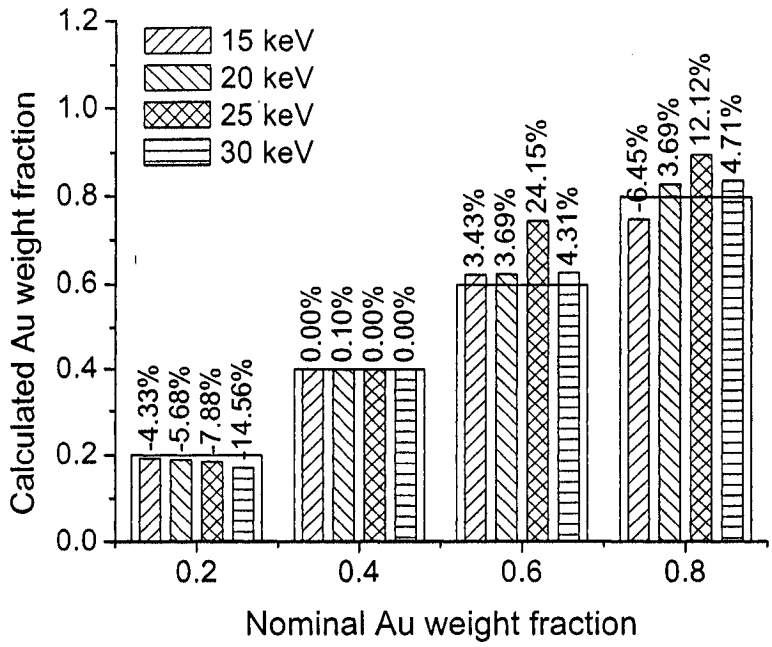

Figure 6–22: Calculated weight fraction of Au in the AuCu alloys for the pair AuM-CuK calibrated using the $Au_{40}Cu_{60}$ standard with the PAP model with a beam-energy-dependent calibration factor

AuM-CuL pair for the AuCu standards

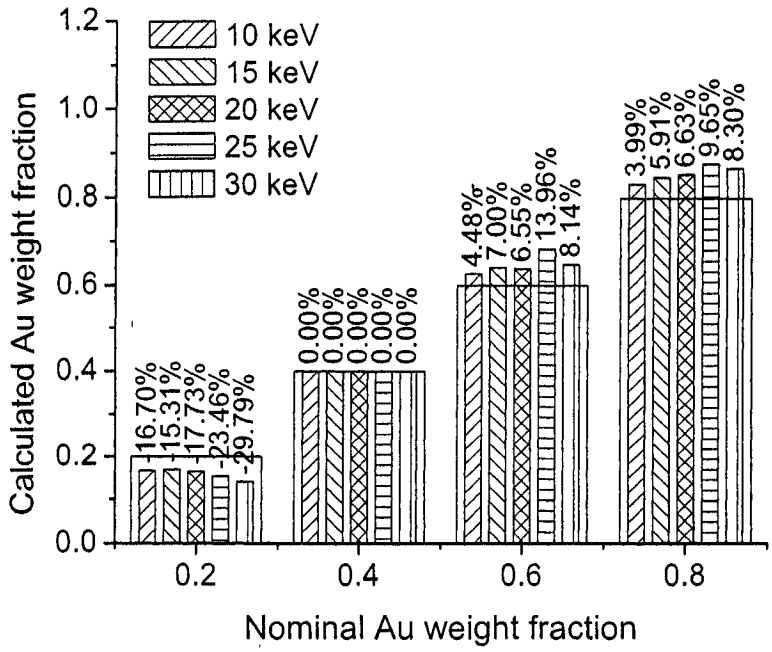

Figure 6–23: Calculated weight fraction of Au in the AuCu alloys for the pair AuM-CuL calibrated using the $Au_{40}Cu_{60}$ standard with the PAP model with a beam-energy-dependent calibration factor

6.2.4 Calculated calibration factors

As explained above, the Au weight fraction was calculated with a constant and a variable calibration factor. Table 6–27 shows the average value of the calculated calibration factors for all the beam energies and the standards. The estimated absolute error is the standard deviation of the calculated ratios for all conditions. The evaluation of the relative error of the Au weight fraction permits the evaluation of the trend of the accuracy. Three decimal places are given for clarity, while four are used

in calculations. Table 6–28 shows another set of calibration factors, calculated for each beam energy and calculated for the $Au_{40}Cu_{60}$ and $Au_{60}Ag_{40}$ alloys, respectively.

Table 6–27: Average calibration factors for the AuCu and AuAg alloys with the absolute error range (standard deviation of the measurements)

AuCu alloys	Calibration factor
AuM-CuK	3.235 ± 1.152
AuM-CuL	0.472 ± 0.134
AuL-CuK	0.646 ± 0.105
AuL-CuL	0.092 ± 0.026
AuAg alloys	Calibration factor
AuL-AgL	1.252 ± 0.227
AuM-AgL	0.393 ± 0.093

Table 6–28: Beam-energy-dependent calibration factors for $Au_{40}Cu_{60}$ and $Au_{60}Ag_{40}$ respectively

$Au_{40}Cu_{60}$	10 keV	15 keV	20 keV	25 keV	30 keV
AuM-CuK		2.510 ±0.025	2.347±0.025	4.235±0.090	4.690±0.091
AuM-CuL	0.639±0.012	0.519±0.005	0.453± 0.021	0.459±0.011	0.385±0.008
AuL-CuK		0.538±0.032	0.630±0.011	0.710±0.015	0.771±0.013
AuL-CuL		0.111±0.007	0.121±0.004	0.077±0.001	0.063±0.002
$Au_{60}Ag_{40}$	10 keV	15 keV	20 keV	25 keV	30 keV
AuL-AgL		0.385±0.042	0.357±0.019	0.345±0.024	0.331±0.034
AuM-AgL	2.062±0.518	1.315±0.047	1.162±0.061	1.138±0.033	1.042±0.084

The calculated factors for the AuCu alloys are shown in figure 6–24 for the pairs AuL-CuK, figure 6–25 for the pairs AuL-CuL, figure 6–26 for the pairs AuM-CuK and figure 6–27 for the pairs AuM-CuL. Figures 6–28 and 6–29 show the calibration factors for the AuAg alloys, for the AuL-AgL and AuM-AgL pairs respectively.

The error bars are calculated using the formula presented in equation 3.21. The value of Δf is the standard deviation of the experimental ratio, calculated with the four experimental spectra obtained for each condition because the exact value cannot be properly evaluated. The necessary data to determine the experimental error (from the equipment) are not available, therefore it is difficult to estimate the real error. The standard deviation permits the estimation of a range of confidence for the calibration factor. Measurement, extraction and statistical errors are included in a function g that may not be linear:

$$\Delta f = g\left(\epsilon(measurement), \epsilon(extraction), \epsilon(statistics)\right) \tag{6.10}$$

AuL-CuK pair for AuCu standards

The error bars for the AuL-CuK lines overlap in figure 6–24. The calibration factor for the AuL-CuK lines seems quite independent of the standard composition, except at 15 keV, since the range of confidence of the calibration factor includes all the values.

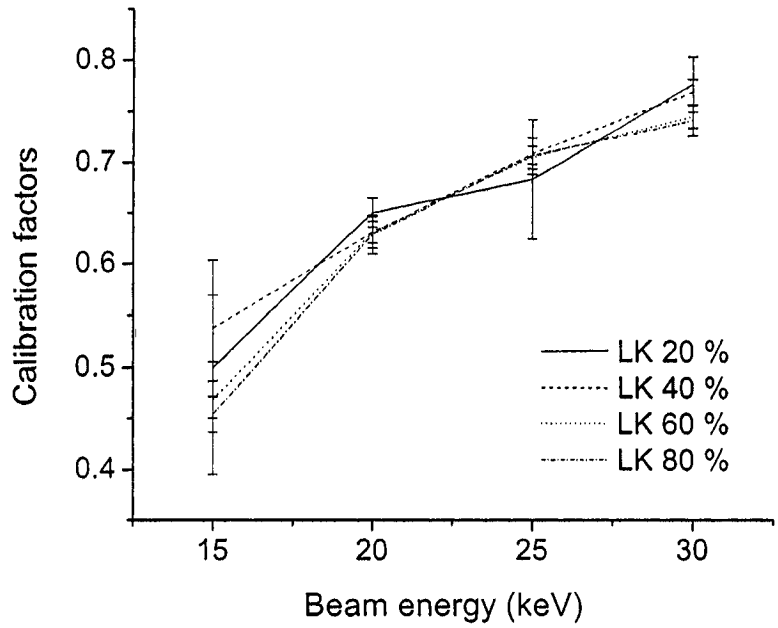

Figure 6–24: Calibration factors for the four AuCu alloys for the pairs AuL-CuK

AuL-CuL pair for the AuCu standards

Calibration factors for the AuL-CuL lines in figure 6–25 are smaller than 1 and indicate a maximum at 20 keV. Moreover, the curves shows a slight dependence on the weight fraction of Au. Some error bars at 25 keV overlap.

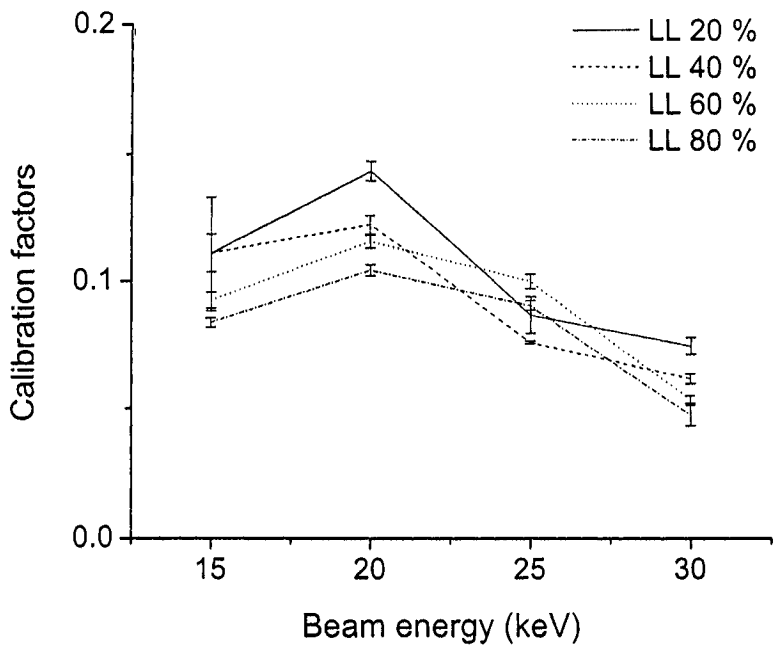

Figure 6–25: Calibration factors for the four AuCu alloys for the pairs AuL-CuL

AuM-CuK pair for the AuCu standards

The calibration factors for the AuM-CuK pair of lines in figure 6–26 are significantly above 1 and present large discontinuities at 25 keV. Once again, the error bars are large at 15 keV. The composition effect globally increases with beam energy. This calibration factor presents a minimum at 20 keV and 25 keV for 60 % and 80 % of Au.

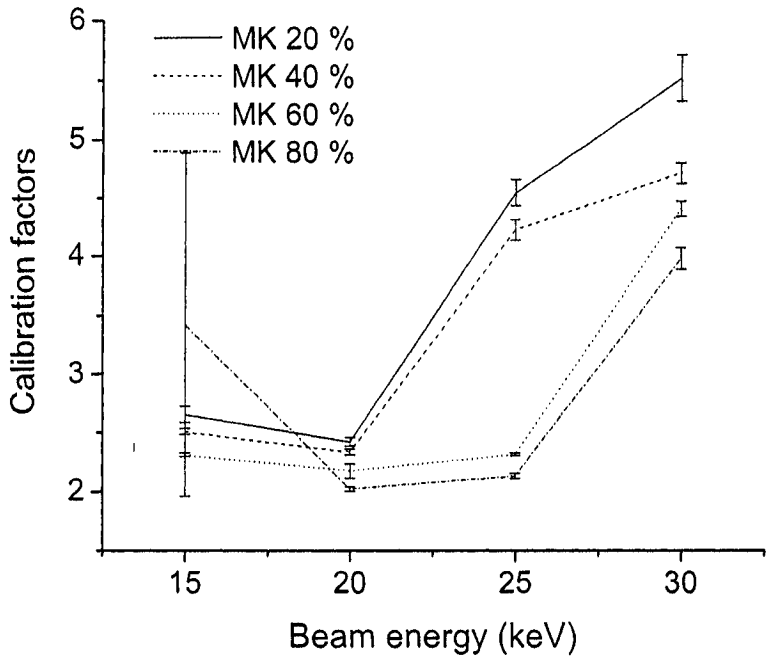

Figure 6–26: Calibration factors for the four AuCu alloys for the pairs AuM-CuK

AuM-CuL pair for the AuCu standards

The calibration factors for the AuM-CuL lines in figure 6–27 show a continuous decrease with the beam energy, with a clear dependence on the Au weight fraction. The trend shows a correlation between the different calibration factors which follow a similar slope. Once again, a clear difference in the trend is observed at 25 keV.

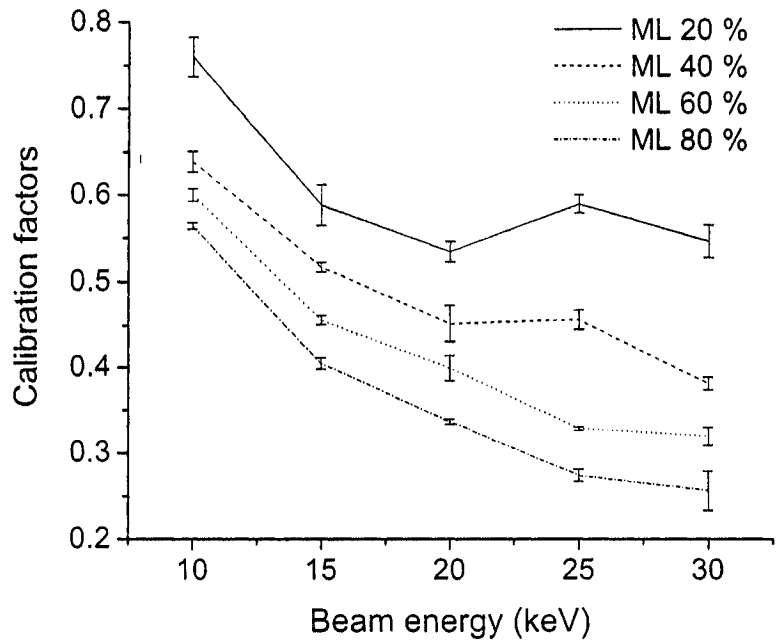

Figure 6–27: Calibration factors for the four AuCu alloys for the AuM-CuL pair

AuL-AgL pair for the AuAg standards

The error bars indicate wide discrepancies of the values of extracted intensities in figure 6–28, particularly at 15 keV. For the AuL-AgL pair, the composition dependence is weak, contrary to what happens in the AuCu alloys, and seems constant with the beam energy.

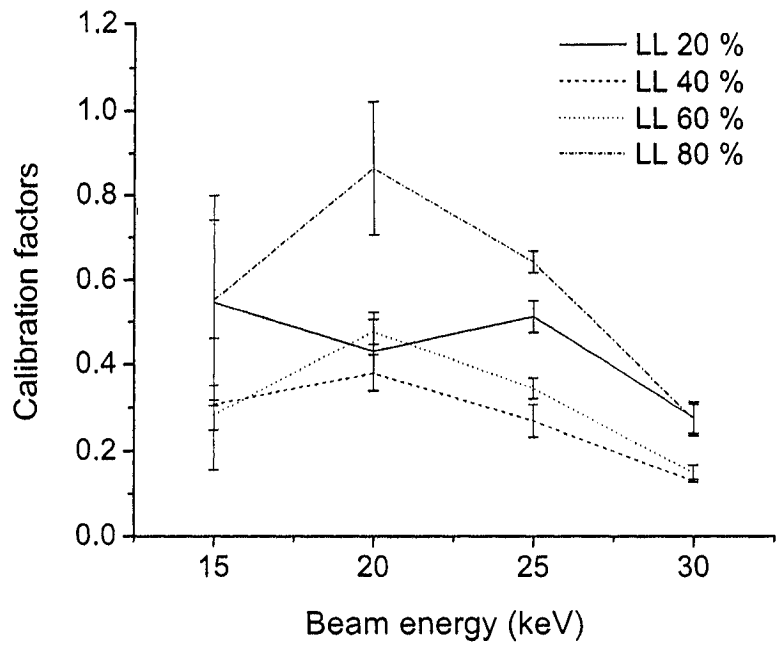

Figure 6–28: Calibration factors for the four AuAg alloys for the AuL-AgL pair

AuM-AgL pair for the AuAg standards

The composition effect is more important for the M-L pair as shown in figure 6–29, but increases with the beam energy. The error bars mainly overlap, therefore the composition effect could be caused by experimental scattering of measurements at 15 and 20 keV.

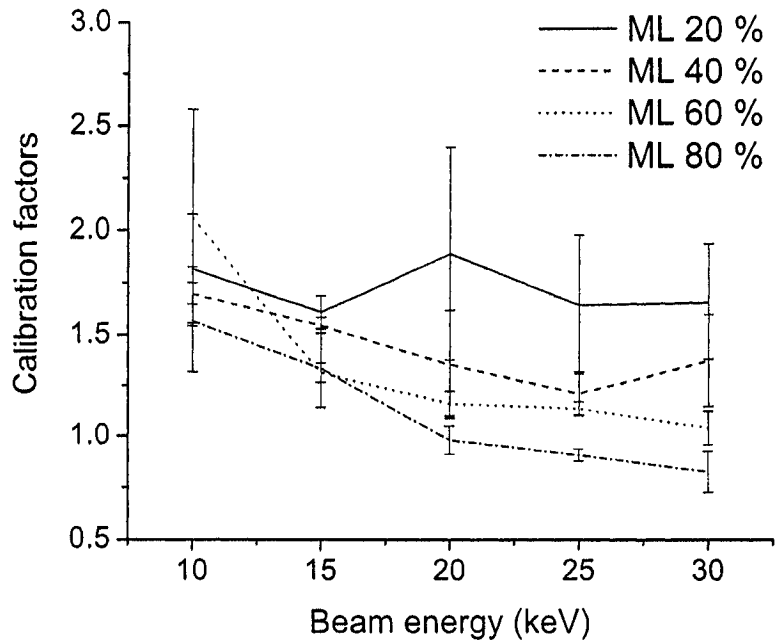

Figure 6–29: Calibration factors for the four AuAg alloys for the AuM-AgL pair

6.3 Interpretation of the results

6.3.1 Effect of the beam energy

A first study of beam energy dependence on the quantification was carried out with the AuAg alloys at 10 and 30 keV. Constant calibration factors were determined at 10 and 30 keV, and the specimen compositions were quantified at these two beam energies with the two different calibration factors. Figure 6–30 shows the calculated Au weight fraction for these four conditions. The straight line shows the ideal position of the points, where the calculated weight fraction is equal to the nominal one. The coefficient of determination R^2 decreases when the beam energy of the microanalysis is different from the beam energy of the calibration. However, the quality of the composition evaluation remains quite acceptable, since the coefficient of determination stays above 0.97.

This graph also enhances the dependence of the accuracy on the beam energy. Optimum conditions must be determined, with a cautiously chosen calibration factor and an adequate beam energy. Otherwise, a beam-energy-dependent calibration factor is proposed. However, it must be kept in mind that an increase in the beam voltage causes a loss in spatial resolution, but an increase in the number of counts and therefore statistical stability for high energy peaks, and a decrease for low-energy characteristic x-rays.

Almost all calibration factors show a dependence on the beam energy, probably linked with the inaccuracies of the physical models of x-ray generation (particularly the ionization cross-sections and the mass-absorption coefficient) which are more significant for low energy characteristic lines.

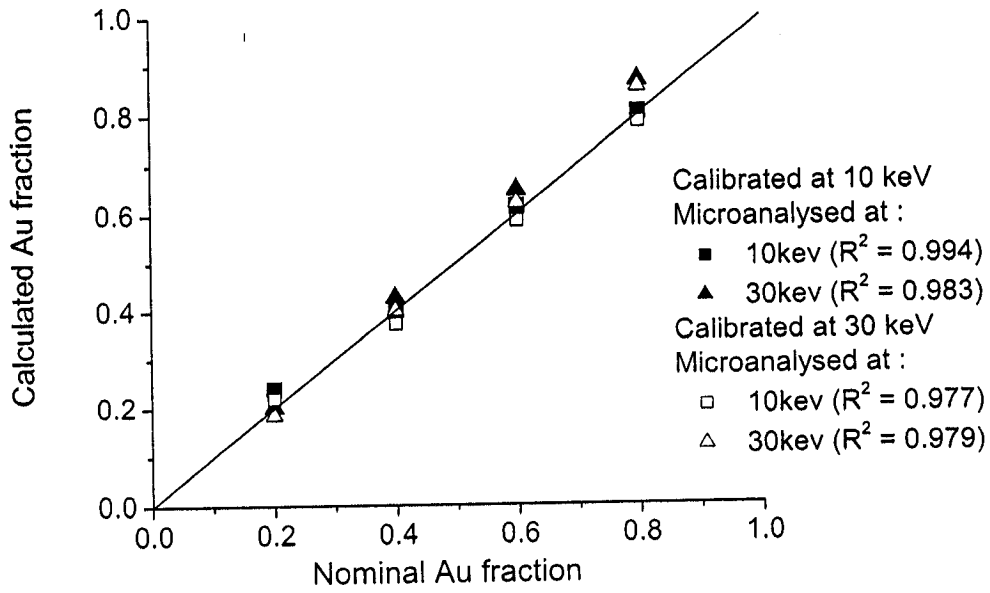

Figure 6–30: Comparison of the calculated ratio at 10 and 30 keV for the AuAg alloy

The accuracy is much improved with variable calibration factors. Results are excellent for the AuL-CuK pair with below 3 % of estimation error, below 10 % for the pairs AuL-CuL and AuM-CuK containing each at least one high energy characteristic peak and between 5 and 15 % for the AuM-CuL pair. Inaccuracy increases for lower energy characteristic lines, due to problems with the physical x-ray generation parameters, but also with the extraction of the characteristic peaks as explained in section 5.4. Absorption edges are important but not accounted for by the method of peak filtering used here. For the AuAg standards, the beam-energy-dependent calibration factor does not improve the accuracy as clearly, due to the scattering of the experimental x-ray intensities and ratios, that reduces the accuracy in the determination of the appropriate calibration factor.

For the AuL-CuL pair, the estimation error of Au weight fraction presents a minimum with beam energy as illustrated in figure 6–31. The relative error shows a minimum with the beam energy at 20 keV in correlation with the maximum shown by the calibration factor in figure 6–25. The dependencon on the beam energy is not monotonic in the case of the AuL-CuL ratio. The Au and Cu characteristic peaks of the two elements are from the same family, therefore some systematic inaccuracies of the model are expected to be cancelled out by the ratio of the ionization cross-sections, at least partially. Moreover, the composition effect in figure 6–31 reveals a possible problem with the mass-absorption coefficient and also underlines the possible need for peak deconvolution. On the other hand, when a beam-energy-dependent calibration factor is used, the composition effect is much less clear, and the relative estimation error is globally divided by two for the AuCu alloy.

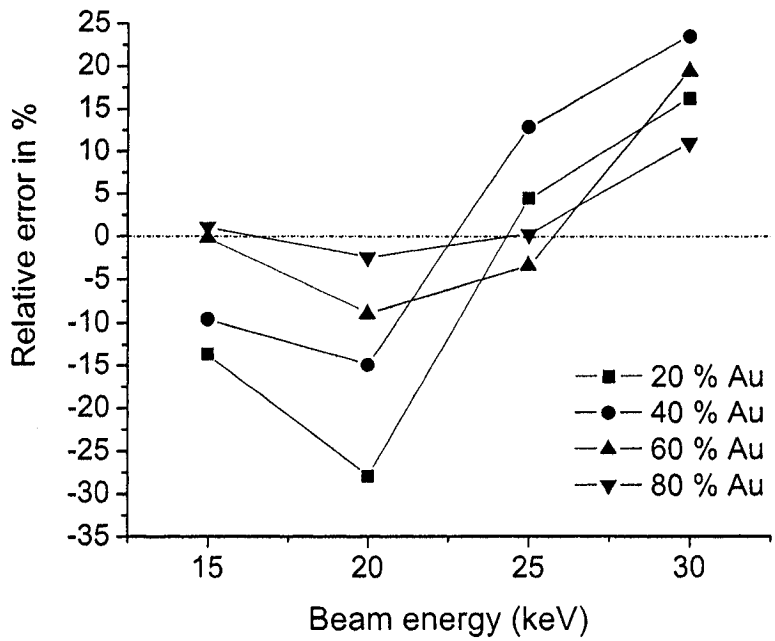

Figure 6–31: Relative error of estimated Au weight fraction for the AuL-CuL pair, with a constant calibration factor with regard to the beam energy

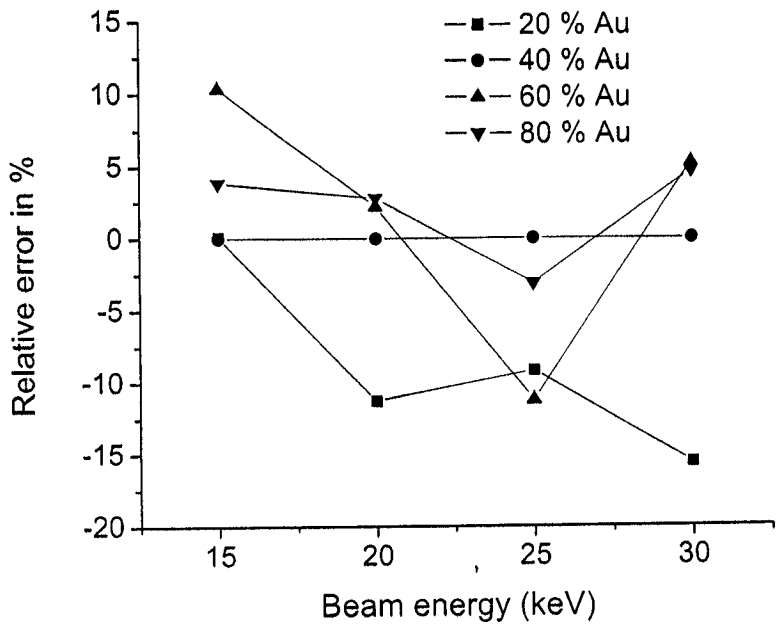

Figure 6–32: Relative error of estimated Au weight fraction for the AuL-CuL pair, with a beam-energy-dependent calibration

Figure 6–33 compares the relative error obtained with the Casnati and Salvat ionization cross-sections for the K-shell in the AuM-CuK pair. The error generated by the two models follows the same trend versus the beam energy and is very similar for the two models. The effect of the model chosen in regard to the beam energy is cancelled out by the calibration factor.

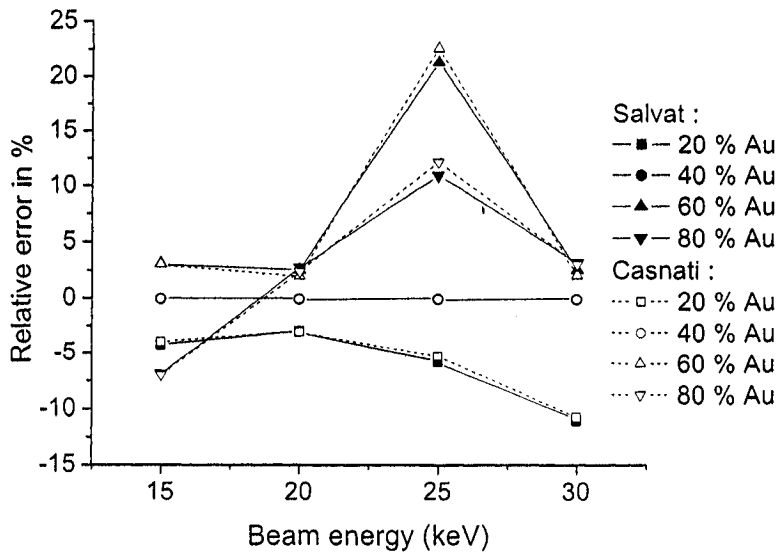

Figure 6–33: Relative error of estimated Au weight fraction for the AuM-CuK pair, with a beam-energy-dependent calibration and with the CuK Casnati [12] and Salvat [93] ionization cross-sections

Even with a beam-energy-dependent calibration factor, figure 6–34 reveals a strong dependence of the error on estimation of the Au weight fraction. The discrepancy between real and calculated Au weight fraction continuously increases from 15 to 30 keV. The AuMα and CuLα lines are low energy peaks, so are not very

well known. Moreover, the background discontinuities at low photon energy are not accounted for. Both of these factors can be the origin of these discrepancies. The correction of the ratio with a beam-energy-dependent calibration factor is not sufficient in the case of large inaccuracies in the models of x-ray generation, as expected for low energy characteristic lines, such as AuMα and CuLα1.

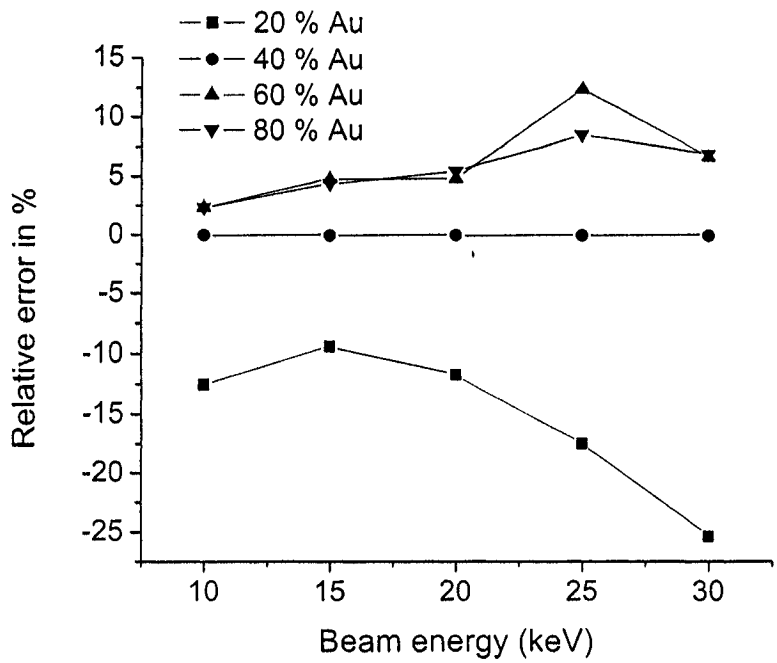

Figure 6–34: Relative error of estimated Au weight fraction for the AuM-CuL pair, with a beam-energy-dependent calibration

Furthermore, in the case of the AuAg alloys, figure 6–35 shows the estimation error with regard to the beam energy for the AuL-AgL pair and with a beam-energy-dependent calibration factor. The relative error is mostly independent of the specimen composition except for the $Au_{20}Au_{80}$ at 15 and 20 keV. Thus this calibration factor provides an accuracy independent of the specimen weight fraction.

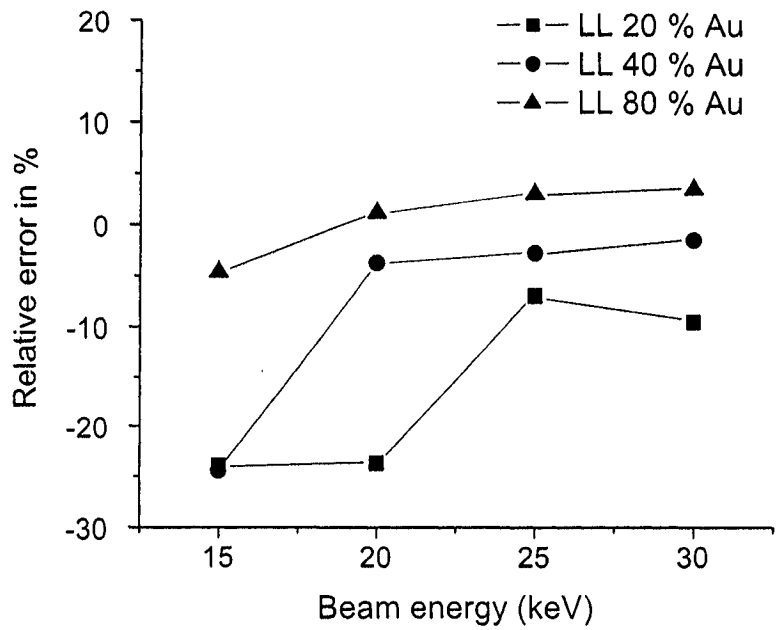

Figure 6–35: Relative error of estimated Au weight fraction for the AuL-AgL pair, with a beam-energy-dependent calibration

Figure 6–36 displays the relative error of Au weight fraction for the AuM-AgL pair in the AuAg alloys with a constant calibration factor. For 60 and 80 % of Au, the error varies within 10 %. The calculation accuracy is also dependent on the composition and the beam energy and is also scattered from -20 to 10 %. From that

figure, it can be deduced that the calculations for the alloys with 20 % of Au causes large error in the composition calculations, probably due to experimental errors, either from the collection of photons or from the background subtraction filtering. The errors are more monotonously increasing for the 60 and 80 % of Au.

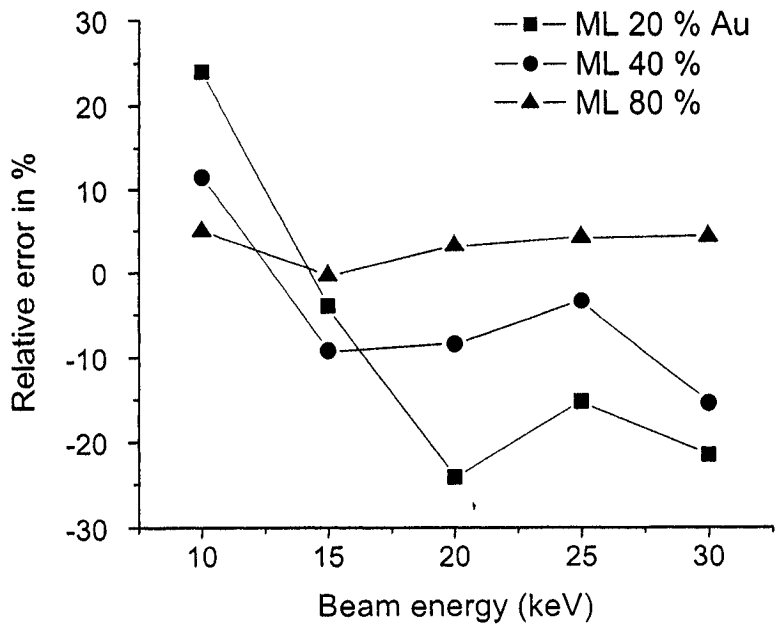

Figure 6–36: Relative error of estimated Au weight fraction for the AuM-AgL pair, with a beam-energy-dependent calibration

These last figures show that in most cases, the determination and the use of a beam-energy-dependent calibration factor largely improve the accuracy of quantification. However, in the case of low energy characteristic x-ray peaks, the gain in accuracy is reduced and the need for better physical models of x-ray generation arises.

6.3.2 Effect of the calibration factor

The comparison of calculated and measured calibration factors for the $Au_{20}Cu_{80}$ and $Au_{80}Cu_{20}$ alloys in figure 6–37 confirms the increase in the values of the calibration factors with the beam energy. Variable calibration signifies that the beam-energy-dependent calibration factor defined in figure 6–24 is used. These ratios are drawn without calibration factor and with constant averaged and beam-energy-dependent calibration factors calculated using the $Au_{40}Cu_{60}$ standard. As shown in figure 6–24, the corrected ratio is quite insensitive to concentration, since the calibration factor is only weakly dependent on the Au weight fraction. As shown in figure 4–2, the Au LIII ionization cross-section lies within the scattered measured values. This confirms the trend of the calibration factor below 1 with the AuL line.

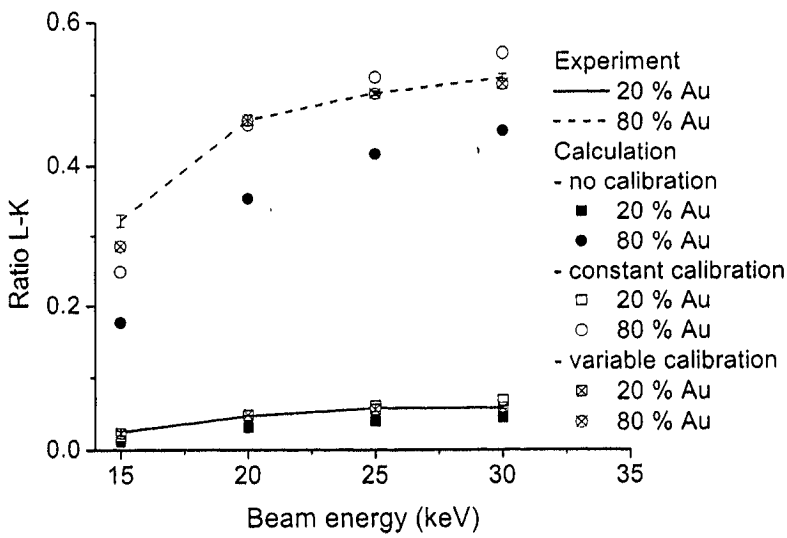

Figure 6–37: Comparison of experimental and simulated ratios for the AuL-CuK pair

The use of a beam-energy-dependent calibration factor improves the correlation between the calculated and measured calibrated ratios. The need for a beam-energy-dependent calibration is confirmed in the following figures. In figure 6–38, ratios for 40 and 60 % of Au do not follow the general trends at 25 keV. Variable calibration means that the beam-energy-dependent calibration factor defined in figure 6–26 is used. The composition effect is more important for the AuM-CuL than for the AuM-CuK pair, as shown in the calibration factors of figure 6–26. Despite the wide variation in the calibration factors for the AuM-CuK pair with the beam energy, the results are surprisingly good; most relative errors of estimation range below 20 %.

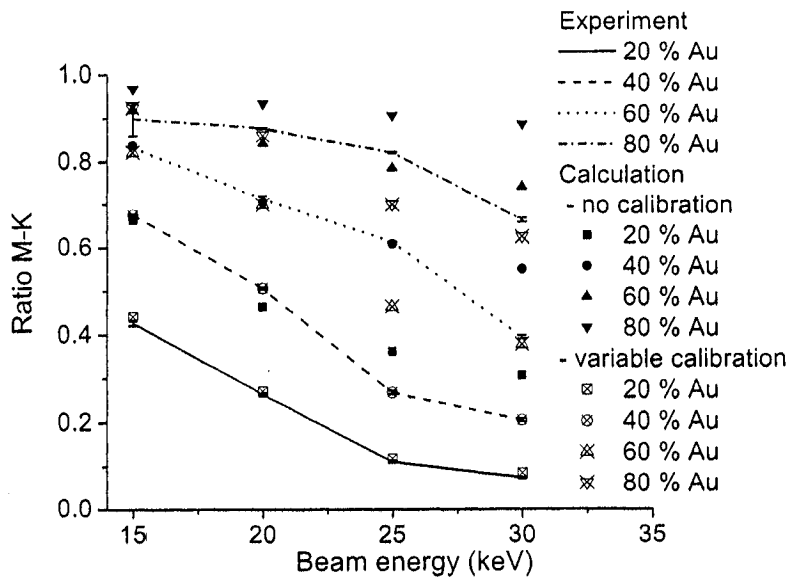

Figure 6–38: Comparison of experimental and simulated ratios for the AuM-CuK pair

The experimental curve for the AuM-CuL pair is similar to the AuL-CuK pair. This is shown in figure 6–39 which compares the experimental ratios and the theoretical ratios with and without calibration factors for the AuM-CuL pairs (variable calibration means with the beam-energy-dependent calibration factor defined in figure 6–27). The need for a calibration is confirmed by the observation of the discrepancy between the theory and the experimental values. The calibration factor is calculated at each beam energy, for the $Au_{40}Cu_{60}$ standard. The corrected ratio is sensitive to the specimen concentration. The error of the method should be higher than with the AuL-CuK ratio.

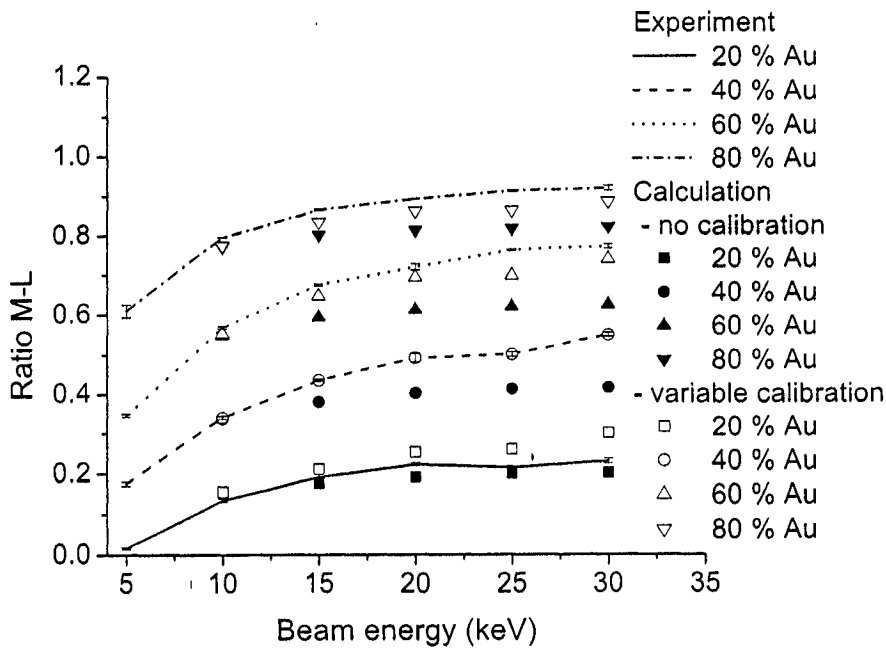

Figure 6–39: Comparison of experimental and simulated ratios for the AuM-CuL pair

The use of an average calibration factor allows minimization of the error due to experimental scattering. However, the effect of inaccuracies in the models, revealed in the composition and beam energy effect, is enhanced. The choice of the calibration factor is very important to optimize the accuracy of the method. However, this would also underline the difficulty of obtained an universal calibration factor, since it is dependent of the detector efficiency and the beam energy of the simulation, as well as the used pair of lines and the materials.

6.3.3 Effect of the ionization cross-section model

The ionization cross-section is the main parameter of x-ray emission. Both relative values with respect to the ionization cross-sections of other subshells and the dependence on the beam energy are essential in the calculation of x-ray generation. For instance, the calibration factor for the AuM-CuK pair of lines is greater than 1. From equation 3.22, this means either the AuM line intensity is overestimated or the CuK line intensity is underestimated, as confirmed by figure 4–1 with the Salvat ionization cross-section compared to experimental measurements. M-shell ionization cross-sections are not available for verification. However, increase of x-ray intensity may also be due to fluorescence. As noticed by Heinrich et al. [43], fluorescence due to the continuum (which is not simulated in this work) is significant for the intensity of CuKα and AuLα emission. Finally, the CuKα line is enhanced by fluorescence due to the AuLα line. Therefore the true CuKα intensity is surely larger than the theoretical calculations due to fluorescence. This trend is confirmed by the value of the calibration factor. In order to evaluate the effect of the ionization cross-section model on the x-ray generated intensity, figure 6–40 depicts CuK generated $\varphi(\rho z)$

curves with Salvat and Casnati ionization cross-sections for the $Au_{20}Cu_{80}$ standard. The film used in the $\varphi(\rho z)$ calculation is a pure Cu film. With the Casnati cross-section, the $\varphi(\rho z)$ is overestimated in comparison with the Salvat ionization cross-section. The difference of x-ray intensity is due to the difference of absolute value and shape of ionization cross-section in regard to the beam energy, as shown in figure 4–1.

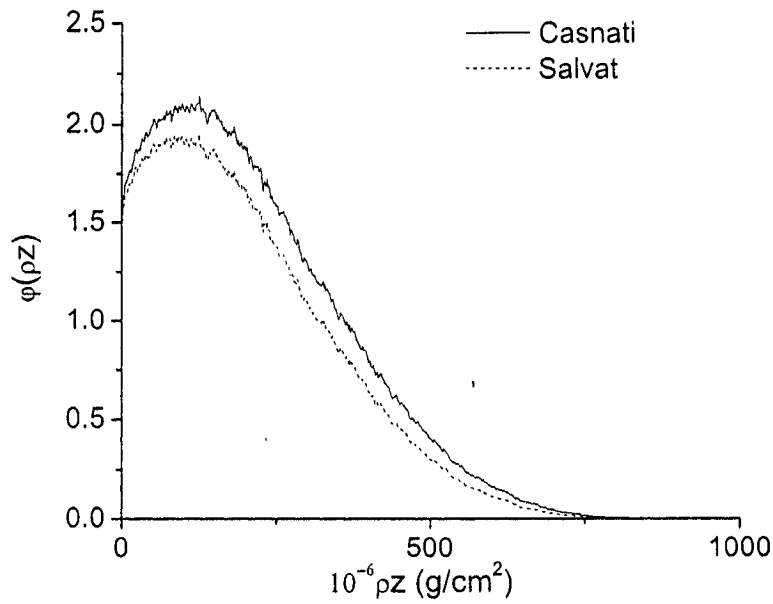

Figure 6–40: Cu $K\alpha 1$ $\varphi(\rho z)$ curve with the Casnati [12] and Salvat [93] ionization cross-sections for the $Au_{20}Cu_{80}$ standard at 20 keV

The comparison of the Au weight fraction estimation error with respect to the model of ionization cross-section is drawn in figure 6–41 for the AuL-CuK pair. The trends are similar, with a decrease at 15 keV and an increase at 30 keV. The intermediate beam energies are localized between the curves for 15 and 30 keV.

Salvat's ionization cross-section produces a relative error systematically smaller than the one produced by Casnati ionization cross-section for K-shell. In both cases, the L-shell ionization cross-section is calculated by Salvat method, therefore the use of Casnati model for the K-shell may enhance the difference between the two models and then produce larger difference.

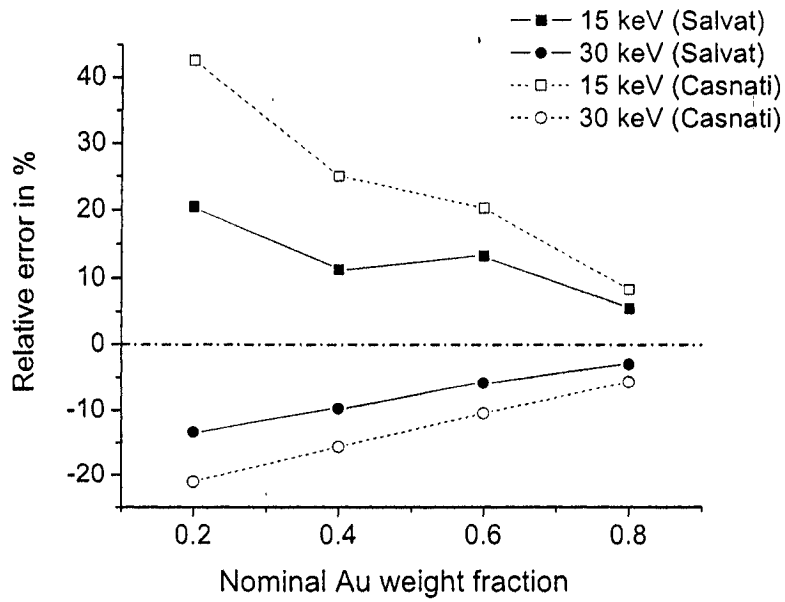

Figure 6–41: Relative error in estimated Au weight fraction for the AuL-CuK pair, with a constant calibration, using Casnati [12] and Salvat [93] Cu K-shell ionization cross-sections

The trends of figure 6–41 are confirmed in figure 6–42 which represents the same result but for the AuM-CuK pair of lines. Both curves converge to 0 % of error at 30 keV.

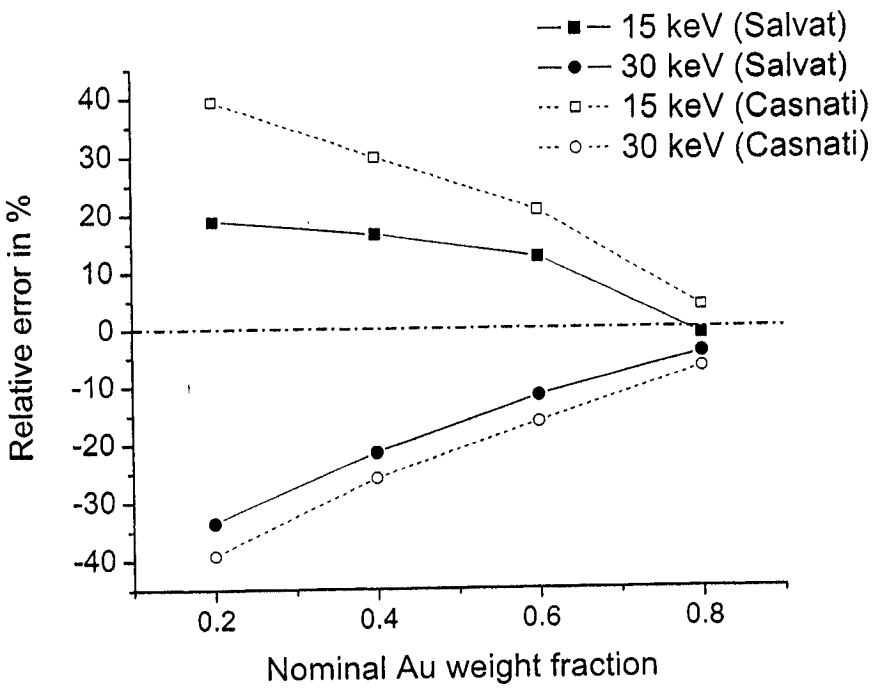

Figure 6–42: Relative error in estimated Au weight fraction for the AuM-CuK pair, with a constant calibration, using Casnati [12] and Salvat [93] Cu K-shell ionization cross-sections

Calculation produces very similar accuracy for the AuL-CuK pair results (figure 6–43) with beam-energy-dependent calibration factors and the two ionization cross-section models. The composition effect is almost identical in the two curves, meaning that it is now weakly related to the uncertainty of ionization cross-section models.

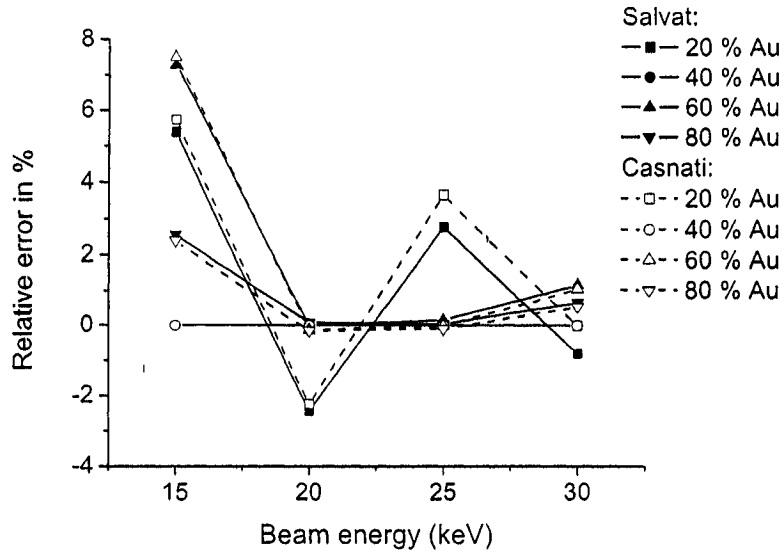

Figure 6–43: Relative error in estimated Au weight fraction for the AuL-CuK pair, with beam-energy-dependent calibration, with Casnati [12] and Salvat [93] Cu K-shell ionization cross-section

In table 6–2, the accuracy is clearly better with the Salvat ionization cross-section for the K-shell than with the Casnati model. The comparison between the different pairs of lines emphasizes the interest of using higher energy lines, such as the AuL-CuK pairs, which are better known and therefore give a better knowledge of

the x-ray generation parameters. The accuracies for the AuL-CuL, AuM-CuK and AuM-CuL pairs are very similar.

6.3.4 Effect of the fluorescence correction

Fluorescence due to the continuum affects the higher energy lines, such as AuL and CuK, while characteristic fluorescence may change the x-ray intensity of the CuK line [43]. The dependency of the calibration to the composition and the beam energy may also be caused by the fluorescence due to the characteristic x-ray for the CuKα line by the AuLα line and due to the contiunuum for the high energy lines CuKα and AuLα. A factor of correction for the fluorescence has been calculated as shown in section 4.4. The table 6–29 presents the caracteristic fluorescence correction δ in % of the characteristic x-ray intensity of the CuKα line, calculated as shown in equation 4.23, using the total emitted calculated x-ray intensity.

Table 6–29: Characteristic fluorescence correction for the CuK line

	15 keV	30 keV
20 % Au	0.66 %	2.04 %
40 % Au	1.51 %	4.54 %
60 % Au	2.62 %	7.75 %
80 % Au	4.16 %	12.05 %

The fluorescence due to the contiuum was also calculated as shown in table 6–30. From table 6–29, the characteristic fluorescence may have a consequent effect

Table 6–30: Continuum fluorescence correction

	AuL		CuK	
	15 keV	30 keV	15 keV	30 keV
20 % Au	5.34 %	3.67 %	0.40 %	3.05 %
40 % Au	7.04 %	4.91 %	0.58 %	4.45%
60 % Au	8.84 %	6.28%	0.82 %	6.41 %
80 % Au	10.77 %	7.80 %	1.18 %	9.38 %

at high beam energy, for high concentration of Au. Continuum fluorescence also

has composition effect and decreases with the beam energy. Figures 6–44 and 6–45 compare the calculated ratios for the AuL-CuK and AuM-CuK pairs of lines, with and without the effect of fluorescence (characteristic and bremsstrahlung) included.

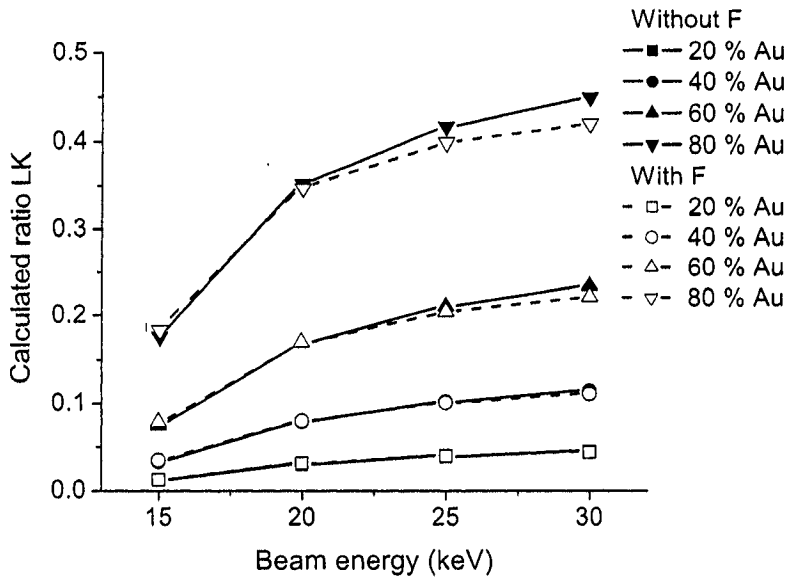

Figure 6–44: Comparison of the ratio of the AuL-CuK pair with and without the fluorescence effect F

New calibration factors were recalculated using the fluorescence correction as:

$$f_{fluo} = \frac{1}{1 + \frac{1-f}{f} F} \tag{6.11}$$

where F is the fluorescence correction for the pairs of lines, as explained in table 6–31.

Corrected calibration factors are shown in figure 6–46 for the AuL-CuK pair, in figure 6–47 for the AuL-CuL pair, in figure 6–48 for the AuL-AgL pair and in

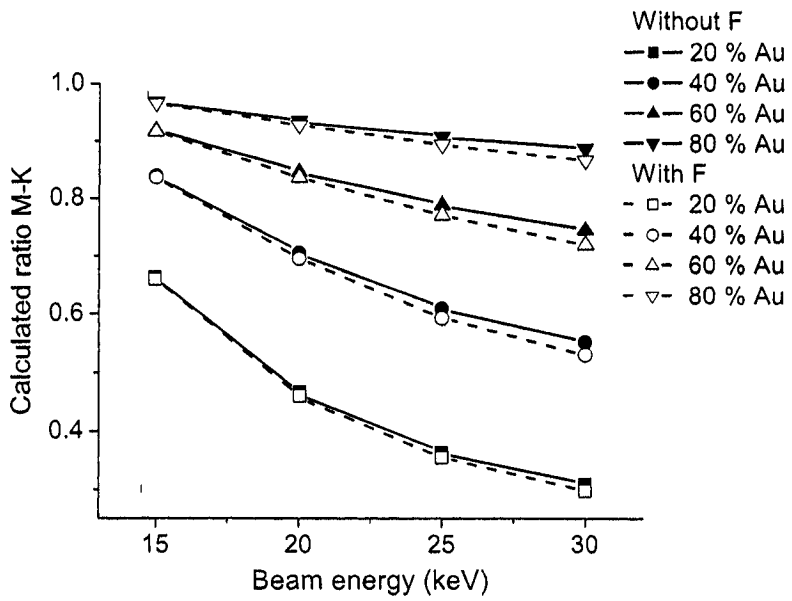

Figure 6–45: Comparison of the ratio of the AuM-CuK pair with and without the fluorescence effect F

Table 6–31: Fluorescence correction for ratios (C= characteristic, B = bremsstrahlung)

	Fluorescence factor F
AuL-CuK	$(1+\delta^B_{CuK}+\delta^C_{CuK})/(1+\delta^B_{AuL})$
AuM-CuK	$1+\delta^B_{CuK}+\delta^C_{CuK}$
AuL-CuL	$1/(1+\delta^C_{AuL})$
AuL-AgL	$1/(1+\delta^C_{AuL})$

figure 6–49 for the AuM-CuK pair of lines. For the AuL-CuK pair, the fluorescence effect slightly increases the composition dependency of the the calibration factor. For the other pairs of lines, the effect does not seems to be significant except for the AuL-AgL pair of lines.

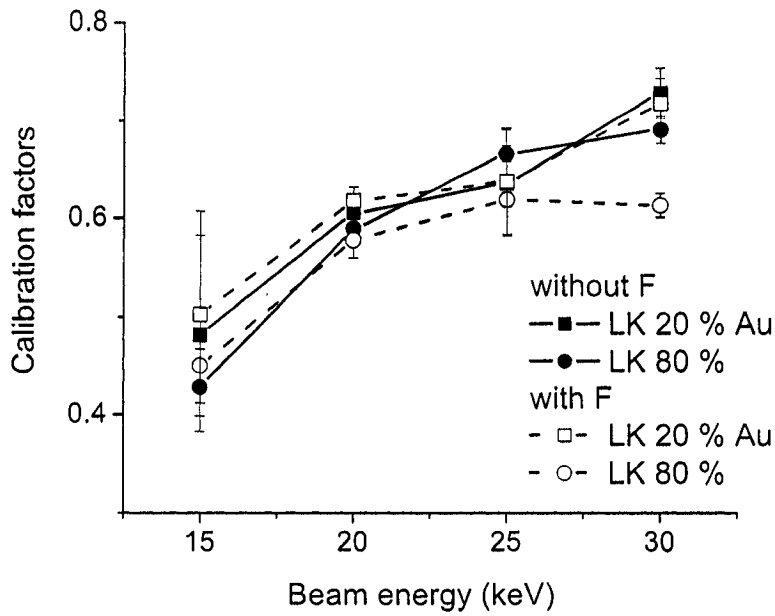

Figure 6–46: Comparison of the calibration factor for the AuL-CuK pair with and without fluorescence correction F

Then, Au weight fractions were recalculated with the new calibration factor and calculated ratios. Figure 6–50 shows the results using the AuL-CuK pair of lines and a constant calibration factor as explained above. The effect of fluorescence does not change significantly the accuracy, while this figure is compared with figure 6–7. A beam-energy-dependent calibration factor is still needed to improve accuracy, as

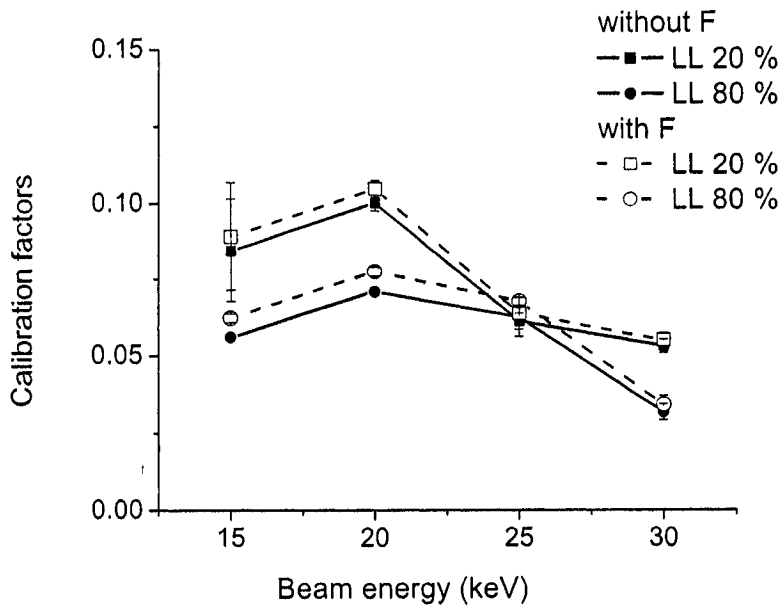

Figure 6–47: Comparison of the calibration factor for the AuL-CuL pair with and without fluorescence correction F

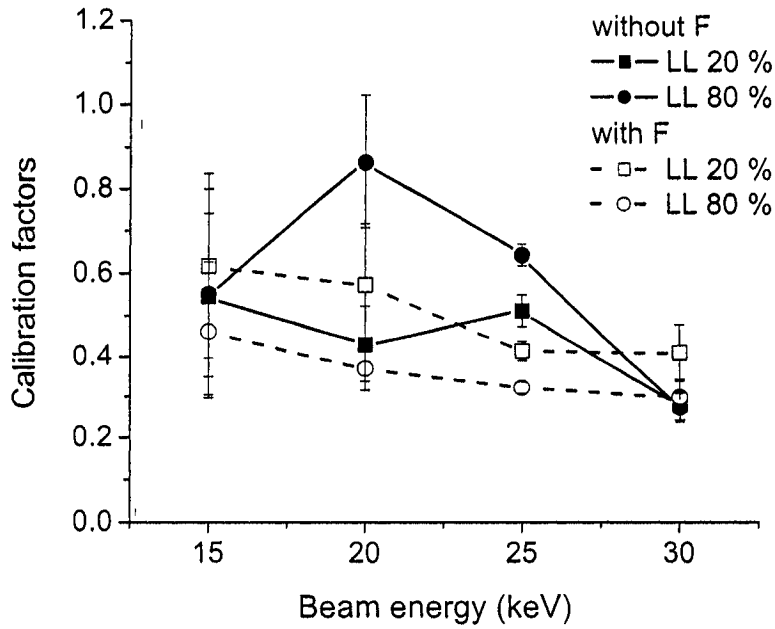

Figure 6–48: Comparison of the calibration factor for the AuL-AgL pair with and without fluorescence correction F

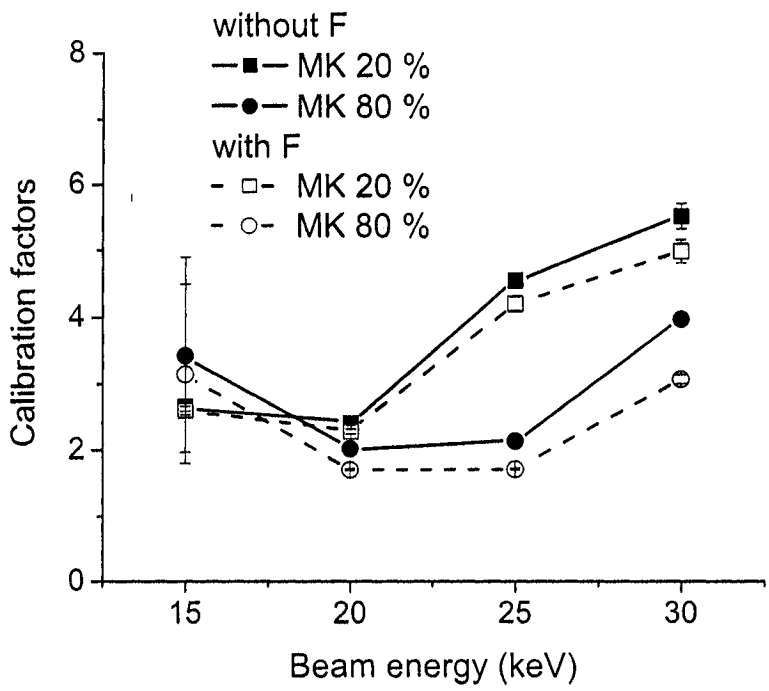

Figure 6–49: Comparison of the calibration factor for the AuM-CuK pair with and without fluorescence correction F

shown in figure 6–51. The error on the determinatio of Au weight fraction is not consistently changed.

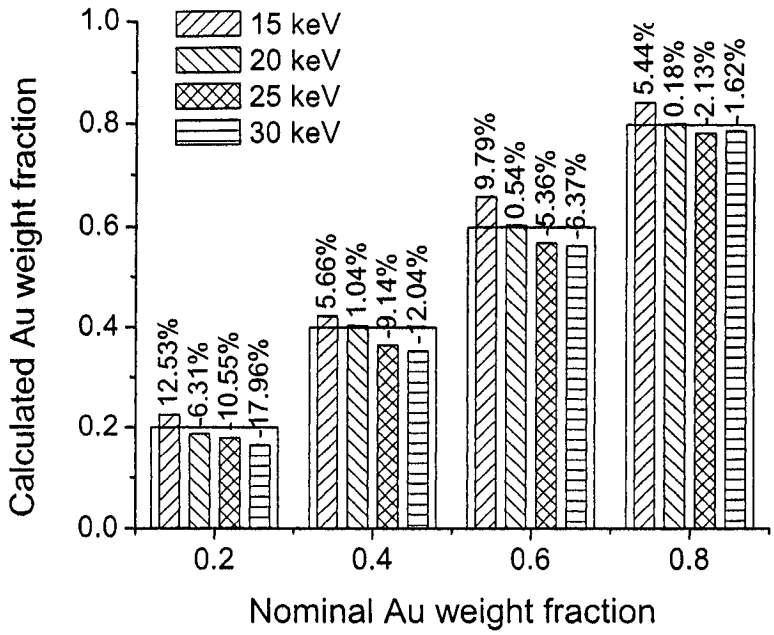

Figure 6–50: Calculated Au weight fraction using the AuL-CuK pair of lines, the constant calibration factor and including the fluorescence effect

Figure 6–52 compares the relative error of calculated Au weight fraction, with and without fluorescence effect. Any improvement can not be clearly observed from this figure, showing that the fluorescence is probably not the main cause of error in the calculations althoug it slightly improves accuracy.

Finally, figures 6–53, 6–54 and 6–55 compares the relative error of calculated Au weight fraction, for the AuCu alloy with and without the approximated fluorescence effect and using a beam-energy-dependent calibration factor. The most important

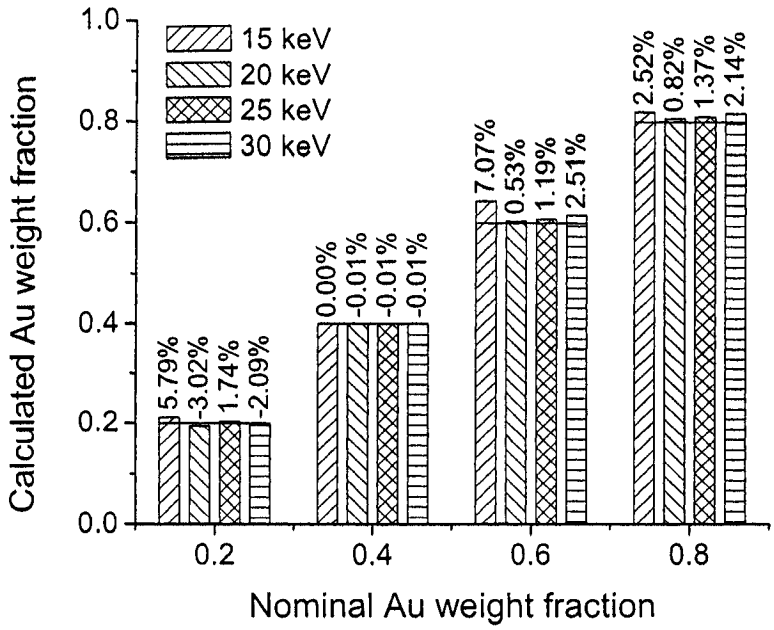

Figure 6–51: Calculated Au weight fraction using the AuL-CuK pair of lines, the beam-energy-dependent calibration factor and including the fluorescence effect

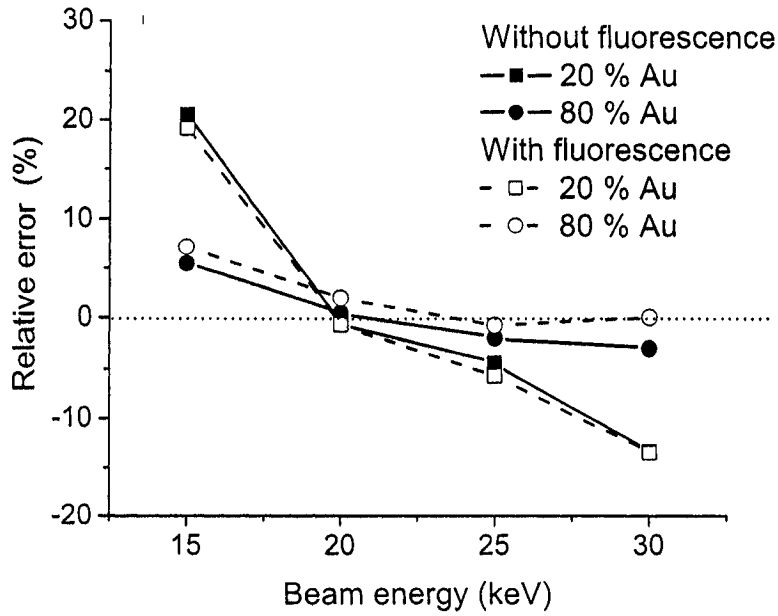

Figure 6–52: Comparison of error of calculation of the Au weight fraction using the AuL-CuK pair with and without the fluorescence effect and using an average calibration factor

effect is for the AuL-CuK and AuL-CuI pair, which may mean that the continuum fluorescence of the AuL line may consequently change the values of the calculated ratios. However, it must be reminded that the models used here are only approximation, and that fluorescence generated other lines that AuLα1 are neglected, as well as continuum fluorescence for other lines than AuLα1 and CuKα1 is not accounted.

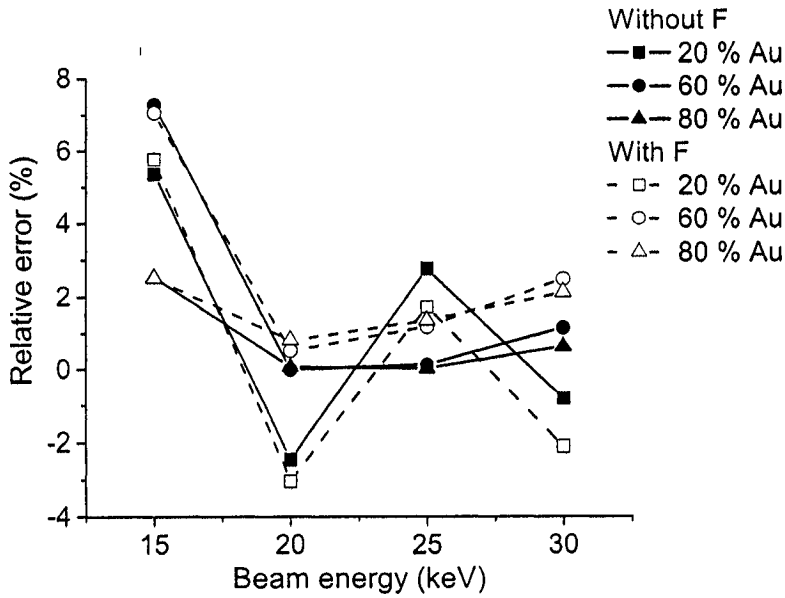

Figure 6–53: Relative error of estimation of the Au weight fraction using the AuL-CuK pair of lines and a beam-energy-dependent calibration factor and including the fluorescence effect

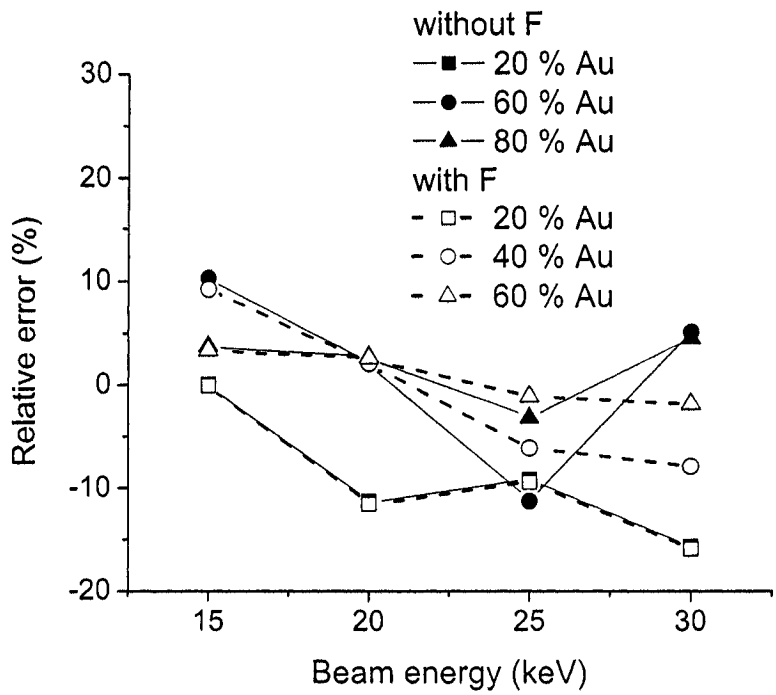

Figure 6–54: Relative error of estimation of the Au weight fraction using the AuL-CuL pair of lines and a beam-energy-dependent calibration factor and including the fluorescence effect

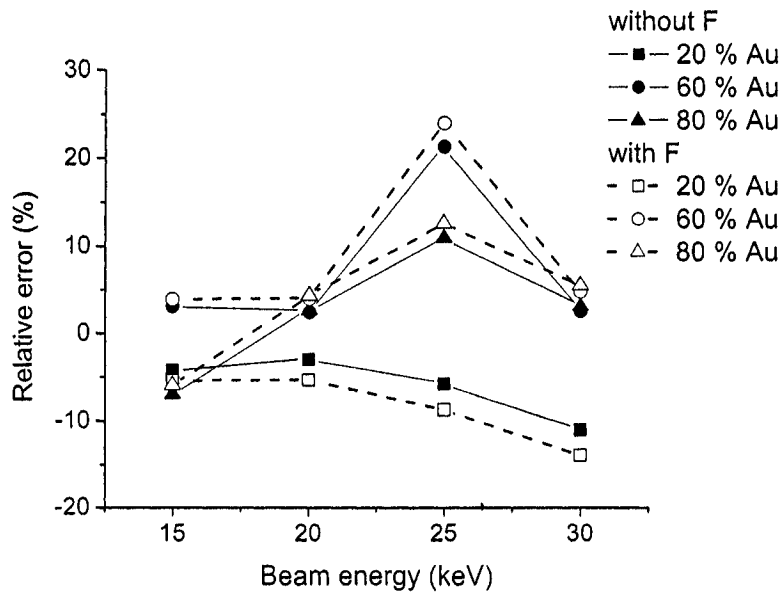

Figure 6-55: Relative error of estimation of the Au weight fraction using the AuM-CuK pair of lines and a beam-energy-dependent calibration factor and including the fluorescence effect

6.3.5 Effect of the choice of the characteristic peaks

For the AuL-CuL pair, the calibration factor is related to lines of the same type. Therefore the cancellation of systematic uncertainties in x-ray ionization cross-sections is expected in ratio 3.2 and this may reduce the beam energy and composition dependency. The curve for the AuL-AgL pair (figure 6–28) shows a relatively constant calibration factor with respect to the beam energy, and both the AuL-CuL pair in figure 6–25 and the AuL-AgL pair show a weak composition dependency. However, the complexity of the overlapped lines for the CuL peak (seven overlapped lines) probably reduces the advantage of cancellation.

The relative error of estimation of the Au weight fraction is drawn in figure 6–56 for the AuM-CuL pair. The low energies of AuM and CuL peaks (2.12 keV for AuM and 0.93 keV for CuL) permit the analysis of the application of this method to low energy characteristic x-ray lines. The error continuously increases with the beam energy. The composition effect is low at 10 keV and rises with the beam energy. Once again, this can indicate a problem with mass-absorption coefficient, as well as generation of x-ray physical models and peak extraction method.

On the other hand, the estimation error for the AuL-CuK pair is poorly dependent on the composition as shown in figure 6–57, emphasizing the importance of working with higher energy peaks, which are better known and less overlapped.

Two examples of graphs of the variation of the ratio with the beam energy and the Au weight fraction are drawn in figures 6–58 and 6–59. The error bars are the standard deviation of the four experimental measurements for each case. While the AuL-CuK ratio is clearly energy dependent, the AuM-AgL ratio is almost constant.

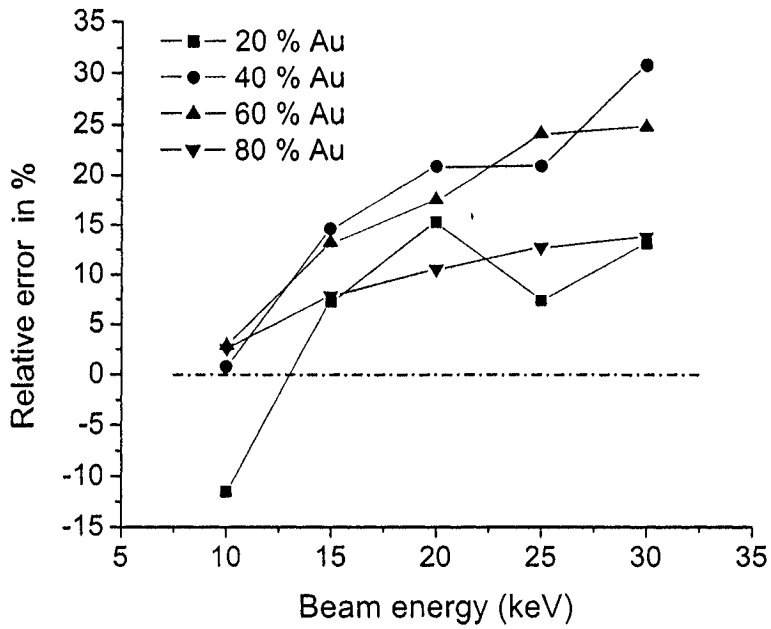

Figure 6–56: Relative error in estimated Au weight fraction for the AuM-CuL pair with a constant calibration

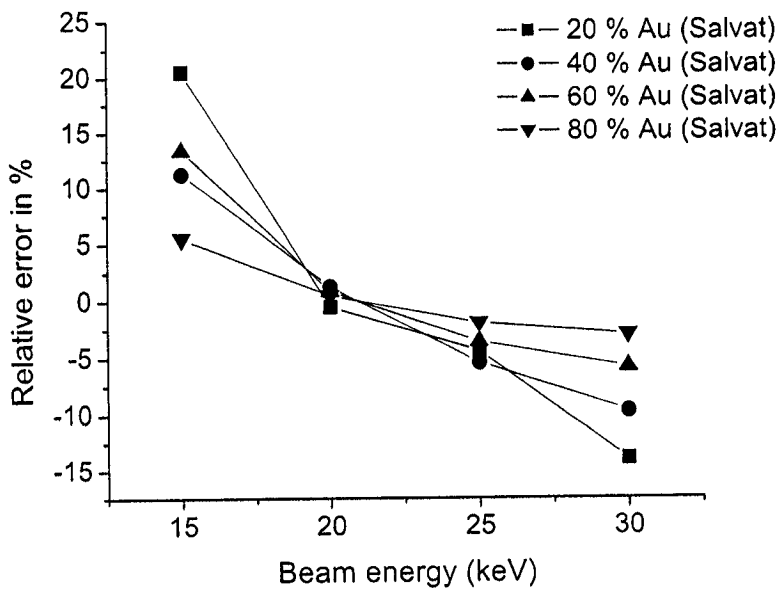

Figure 6–57: Relative error in estimated Au weight fraction for the AuL-CuK pair, with a constant calibration

In the case of AuL-CuK, the error bars are quite small, because the background shape is linear at these energies and characteristic peaks of high energy are easier to extract. The large error bars for the AuM-AgL pair demonstrate a problem either with the extraction of peak intensities or with the experimental measurements. As explained before, lower energy peaks introduce extraction errors, therefore the use of a simulated background, which includes mass-absorption edge jumps, would improve accuracy for such x-ray characteristic peaks. Moreover, the large error bars increase the errors in the estimation of the composition. The weak dependency of the ratio with the beam energy permits the conclusion that a constant calibration factor should offer similar accuracies than using a beam-energy dependent calibration factor, which is demonstrated in tables 6–3 and 6–6.

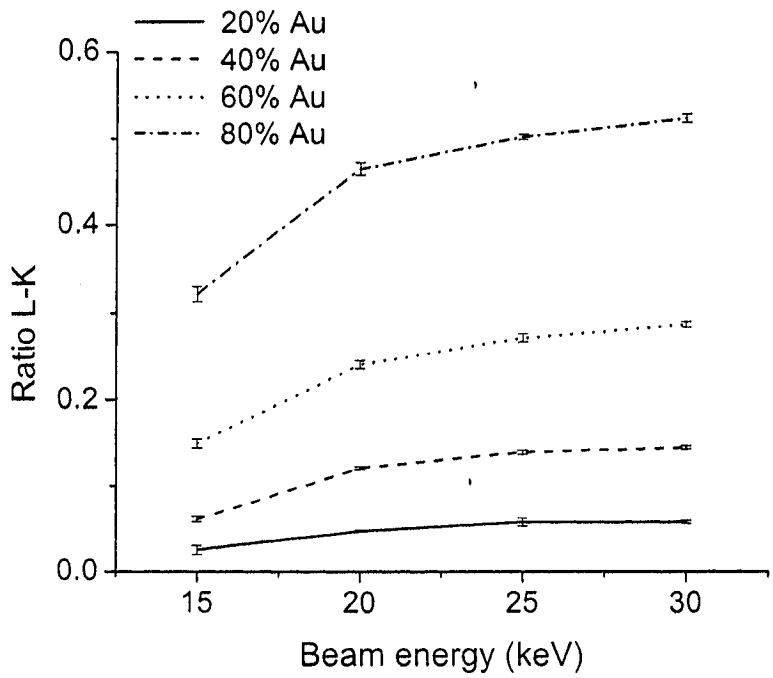

Figure 6–58: Variation of the experimental ratio for the AuCu alloys using the AuL-CuK pair

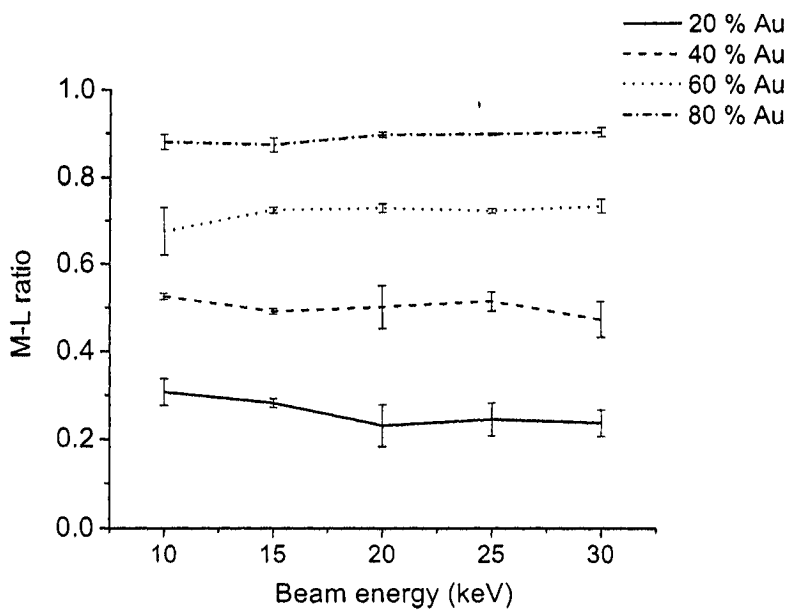

Figure 6–59: Variation of the experimental ratio for the AuAg alloys using the AuM-AgL pair

6.3.6 Effect of the mass-absorption coefficient

The effect of composition on the determination of the calibration factors is probably partially due to inaccuracies in the mass-absorption coefficients. In order to evaluate the effect of possible inaccuracy of mass-absorption coefficient on the composition effect, Monte Carlo calculations were launched with weighted mass-absorption coefficients. For instance for an element A, the new mass-absorption coefficient χ_w is:

$$\chi_w = P \cdot \chi \tag{6.12}$$

where P is the weighting factor and χ the mass-absorption coefficient from the Henke database [47]. Figure 6–60 shows the effect of 50 and 150 % of weighting for either Cu or Au mass-absorption coefficient. The effect is very low for the AuL-CuK pair (figure 6–60) for both weighted Au and Cu absorption coefficients, because the absorption effect is always weaker for high energy x-rays. The effect is similar for Au and Cu. For 20 % of Au, the mass-absorption coefficient is 216.58 cm^2/g for AuLα and 177.92 cm^2/g for CuKα, from table 4–4.

On the other hand, the ratio AuM-CuL is more strongly modified by the same change in the absorption coefficient as shown in figures 6–61 and 6–62 respectively for the Cu and Au weighted mass-absorption coefficients. From table 4–4, for 20 % of Au, $\chi_{AuM\alpha} = 1793\ cm^2/g$ while it is 2420.4 cm^2/g for Cu$L\alpha$. Therefore the absorption effect is more important for these characteristic lines as underlined by Heinrich et al. [43], shown in figure 4–11 and confirmed in figures 6–61 and 6–62. At 10 keV for the Cu weighted absorption, the ratio increases by 4% when the weight P goes from 50 to 150 %. From interpolation with ratio curves under these conditions, this causes

a relative variation by 2 % in the calculated Au weight fraction. In figure 6–62, the ratio increases by 2 % when the mass-absorption coefficient is weighted from 50 to 150 % at 15 keV for 80 % of Au. The effect of weighting depends on the element involved and its mass-absorption coefficient, as well as its concentration; it is reduced when the beam energy is decreased in figure 6–61, while it increases in figure 6–62.

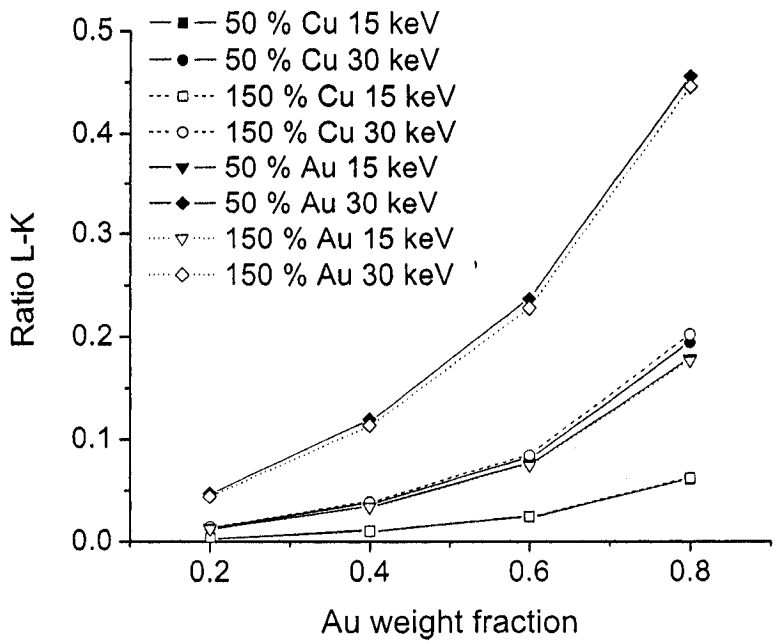

Figure 6–60: Effect of weighting the mass-absorption coefficient of Cu for the AuL-CuK pair

In order to understand the previous figures, another point to analyze is the variation of the mass-absorption coefficient of each x-ray characteristic line in the

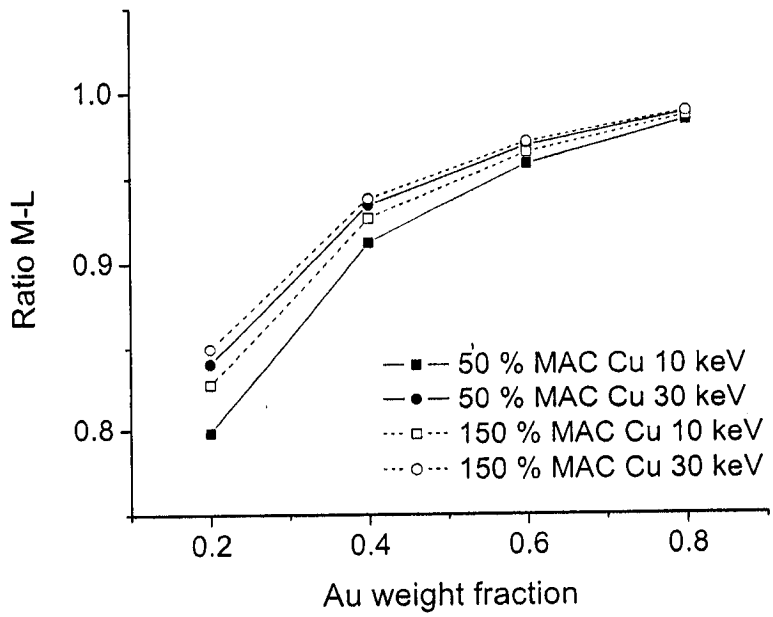

Figure 6–61: Effect of weighting the mass-absorption coefficient of Cu for the AuM-CuL pair

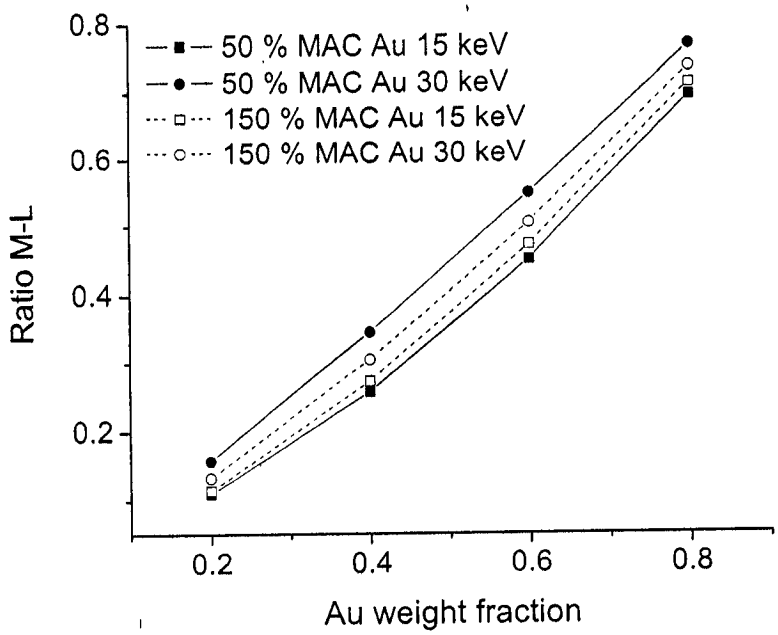

Figure 6–62: Effect of weighting the mass-absorption coefficient of Au and for the AuM-CuL pair

material, according its composition, as defined in equation 2.9 and as shown in figure 6–63. The coefficients for AuMα and AuLα decrease with increased Au weight fraction. For CuKα, the absorption coefficient decreases with Au weight fraction, while for CuLα it decreases. This means that absorption is important for low concentrations of Au for the AuMα, AuLα and CuKα lines, although it is more important for the CuLα lines at high Au concentration. Mass-absorption coefficient inaccuracy

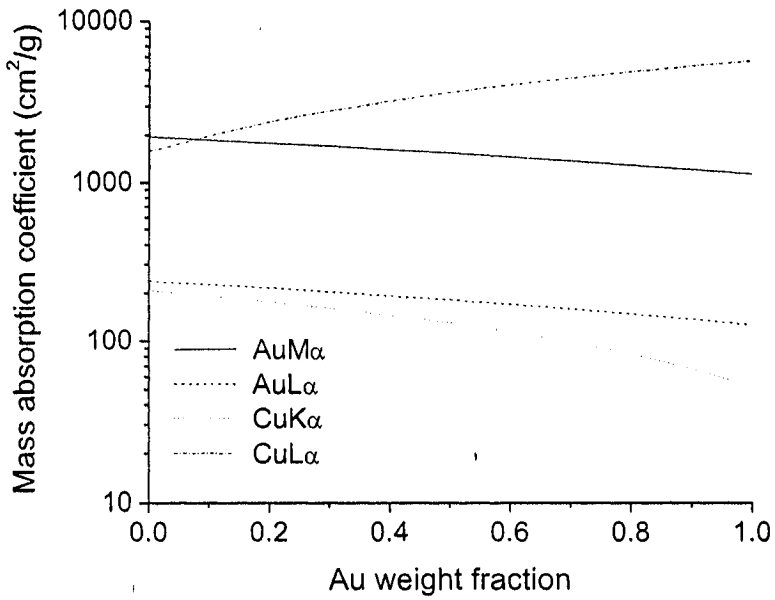

Figure 6–63: Mass-absorption coefficient of the main Au and Cu characteristic x-ray lines in Au_xCu_{1-x} alloy

is more significant with low energy x-ray intensity (Cu Lα and Au Mα), at low beam energy and with low concentration elements. However, this effect is probably not the only cause of the composition dependence of the calibration factors. However,

in order to confirm this hypothesis, measured values of mass-absorption coefficient should be compared to the theoretical values, in order to estimate the diference. The composition effect on the calibration factor could be due to the correlated effect of inaccurate mass-absorption coefficient and fluorescence effect.

6.3.7 Effect of the x-ray generation calculation method

Finally, in order to verify if the global behavior of the ratios, Monte Carlo curves of ratios versus composition were compared with the curves obtained by the PAP model (see section 5.2), for the AuCu standard alloys. The results can be seen in figures 6–64, 6–65, 6–66 and 6–67. The L-K ratio shows very good agreement between the two models, from 15 to 30 keV, while the discrepancy increases with beam energy for the L-L, M-K and M-L ratio pairs. For these three pairs of lines, the ratio curves are quite close at 15 keV but the difference increases with the beam energy. This is linked to inaccuracies in physical parameters particularly the $\varphi(\rho z)$ curve shape, as compared in section 5.2. Moreover, since the $\varphi(\rho z)$ curves present a different shape, different ratios are expected.

The differences in the x-ray generation models are compensated by calibration factors, since the accuracy is similar for both models as shown in tables 6–4 and 6–5. Figure 6–68 compares the error of estimation of Au weight fraction for the AuL-CuK pair. Monte Carlo simulations generally offer a better accuracy, as also observed in the tables of results 6–4 and 6–5.

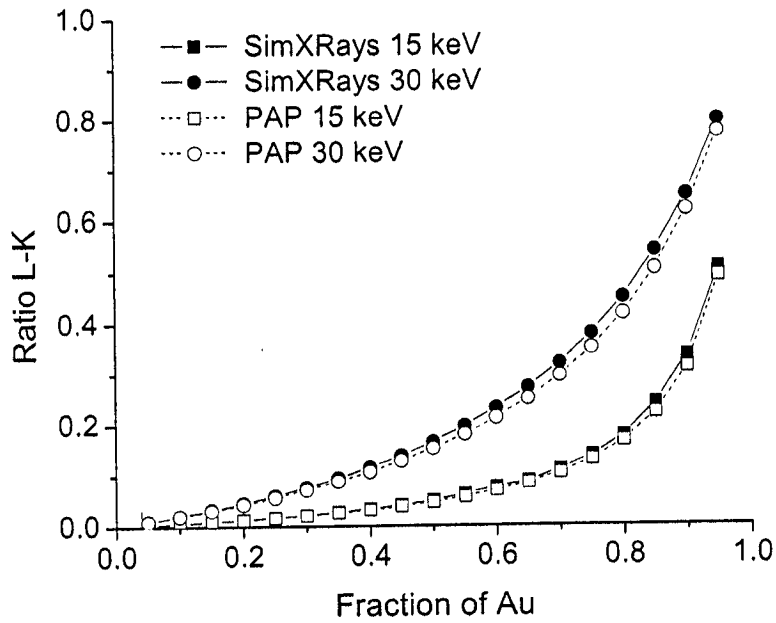

Figure 6–64: Comparison of ratios calculated with the PAP model [77] and Monte Carlo simulation program, for the AuL-CuK pair

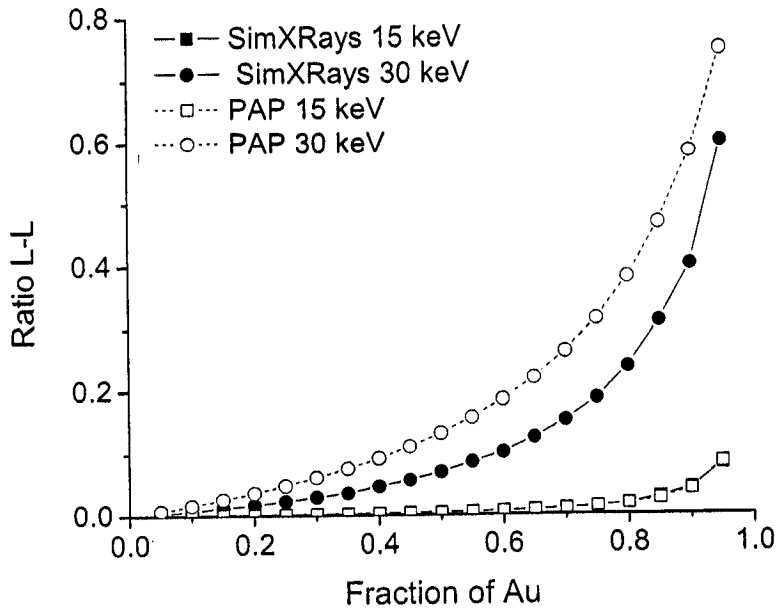

Figure 6–65: Comparison of ratios calculated with the PAP model [77] and Monte Carlo simulation program, for the AuL-CuL pair

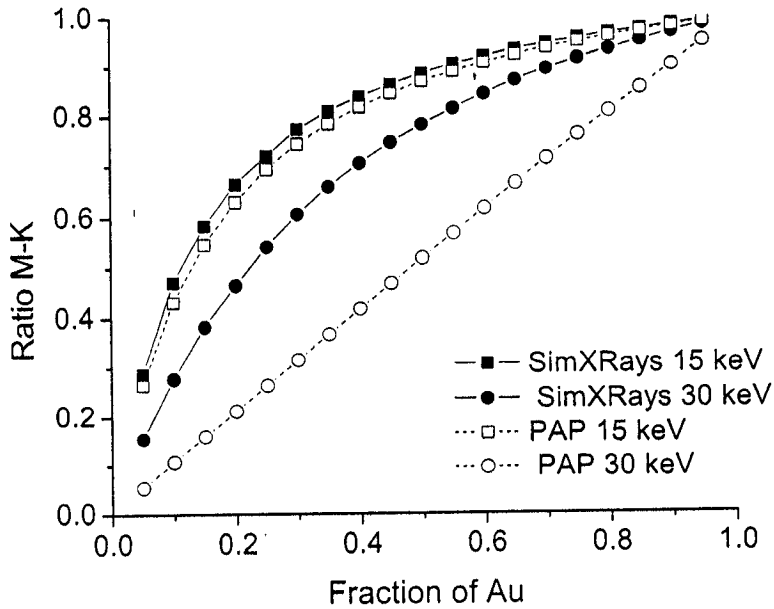

Figure 6–66: Comparison of ratios calculated with the PAP model [77] and Monte Carlo simulation program, for the AuM-CuK pair

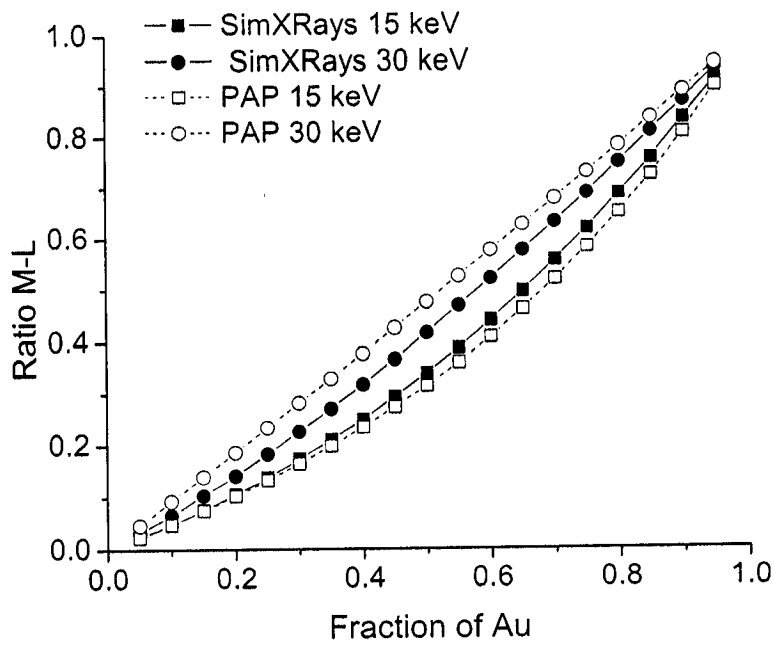

Figure 6–67: Comparison of ratios calculated with the PAP model [77] and Monte Carlo simulation program, for the AuM-CuL pair

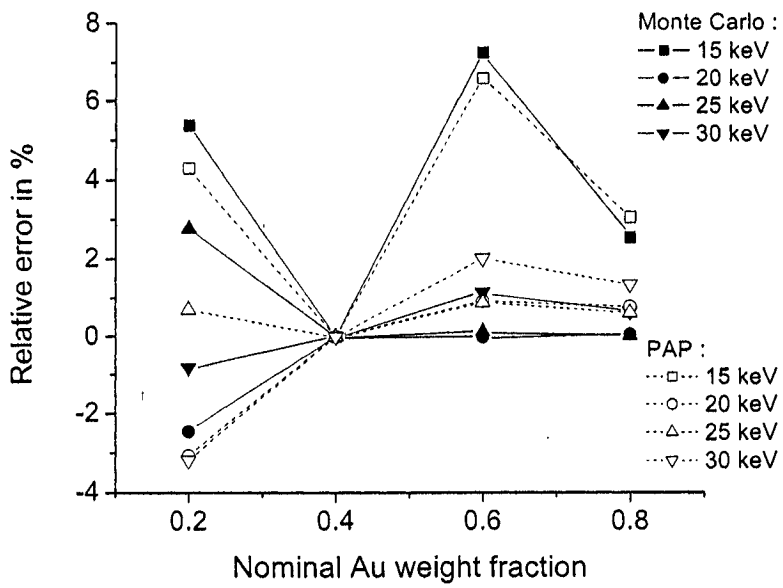

Figure 6–68: Comparison of the relative errors of estimation of Au weight fraction calculated with Monte Carlo and PAP model [77] for the AuL-CuK pair

6.3.8 Effect of the error propagation

Since the quantification process is based on the use of calibration factors, which are determined from experimental measurements of x-ray intensities, the examination of the propagation of errors through this method is necessary. A typical curve of calibration factor versus the ratio is shown in figure 6–69, for the ratio $f(\Lambda) = AuM\alpha/(CuL\alpha + \Lambda AuM\alpha)$ for the AuCu alloys at 5 keV. The intensities were calculated with Monte Carlo simulations. The calibration factor Λ varies between 0 and 3 and the curves are the reciprocal of f(Λ).

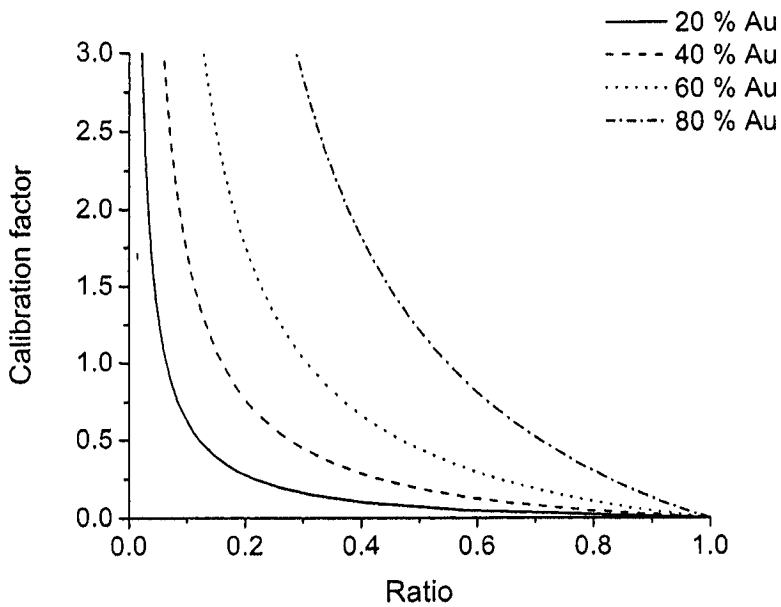

Figure 6–69: Theoretical variation of the calibration factor Λ with the ratio $AuM\alpha/(CuL\alpha + \Lambda AuM\alpha)$ as a function of Λ, calculated with the Monte Carlo program at 5 keV

This curve enhances the effect of variation of the ratio (due to experimental errors for instance) on the calibration factor. In the case of calibration, the statistics, measurement or processing errors induce errors in the calculation of the ratios, and furthermore in the determination of calibration factors. Figure 6–70 presents an example of error propagation, extracted from the $Au_{60}Cu_{40}$ curve in figure 6–69. The step $\Delta x = 0.1$ is the same for the two examples. In the region of lowest slope, it causes a variation of 0.09 on the y axis, while it is 0.74 in the upper region of highest slope. This shows the negative or positive effect that the calibration introduces in the processing of the spectrum, depending on the beam energy of the microanalysis as well as on the specimen composition. Reciprocally, inaccuracy in the values of the calibration factor affects the accuracy of the calculated and calibrated ratios, and further affects the calculated weight fraction.

The value of the calibration factor may significantly alter the accuracy of the method if not chosen cautiously. Hence the range of variation of the calibration factor due to experimental error affects the later range of calculated ratios and therefore the scattering of calculated weight fractions. In order to evaluate this effect, tables 6–32 and 6–33 show the error of estimation of the ratio due to the statistical error of x-ray emission (according to equation 3.11) for the $Au_{20}Cu_{80}$ and the $Au_{80}Cu_{20}$ alloys respectively and from the intensities shown in figure 3–2.

The statistical error propagated to the ratio is quite small, around three orders of magnitude smaller than the ratio itself. It is not the main source of error in the estimation of the ratio. However, it shows the effect of concentration and type of lines.

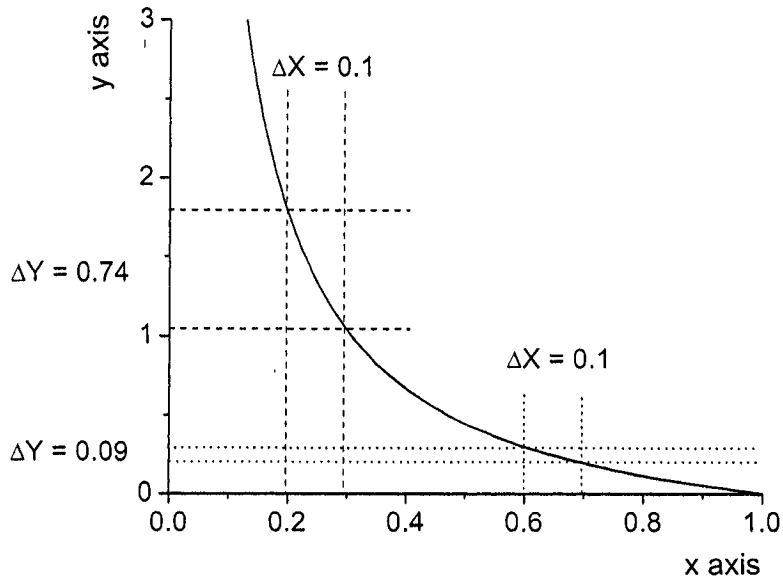

Figure 6–70: Example of error propagation from the ratio to the calibration factor

Table 6–32: Absolute statistical error propagated to the ratio for the $Au_{20}Cu_{80}$ standard

Beam energy	L-L ratio	M-K ratio
15 keV	0.0083± 1.19E-04	0.4300± 7.88E-06
20 keV	0.0378± 7.90E-05	0.2649± 1.72E-05
25 keV	0.1128± 1.61E-04	0.1084± 5.02E-05
30 keV	0.1885± 1.76E-04	0.0721± 5.85E-05

Table 6–33: Absolute statistical error propagated to the ratio for the $Au_{80}Cu_{20}$ standard

Beam energy	L-L ratio	M-K ratio
15 keV	0.1764± 2.02E-04	0.9362± 3.01E-05
20 keV	0.4990± 4.36E-07	0.8774± 2.19E-05
25 keV	0.7024± 8.29E-05	0.8218± 2.04E-05
30 keV	0.8594± 2.53E-04	0.6724± 2.63E-05

6.3.9 Effect of the spectrum filtering method

The principle of peak filtering is explained in section 5.4. Here some points of this technique are enhanced, particularly the limits for low energy characteristic peaks. For low energy peaks, such as AuMα, CuLα, the peaks are more narrow than AuLα, CuKα, since the full width at half maximum E_{FWHM} is dependent on the photon energy as explained by Reimer [86]:

$$E_{FWHM} = \sqrt{\Delta E + 2.6232 \cdot 10^{-3} E} \tag{6.13}$$

where ΔE is the square of the electronic noise due the amplification process and the term $2.6232 \cdot 10^{-3} E$ represents the statistical probability of creating an electron-hole pair by a photon of energy E in keV (see appendix A for the description of the working principle of the energy dispersive detector). Thus, when E increases, E_{FWHM} increases. According to Benoit [5], the filtering method is less accurate when the peaks are wider and lower. The required filter needs larger central lobes because of the peak width, but then is less sensitive to the rapid change in the background shape which occurs at the absorption edges. Low emitted intensity is due to a combined effect of overvoltage and high mass-absorption coefficient. This is the case for low energy photons and low concentration elements, such as AuMα in the $Au_{20}Cu_{80}$ alloy as shown in figure 6–71.

Extraction of peak intensity can be improved by using a simulated background shape, especially for low energy photons as explained by Statham [106]. However, the current models for bremsstrahlung generation are not accurate enough to allow this (section 5.3).

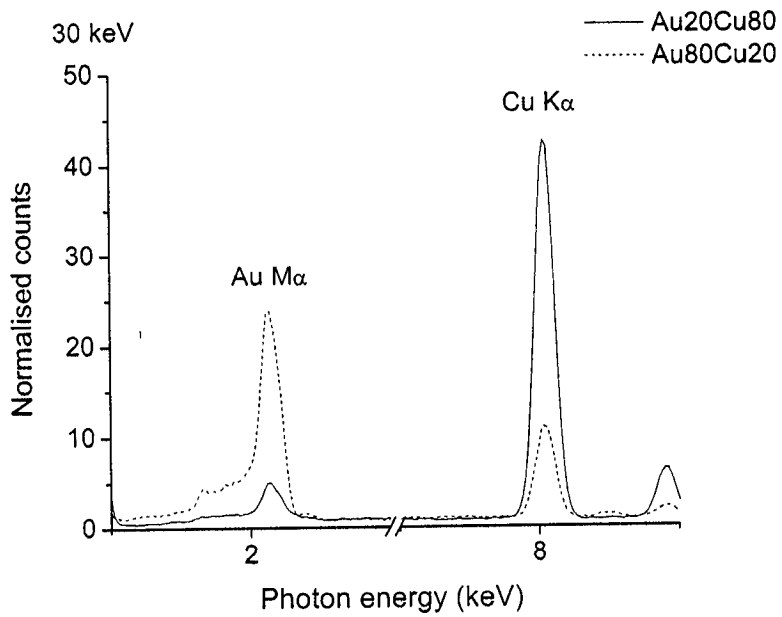

Figure 6–71: Spectra of the $Au_{20}Cu_{80}$ and $Au_{80}Cu_{20}$ alloys at 30 keV

6.4 Analysis of results and discussion

Most of the results presented here underline the dependence of the method on the electron beam energy. In the curves of calibration factors shown in section 6.2.4, the electron beam energy dependency is clear. Using a constant calibration factor, the average error of estimation of the Au weight fraction is below 10 % for the AuCu alloy using the AuL-CuK pair of lines, and below 12 % for the AuAg alloy using the AuL-AgL pair of lines. This enhances the fact that the theoretical x-ray generation parameters do not fit with reality, and particularly versus the electron beam energy. This also means that the ideal calibration factor should be determined in relation to the microanalysis beam energy as explained in section 6.3.1 in order to get better results, with average estimation error for Au weight fraction below 10 % except for 20 % of Au weight fraction (table 6–4). Moreover, the choice of characteristic lines is also important, as discussed in section 6.3.5. For instance, the AuL-CuK pair provides a much higher accuracy (around 3 % on average) in Au weight fraction determination than the AuL-CuM pair (around 7 % error on average) as shown in tables 6–2 and 6–4.

Moreover, the use of M and L lines to calculate the ratio adds to the complexity of determining the exact emitted x-ray intensity. The choice of keeping the convoluted peaks to quantify the materials has been done. Figure 6–4 shows that the effect of convolution on the ratio is major for the AuL-CuK pair while it is almost negligible for the AuM-CuL and AuM-CuK pairs. Despite the fact that this work was done without deconvolution (see section 6.1), the best results were provided for the pair AuL-CuK for the AuCu standard with both a constant and a variable calibration

factor. Therefore the effect of convolution is expected to be minor in the case of the other pairs of lines, although deconvolution should improve accuracy for low energy peaks, due to absorption effect.

Despite the complexity of the x-ray spectra, which added difficulties in the experimental data processing and modeling, the accuracy of the estimation of composition is more than satisfying in many cases, better than 3 % for the AuL-CuK pair in AuCu, and better than 12 % for the AuL-AgL pair in AuAg. For the AuM-AgL pair, it appears that the measured x-ray ratios present a large standard deviation due to the scattering of measured x-ray intensities. This consistently alters the accuracy. The experimental scattering of x-ray intensities can be due either to temporary problem with the measurement of low energy peaks or their extraction processing. Some experimental values vary largely from less than 50 % up to 200 % of the average of these values, as explained in section 6.2.2. If the values below 50 % and above 200 % are taken apart, the mean relative error of estimation of the Au weight fraction falls around 7 % for the AuAg alloys using the AuL-AgL pair, while it was 16 % with all the experimental values. However, except for two conditions ($Au_{20}Ag_{80}$ alloy at 10 and 15 keV, where the peaks are the lowest), none to one data was taken out of four.

The use of beam-energy-dependent calibration factor does not clearly improve the accuracy for the AuM-AgL pair, due to the large scattering of measured ratios, as shown in figure 6–29. For the AuL-AgL pair, if the results at 15 and 20 keV for 20 % of Au weight fraction are taken out (corresponding to the smallest x-ray intensities), the mean error of estimation of the Au weight fraction ranges below 3 %, which is close to the accuracy obtained for the AuCu alloys using the AuL-CuK

pair. The fact that low energy characteristic lines are always used for the AuAg alloys also explains the lower accuracy than the one obtained with high energy lines for the AuCu alloys.

For the specific case of the specimens used here, the calculation of bremsstrahlung and characteristic fluorescences slightly reduce the beam-energy dependency of the calibration factor for the AuL-CuL and AuL-AgL, but seem to increase its composition effect. This could be due to inaccuracy of the correction model for fuorescence. However, the effect is small in regards with the global accuracy of the method except for the AuL-CuK and AuL-CuL pairs of lines for high beam energy.

Another cause of inaccuracy comes from uncertainties due to the lack of reliable measurement of x-ray generation parameters for low energy L- and M-subshells, such as ionization cross-section (see section 4.1) but also mass-absorption coefficient. In section 6.3.6, figures 6–61 and 6–62 show enhancement of the impact of mass-absorption coefficient variation on the ratio for low energy peaks (AuM-CuL). The results of this study emphasize the need for more fundamental experimental databases, including ionization cross-sections, fractions of lines, fluorescence yields, Coster-Kronig parameters and also details about the detector efficiency.

Finally the comparison of accuracy obtained by Monte Carlo calculations and the PAP analytical model for $\varphi(\rho z)$ calculations enhances the versatility of the method which can be used with any reliable method of x-ray emission calculation. Monte Carlo simulations generally show a better accuracy, as compared in tables 6–4 and 6–5. However, the PAP model is much faster than Monte Carlo simulation and therefore

could be used for homogeneous materials where it is known to be reliable. The advantage of Monte Carlo is that is can be applied to any type of material, homogeneous, heterogeneous and even rough surfaces, interfaces, etc.

As shown in section 6.3.9 and also in the litterature [46], statistical and extraction errors are intrinsic to microanalysis, since they are directly related to the collection of photons and to the basic processing of spectra. In the case of this work moreover, these errors are propagated to the determination of the calibration factor, and furthermore to the calculation of the composition. At the time of microanalysis at 25 keV, instability of the energy dispersive spectrometer was discovered and a hole in the window of the energy dispersive spectrometer was later detected. This caused development of ice on the crystal and so increased the absorption of low energy x-rays, such as the CuLα characteristic line. Therefore, discrepancies in the experimental ratios for the low energy lines may be due to this effect. Reduction of statistical errors can be done by increasing the number of counts of peaks, which is limited by the physical parameters of x-ray generation and equipment characteristics. Extraction errors can be reduced by a different method of background subtraction, such as the use of a calculated bremsstrahlung [106]. The proposed method then reduces the propagation of error in comparison with the classical Cliff and Lorimer method (figure ??). It is also interesting to note that for the $Au_{80}Cu_{20}$ alloy at 25 keV, the microscope was just flashed and the beam current extremely unstable. Despite this fact, the calculated composition is close to the nominal composition of the specimen. This shows the independence of this method to the beam current fluctuations as well as its promising accuracy. Once the calibration factor is determined for

a material, or an element, it can be reused as often as needed, making it simple to make quantitative microanalysis at one beam energy, using a tabulated calibration factor.

Chapter 7
Conclusion

The quantitative x-ray microanalysis method proposed here offers a promising accuracy of weight fraction measurements for the studied AuCu and AuAg NBS (NIST) standards. The independence of the results with respect to the beam current has been demonstrated in this work. The method introduced here can provide fast and accurate quantification. Results obtained with the cold field emission gun scanning electron microscope S-4700 have shown that this method works for this type of electron microscope, although the beam current is known to be unstable. Therefore, in order to correct the uncertainties in the physical parameters, a calibration factor must be implemented in the ratio. Under optimum conditions of x-ray microanalysis and with appropriate calibration factors and characteristic lines, this approach permits the determination of the composition with a relative error better than 3% for the AuCu standard alloys (AuL-CuK pair) and better than 7 % for the AuAg alloys (AuL-AgL pair), both with a beam-energy-dependent calibration factor.

The study of the dependence on the accuracy of different variables such as the value of the mass-absorption coefficient and the ionization cross-section emphasizes the need for a better knowledge of these parameters and the importance of their uncertainties on the quality of the standardless quantitative x-ray microanalysis proposed in this work. The choice of the characteristic lines is also essential to the accuracy; the lines of higher energy provides the best accuracy. This can be linked

to the fact that the low energy lines, typically L- and M-shells, are not very well known, as well as the shape of the bremsstrahlung. Moreover, the use of an appropriate calibration factor compensates for most differences and can achieve acceptable accuracies. The need for more experimental and reliable measurements of the x-ray generation parameters, in order to reduce the variation of the calibration factors for low energy characteristic lines, is emphasized by this work. The dependency of the calibration factor on the specimen composition, as well as the beam energy and the detector efficiency would make it difficult to establish a universal standardless method. Only better parameters, that would allow to reduce the effect of calibration factors, would make this standardless method more general.

The analysis of the results focuses on the major parameters affecting the reliability. One of the most important is the effect of the electron beam energy. It is particularly apparent on the graphs which link the calibration factors to the beam energy. The use of a beam-energy-dependent calibration factor results in a reduction in estimation error of Au weight fraction by a factor of three for the AuL-CuK pair for instance. The calculation of fluorescence inside the function of generation of x-rays would problably still reduce inaccuracy of x-ray generation. The effect of the variation of mass-absorption coefficients on calculated composition emphasizes a possible problem with the database, which cannot be corrected by the calibration factor, because it depends on the material composition. The importance of the error caused by the background subtraction method was also underlined. The use of two different models for the generation of the ionization cross-sections leads to correlated

calibration factors and very similar results. The calculations also show that the accuracy is similar using the Pouchou and Pichoir analytical model or a Monte Carlo program to calculate the emitted x-ray intensity. Therefore, the method appears to be independent of the model of x-ray generation chosen, as well as the method of calculation of x-ray generation because the differences are compensated by the calibration factors. However, Monte Carlo simulations as well as Salvat ionization cross-sections offers a better accuracy.

Considering the improvement that could be made, two main directions are to be explored. The first one is an exhaustive validation of the method which should be applied to other types of materials such as semi-conductors, stoichiometric components and other metallic alloys. The second point is the use of a different method for background subtraction, particularly with respect to the low energy characteristic peaks. A calculated bremsstrahlung could be used to subtract the spectrum instead of a filter. Moreover, on the experimental side, deconvolution of characteristic peaks would also reduce the extraction error of low energy lines, as well as the effect of the calibration factor for these lines. Increasing the reliability of x-ray emission calculation would allow to reduce the need for calibration factors. The main objective would be to avoid its beam-energy and composition dependency in order to obtain a Z-dependent, constant with the beam energy and composition independent calibration factor, which would be easier to determine and use. However, the need to calculate it for each microscope would certainly remain, because of the intrinsic difficulty of determining the EDS efficiency.

Moreover, this method could be expanded to ternary systems and also to more complex materials with n elements. Instead of interpolating a 2-D curve, the user would interpolate on n-surface to extract the composition. The approach by iteration could also be studied. Inasmuch as the specimen can be simulated with a Monte Carlo program, variable geometry could be used, such as rough surfaces, thin films, particles on a substrate and multilayered structures.

This work has opened a promising avenue for quantitative x-ray microanalysis with any electron microscope, and particularly the field emission gun scanning electron microscope.

Chapter 8
Original contribution to knowledge

This work permitted the development of an alternative method to ZAF and usual standardless quantitative x-ray microanalysis. It showed that an accuracy close to the one obtained by quantification with standards can be obtained, without the measurement of the beam current. It therefore opens the way to a real standardless method, taking into account the characteristics of the microscope and x-ray detector as well as the uncertainties in the knowledge of x-ray emission physical parameters. It was demonstrated that quantitative x-ray microanalysis is possible using a cold field scanning electron microscope where the beam current is unstable.

This work also showed that the Cliff and Lorimer ratio can be successfully applied to bulk specimen in a scanning electron microscope with an energy dispersive spectrometer. The formulation of the ratio also permitted the reduction of the propagation of measurement errors in the accuracy of the quantification. An investigation of the importance of fundamentals parameters on quantitative x-ray microanalysis was undertaken and thus it was demonstrated that the accuracy of estimation of these parameters is mandatory to perform reliable standardless quantitative microanalysis.

The development of a complete database of x-ray generation parameters, including the transitions rates, the Coster-Kronig and the fluorescence yields, extracted from the literature, permitted the development of a Monte Carlo program

which simulates full spectrum, complete families of characteristic lines as well as the bremsstrahlung. This work would permit background subtraction by the use of a simulated background in order to improve accuracy of x-ray intensity measurement.

Appendix A
Calculation of the detector efficiency and solid angle

An interesting overwiew of the working principle of the energy dispersive spectrometer was made by Macdonald [63].The determination of detector efficiency is complex, but mostly because its physical parameters are unknown to the user. The main part of the detector is a thick silicon layer as shown in figure 2–6. The window protects the silicon crystal from cracking, because of the wide difference in vacuum between the crystal and the specimen chamber. The counting and identification of the photon is determined from the number of created electron-holes pairs. When an x-ray of a certain energy interacts with an atom of silicon, it transfers its energy to the Si K-shell. Then the atom relaxes and emits either an Auger electron or a K_α x-ray, or produces an electron-hole pair, according to a certain probability. The energy E_{pair} to emit an hole-electron pair is 3.8 eV, so the number of generated electron-hole pairs is proportional of the incident x-ray energy $h\nu_x$ as in the next equation:

$$n_{pairs} = \left[\frac{h\nu_x}{E_{pair}}\right] \tag{A.1}$$

where n_{pairs} is the number of electron-hole pairs related to the energy of the photon. Since this is a statistical phenomenon, the number n_{pairs} is not constant but varies around its exact theoretical value according to Poisson law and then produces Gaussian shaped peaks. The number of counts in the peak remains equal to the real height of the peak. Moreover, according to Poisson law, the higher the number of

the counts, the wider is the peak. That is why the width of the peak increases with photon energy.

In order to determine the detector efficiency, the exact composition and the thickness of the window should be known. However, manufacturers do not provide the necessary data. Therefore, experimental measurements found in the literature were taken as the basis for this work [62]. The author gives the fluctuation of the efficiency of the EDS detector with respect to the energy of the absorbed x-ray. The window geometry was approximated according to general knowledge from the manufacturer. The window is made with a polymer film (Carbon, Oxygen and Nitrogen), and also a thin Al layer. Estimated thickness are given in table A–1. The mass-absorption coefficients of x-rays in each material was taken from Thinh and Leroux [109].

Table A–1: Estimated detector window polymer film thickness and density [62]

Film	Thickness	Density (g/cm^3)
Polymer	300 nm	1.29
Al	40 nm	2.7
Si	3 mm	2.33

The absorption parameter F in each layer and for each component was calculated according to:

$$\begin{aligned} F_{Al} &= e^{-\left(\frac{\mu}{\rho}\right)_{Al}\rho_{Al}t_{Al}} \\ F_{p} &= e^{-f_O\left(\frac{\mu}{\rho}\right)_{O}\rho_O t_O} \cdot e^{-f_C\left(\frac{\mu}{\rho}\right)_{C}\rho_C t_C} \cdot e^{-f_N\left(\frac{\mu}{\rho}\right)_{N}\rho_N t_N} \\ F_{Si} &= e^{-\left(\frac{\mu}{\rho}\right)_{Si}\rho_{Si}t_{Si}} \end{aligned} \tag{A.2}$$

where f_O, $f_C$and f_N are the fractions of O, C and N in the polymer. Then, the detector ε efficiency was then calculated as follows:

$$\varepsilon = F_{Al}F_p(1 - F_{Si}) \tag{A.3}$$

In order to ascertain the fraction of O, N and C in the polymer, iterative calculations were carried out in order to fit the experimental curve of efficiency given by Lund [62] and the theoretical efficiency described in equation A.3. The best fit was obtained for the composition of polymer given in table A–2 and figure 3–4 presents the efficiency curve obtained with theses specifications.

Table A–2: Estimated polymer film composition

Element	Weight fraction
O	0.17
C	0.75
N	0.08

Another variable is the solid angle of detection [110, chapter 6]. However, since this value is cancelled in this method, this factor is not major in this work. The solid angle of detection is calculated from a rough estimated value from the crystal size :

$$\Omega = \frac{1}{2}4\pi(1 - \frac{D}{\sqrt{D^2 + d^2}}) \tag{A.4}$$

where D is the distance from the specimen surface to the crystal surface, along the take-off angle and d is the given crystal diameter.

Appendix B
Second and third pages of the certificates of the SRM 482 and SRM 481 NBS standards

PREPARATION AND PURITY: The standards were prepared by Cominco American, Inc. in the form of wires approximately 150 meters long. The end members of the series, as well as the starting materials for the alloys, were of the highest purity grade and precautions were taken to minimize contamination. Two of the alloy standards were heat-treated at NBS to improve microhomogeneity. The pure metal standards were examined by the residual resistivity ratio technique and the total of electrically active impurities in each was estimated to be about 0.001%. The gold-copper wires were examined spectrographically for metallic impurities; no significant impurities were found at detection limits ranging from 0.0001 to 0.010%.

LONGITUDINAL HOMOGENEITY: Variation in composition along the full length of each alloy wire was investigated by electron probe microanalysis for areas 25 μm diameter on cross sections at three positions along the wire including the two ends. The observed differences in composition for the positions, expressed as the range between the highest and lowest values for each alloy, were as follows:

Nominal Composition	Au80	Au60	Au40	Au20
Observed range*	0.3%	0.7%	0.9%	0.9%

Homogeneity along the wires was also tested by measurement of the residual resistivity ratio. These measurements indicated that the variation (macroscopic) of composition along all standard wires was less than 0.1% absolute. Further information on longitudinal homogeneity of the wires was obtained by determinations of Au at the extreme ends of the alloy wires by the Bureau of the Mint; the data also indicate that the extreme variation along the wires is less than 0.1% absolute.

TRANSVERSE AND MICRO HOMOGENEITY: Variation in composition within the above mentioned cross sections of the wires was investigated by electron probe microanalysis. For each cross section, measurements were made along two diagonals at right angles. On each diagonal, determinations were made at 25 points, 1 μm or less in diameter, starting and ending at approximately 25 μm from the edge. For each alloy, the element which could be determined with the better precision was used in the evaluation. The variation was calculated in terms of the standard deviation for an individual determination for each traverse. In the table below, the variation is presented as the range between the lowest and highest observed standard deviations for the six traverses performed on each alloy.

Nominal Composition	Element Determined	Range of Standard Deviations for Traverses*
Au80	Cu	0.09 – 0.24%
Au60	Cu	.16 – .27
Au40	Au	.13 – .23
Au20	Au	.13 – .20

Figure B–1: Second page of certificate of analysis for the AuCu standards, SRM 482 [104]

The homogeneity on a microscopic scale was further investigated by performing quantitative measurements in two arrays of 10 × 10 points (1 μm diameter) on each of the cross sections. The distance between adjacent points was 3.5 μm. This was repeated on several cross sections so that 6 arrays were obtained on each alloy. For the element which could be measured with better precision, the range is given between the lowest and highest observed standard deviation for an individual determination for the 6 arrays for each alloy.

Nominal Composition	Element Determined	Range of Standard Deviations for Arrays*
Au80	Cu	0.19 – 0.28%
Au60	Cu	.28 – .37
Au40	Au	.25 – .31
Au20	Au	.12 – .20

*The ranges indicated are close to the precision of the method and should be considered upper limits of estimates of inhomogeneity.

Extensive homogeneity studies were performed with the electron probe microanalyzer at NBS by M. A. Giles, D L. Vieth, R. L. Myklebust, C. E. Fiori, and K. F. J. Heinrich. Measurements of residual resistivity ratio were made at NBS, Boulder, Colorado, by R. L. Rutter and R. L. Powell. Heat treatment of the alloys at NBS was performed by G. E. Hicho and M. R. Meyerson. Spectrographic survey analyses were made at NBS by V. C. Stewart. Determinations of composition were made at Cominco American, Inc., Spokane, Washington, by T. A. Rice; at the U. S. Bureau of the Mint, Washington, D. C., by H. G. Hanson, Jr.; and at NBS by J. R. Baldwin and R. A. Durst.

Figure B–2: Third page of certificate of analysis for the AuCu standards, SRM 482 [104]

PREPARATION AND PURITY: The standards were prepared by Cominco American Inc. in the form of wires approximately 150 meters long. The end members of the series, as well as the starting materials for the alloys, were of the highest purity grade and precautions were taken to minimize contamination. Two of the alloy standards were heat-treated at NBS to improve microhomogeneity. The pure metal standards were examined by the residual resistivity ratio technique and the total of electrically active impurities in each was estimated to be about 0.001 percent. The gold-silver wires were examined spectrographically for metallic impurities; no significant impurities were found at detection limits ranging from 0.0001 to 0.010 percent.

LONGITUDINAL HOMOGENEITY: Variation in composition along the full length of each alloy wire was investigated by electron probe microanalysis for areas 25 μm diameter on cross sections at three to five positions along the wire including the two ends. The observed differences in composition for the positions, expressed as the range between the highest and lowest values for each alloy, were as follows:

Nominal Composition	Au80	Au60	Au40	Au20
Observed range	0.3%	0.6%	0.3%	0.5%

Homogeneity along the wires was also tested by measurement of the residual resistivity ratio. These measurements indicated that the variation (macroscopic) of composition along all standard wires was less than 0.1 percent absolute. Further information on longitudinal homogeneity of the wires was obtained by determinations of Au at the extreme ends of the alloy wires by the Bureau of the Mint; the data also indicate that the extreme variation along the wires is less than 0.1 percent absolute.

TRANSVERSE AND MICRO HOMOGENEITY: Variation in composition within the above mentioned cross sections of the wires was investigated by electron probe microanalysis. For each cross section, measurements were made along two diagonals at right angles. On each diagonal, determinations were made at 25 points, 1 μm or less in diameter, starting and ending at approximately 25 μm from the edge. For each alloy, the element which could be determined with the better precision was used in the evaluation. The variation was calculated in terms of the standard deviation for an individual determination for each traverse. In the table below, the variation is presented as the range between the lowest and highest observed standard deviations for the six to eight traverses performed on each alloy.

Nominal Composition	Element Determined	Range of Standard Deviation for Traverses[a]
Au80	Ag	0.08 – 0.11%
Au60	Au	.08 – .16
Au40	Au	.08 – .13
Au20	Au	.12 – .37

Figure B–3: Second page of certificate of analysis for the AuAg standards, SRM 481 [103]

The homogeneity on a microscopic scale was further investigated by performing quantitative measurements in two arrays of 10 × 10 points (1 μm diameter) on each of the cross sections. The distance between adjacent points was 3.5 μm. This was repeated on several cross sections so that 6 to 8 arrays were obtained on each alloy. For the element which could be measured with better precision, the range is given between the lowest and highest observed standard deviation for an individual determination for the 6 to 8 arrays for each alloy.

Nominal Composition	Element Evaluated	Range of Standard Deviations for Arrays[a]
Au80	Ag	0.09 – 0.15 %
Au60	Au	.18 – .57
Au40	Au	.19 – .25
Au20	Au	.11 – .66

(Note: This range and the two ranges in the following tables are close to the precision of the method and should be considered upper limits of estimates of inhomogeneity.)

Extensive homogeneity studies were performed with the electron probe microanalyzer at NBS by M. A. Giles, R. L. Myklebust, C. E. Fiori, and K. F. J. Heinrich. Measurements of residual resistivity ratio were made at NBS, Boulder, Colorado, by R. L. Rutter, J. G. Hust, and R. L. Powell. Heat treatment of the alloys at NBS was performed by G. E. Hicho and M. R. Meyerson. Spectrographic survey analyses were made at NBS by V. C. Stewart. Determinations of composition were made at Cominco American, Inc., Spokane, Washington, by T. A. Rice; at the U.S. Bureau of the Mint, Washington, D. C., by H. G. Hanson, Jr.; and at NBS by R. A. Durst, G. Marinenko, and C. E. Champion.

Figure B–4: Third page of certificate of analysis for the AuAg standards, SRM 481 [103]

Appendix C
Tables of calculated Au weight fraction

The next tables presents the calculated composition of the AuCu and AgAg alloys, using the different pairs of lines, with and without the continuum and characteristic fluorescence effect and a constant and a beam-energy dependent calibration factor

Table C–1: Calculated Au weight fraction using the AuL-CuK pair of lines with average calibration factors without fluorescence correction

Nominal fraction	15 keV	20 keV	25 keV	30 keV
20 % Au	0.2410	0.1990	0.1912	0.1734
40 % Au	0.4451	0.4051	0.3783	0.3612
60 % Au	0.6803	0.6053	0.5784	0.5651
80% Au	0.8441	0.8039	0.7845	0.7764

Table C–2: Calculated Au weight fraction using the AuL-CuK pair of lines with an average calibration factor and with the fluorescence correction

Nominal fraction	15 keV	20 keV	25 keV	30 keV
20 % Au	0.2382	0.1987	0.1887	0.1731
40 % Au	0.4428	0.4256	0.3782	0.3679
60 % Au	0.6803	0.6255	0.5839	0.5782
80 % Au	0.8574	0.8157	0.7946	0.8009

Table C–3: Calculated Au weight fraction using the AuL-CuL pair of lines with an average calibration factor and without the fluorescence correction

Nominal fraction	15 keV	20 keV	25 keV	30 keV
20 % Au	0.1728	0.1441	0.2088	0.2326
40 % Au	0.3619	0.3404	0.4516	0.4943
60 % Au	0.5993	0.5464	0.5796	0.7168
80% Au	0.8088	0.7802	0.8026	0.8881

Table C–4: Calculated Au weight fraction using the AuL-CuL pair of lines with an average calibration factor and with the fluorescence correction

Nominal fraction	15 keV	20 keV	25 keV	30 keV
20 % Au	0.1612	0.1355	0.2008	0.2261
40 % Au	0.3467	0.3268	0.4375	0.4848
60 % Au	0.5817	0.5306	0.5979	0.6407
80 % Au	0.8007	0.7690	0.8116	0.8370

Table C–5: Calculated Au weight fraction using the AuM-CuK pair of lines with an average calibration factor and without the fluorescence correction

Nominal fraction	15 keV	20 keV	25 keV	30 keV
20 % Au	0.2375	0.2473	0.1512	0.1327
40 % Au	0.4657	0.4802	0.3365	0.3138
60 % Au	0.6746	0.6865	0.6728	0.6444
80% Au	0.7908	0.8645	0.8571	0.8374

Table C–6: Calculated Au weight fraction using the AuM-CuK pair of lines with an average calibration factor and with the fluorescence correction

Nominal fraction	15 keV	20 keV	25 keV	30 keV
20 % Au	0.2290	0.2426	0.1481	0.1308
40 % Au	0.4579	0.4802	0.3368	0.3164
60 % Au	0.6709	0.6936	0.6750	0.6659
80 % Au	0.7900	0.8733	0.8671	0.8592

Table C–7: Calculated Au weight fraction using the AuM-CuL pair of lines with an average calibration factor

Nominal fraction	10 keV	15 keV	20 keV	25 keV	30 keV
20 % Au	0.1771	0.2147	0.2307	0.2150	0.22635772
40 % Au	0.4033	0.4584	0.4839	0.4839	0.52382269
60 % Au	0.6177	0.6793	0.7052	0.7451	0.74946161
80% Au	0.8210	0.8636	0.8848	0.9022	0.91082219

Table C–8: Calculated Au weight fraction using the AuM-AgL pair of lines with an average calibration factor

Nominal fraction	10 keV	15 keV	20 keV	25 keV	30 keV
20 % Au	0.1674	0.1850	0.1618	0.1827	0.18157348
40 % Au	0.3304	0.3523	0.3827	0.4078	0.37910626
60 % Au	0.4792	0.5890	0.6170	0.6212	0.63941131
80% Au	0.7619	0.7897	0.8362	0.8466	0.85541022

Table C–9: Calculated Au weight fraction using the AuL-AgL pair of lines with an average calibration factor and without the fluorescence correction

Nominal fraction	15 keV	20 keV	25 keV	30 keV
20 % Au	0.1547	0.1636	0.2060	0.20621806
40 % Au	0.3759	0.4066	0.4180	0.43161043
60 % Au	0.6049	0.6221	0.6320	0.63858223
80% Au	0.7934	0.8233	0.8435	0.85192286

Table C–10: Calculated Au weight fraction using the AuL-AgL pair of lines with an average calibration factor and with the fluorescence correction

Nominal fraction	15 keV	20 keV	25 keV	30 keV
20 % Au	0.1437	0.1556	0.1972	0.199335101
40 % Au	0.4821	0.3913	0.4053	0.423360633
60 % Au	0.5794	0.6055	0.6169	0.626720166
80% Au	0.7782	0.8132	0.8346	0.844700555

Table C–11: Calculated Au weight fraction using the AuL-CuK pair of lines with a beam-energy-dependent calibration factor and without the fluorescence correction

Nominal fraction	15 keV	20 keV	25 keV	30 keV
20 % Au	0.2108	0.1951	0.2056	0.1984
60 % Au	0.6437	0.6000	0.6009	0.6070
80% Au	0.8205	0.8006	0.8004	0.8052

Table C–12: Calculated Au weight fraction using the AuL-CuK pair of lines with a beam-energy-dependent calibration factor and with the fluorescence correction

Nominal fraction	15 keV	20 keV	25 keV	30 keV
20 % Au	0.2116	0.1940	0.2035	0.1958
60 % Au	0.6424	0.6032	0.6071	0.6150
80 % Au	0.8202	0.8066	0.8110	0.8171

Table C–13: Calculated Au weight fraction using the AuL-CuL pair of lines with a beam-energy-dependent calibration factor and without the fluorescence correction

Nominal fraction	15 keV	20 keV	25 keV	30 keV
20 % Au	0.2002	0.1775	0.1817	0.1688
60 % Au	0.6623	0.6132	0.5328	0.6313
80% Au	0.8305	0.8221	0.7751	0.8371

Table C–14: Calculated Au weight fraction using the AuL-CuL pair of lines with a beam-energy-dependent calibration factor and with the fluorescence correction

Nominal fraction	15 keV	20 keV	25 keV	30 keV
20 % Au	0.2000	0.1769	0.1812	0.1732
60 % Au	0.6560	0.6143	0.5620	0.5509
80 % Au	0.8274	0.8253	0.8050	0.7695

Table C–15: Calculated Au weight fraction using the AuM-CuK pair of lines with a beam-energy-dependent calibration factor and without the fluorescence correction

Nominal fraction	15 keV	20 keV	25 keV	30 keV
20 % Au	0.1916	0.1941	0.1885	0.1781
60 % Au	0.6188	0.6153	0.7285	0.6155
80% Au	0.7448	0.8219	0.8880	0.8254

Table C–16: Calculated Au weight fraction using the AuM-CuK pair of lines with a beam-energy-dependent calibration factor and with the fluorescence correction

Nominal fraction	15 keV	20 keV	25 keV	30 keV
20 % Au	0.1901	0.1907	0.1838	0.1730
60 % Au	0.6221	0.6221	0.7417	0.6281
80 % Au	0.7500	0.8321	0.8989	0.8432

Table C–17: Calculated Au weight fraction using the AuM-CuL pair of lines with a beam-energy-dependent calibration factor

Nominal fraction	10 keV	15 keV	20 keV	25 keV	30 keV
20 % Au	0.1750	0.1813	0.1766	0.1651	0.14930731
60 % Au	0.6142	0.6290	0.6290	0.6747	0.64008136
80% Au	0.8188	0.8352	0.8432	0.8683	0.85555174

Table C–18: Calculated Au weight fraction using the AuM-AgL pair of lines with a beam-energy-dependent calibration factor

Nominal fraction	10 keV	15 keV	20 keV	25 keV	30 keV
20 % Au	0.2479	0.1921	0.1517	0.1695	0.156917788
40 % Au	0.4461	0.3633	0.3664	0.3865	0.338377182
80% Au	0.8398	0.7975	0.8260	0.8340	0.834867199

Table C–19: Calculated Au weight fraction using the AuL-AgL pair of lines with a beam-energy-dependent calibration factor and without the fluorescence correction

Nominal fraction	15 keV	20 keV	25 keV	30 keV
20 % Au	0.1521	0.1527	0.1862	0.1812
40 % Au	0.4931	0.3852	0.3890	0.3943
80% Au	0.7894	0.8100	0.8249	0.8288

Table C–20: Calculated Au weight fraction using the AuL-AgL pair of lines with a beam-energy-dependent calibration factor and with the fluorescence correction

Nominal fraction	15 keV	20 keV	25 keV	30 keV
20 % Au	0.1487	0.1516	0.1867	0.1833
40 % Au	0.5275	0.3828	0.3909	0.3972
80% Au	0.7842	0.8081	0.8247	0.8299

Appendix D
Tables of measured x-ray intensities

The next tables show the characteristic x-ray intensities of the peaks, named AuL, AuM, CuK and CuL in this work. The intensities have been obtained by filtering as shown in section 5.4. The four data in lines are the four measurements for each conditions. Each table represents the values for one standard at one beam energy in counts.

Table D–1: Measured x-ray intensity for the $Au_{20}Cu_{80}$ standard at 10 keV

Nominal fraction	Point 1	Point 2	Point 3	Point 4
AuLα	0	0	0	0
AuMα	16479.3	16313.3	16772.1	16997.6
CuKα	0	0	0	0
CuLα	109597	107447	104896	107373

Table D–2: Measured x-ray intensity for the $Au_{20}Cu_{80}$ standard at 15 keV

Nominal fraction	Point 1	Point 2	Point 3	Point 4
AuLα	2657.86	2612.65	2565.81	2468.87
AuMα	19171.6	19008.6	18572.1	18189.3
CuKα	53202.6	52003.2	51520.4	51614.8
CuLα	67632.1	64498.8	64275.4	64817.8

Table D–3: Measured x-ray intensity for the $Au_{20}Cu_{80}$ standard at 20 keV

Nominal fraction	Point 1	Point 2	Point 3	Point 4
AuLα	2657.86	2612.65	2565.81	2468.87
AuMα	19171.6	19008.6	18572.1	18189.3
CuKα	53202.6	52003.2	51520.4	51614.8
CuLα	67632.1	64498.8	64275.4	64817.8

Table D–4: Measured x-ray intensity for the $Au_{20}Cu_{80}$ standard at 25 keV

Nominal fraction	Point 1	Point 2	Point 3	Point 4
AuLα	3162.58	3212.42	3306.31	3756.09
AuMα	6741.82	6737.98	6773.57	6901.42
CuKα	55443.9	54865.4	54896.3	54546
CuLα	24885.1	24282.7	25152.1	24710.2

Table D–5: Measured x-ray intensity for the $Au_{20}Cu_{80}$ standard at 30 keV

Nominal fraction	Point 1	Point 2	Point 3	Point 4
AuLα	3642.14	3850.67	3772.7	3944.68
AuMα	4773.9	4917.6	4829.84	5088.8
CuKα	61167.1	61915.4	62193.1	61158.6
CuLα	16573.5	16047.5	16243.3	16373.7

Table D–6: Measured x-ray intensity for the $Au_{40}Cu_{60}$ standard at 10 keV

Nominal fraction	Point 1	Point 2	Point 3	Point 4
AuLα	0	0	0	0
AuMα	39152.4	37844.9	32143.3	38223.8
CuKα	0	0	0	0
CuLα	73481.1	74043.2	62358	74497.2

Table D–7: Measured x-ray intensity for the $Au_{40}Cu_{60}$ standard at 15 keV

Nominal fraction	Point 1	Point 2	Point 3	Point 4
AuLα	1288.62	1490.86	1493.22	1461.9
AuMα	46045	46698.3	46171	45727.1
CuKα	21719	22350.2	22037.5	22108.5
CuLα	59573.7	60051.2	60570.8	58603.2

Table D–8: Measured x-ray intensity for the $Au_{40}Cu_{60}$ standard at 20 keV

Nominal fraction	Point 1	Point 2	Point 3	Point 4
AuLα	5566.55	5665.71	5550.24	5896.95
AuMα	41903.8	42351.8	42502.2	43130.3
CuKα	40108.3	41324.7	41353.8	42299.1
CuLα	41382.2	44205.6	42545	47224.6

Table D–9: Measured x-ray intensity for the $Au_{40}Cu_{60}$ standard at 25 keV

Nominal fraction	Point 1	Point 2	Point 3	Point 4
AuLα	6992.05	6955.61	6721.02	7265.27
AuMα	16549.2	15721.9	15480	16025.6
CuKα	43407.8	42578.1	42604.8	43782.6
CuLα	16006	15803	15205.4	16366.4

Table D–10: Measured x-ray intensity for the $Au_{40}Cu_{60}$ standard at 30 keV

Nominal fraction	Point 1	Point 2	Point 3	Point 4
AuLα	7965.96	8104.81	8186.15	8026.18
AuMα	12801.6	12134.2	12440.2	12224.4
CuKα	47874.8	47399.6	47328.8	47347.1
CuLα	10486.8	10210.2	10175.4	9793.24

Table D–11: Measured x-ray intensity for the $Au_{60}Cu_{40}$ standard at 10 keV

Nominal fraction	Point 1	Point 2	Point 3	Point 4
AuLα	0	0	0	0
AuMα	64235.3	64078.3	62564.7	63655.2
CuKα	0	0	0	0
CuLα	48812.7	48433.5	47308.7	49364.2

Table D–12: Measured x-ray intensity for the $Au_{60}Cu_{40}$ standard at 15 keV

Nominal fraction	Point 1	Point 2	Point 3	Point 4
AuLα	2716.01	2578.51	2861.29	2629.07
AuMα	79000	74167.5	78560.9	78376.5
CuKα	15589.1	14712.7	15528.7	15699.5
CuLα	38386.1	35163.4	37945.2	37389.8

Table D–13: Measured x-ray intensity for the $Au_{60}Cu_{40}$ standard at 20 keV

Nominal fraction	Point 1	Point 2	Point 3	Point 4
AuLα	8697.27	8439.1	8824.47	8851.1
AuMα	65654.8	68973.6	69863.3	69449.3
CuKα	27205.7	27451.6	27165.9	27466.9
CuLα	26963.3	26409	26571.7	26424.1

Table D–14: Measured x-ray intensity for the $Au_{60}Cu_{40}$ standard at 25 keV

Nominal fraction	Point 1	Point 2	Point 3	Point 4
AuLα	14430.4	13933.9	13686.8	14047.1
AuMα	57966.9	56472.8	56457.1	57483.7
CuKα	38037.6	36700.1	37324.9	37115.8
CuLα	16495.3	16162.6	16147.1	16096.6

Table D–15: Measured x-ray intensity for the $Au_{60}Cu_{40}$ standard at 30 keV

Nominal fraction	Point 1	Point 2	Point 3	Point 4
AuLα	18102.6	18044.4	18005.6	18347.3
AuMα	47888.3	47778.9	48218.3	47796.6
CuKα	44434.5	44105.7	45039.5	44269.2
CuLα	11709.3	11839.4	11633.2	11707.1

Table D–16: Measured x-ray intensity for the $Au_{80}Cu_{20}$ standard at 10 keV

Nominal fraction	Point 1	Point 2	Point 3	Point 4
AuLα	0	0	0	0
AuMα	93085.6	91968.8	94236	94421.2
CuKα	0	0	0	0
CuLα	23761.4	23812.1	24191.5	24174.7

Table D–17: Measured x-ray intensity for the $Au_{80}Cu_{20}$ standard at 15 keV

Nominal fraction	Point 1	Point 2	Point 3	Point 4
AuLα	3353.06	3393.11	3432.15	3517.16
AuMα	102588	104374	101292	100763
CuKα	6996.44	7498.56	7275.07	7089.76
CuLα	15652.4	16016.3	15536.7	15924.3

Table D–18: Measured x-ray intensity for the $Au_{80}Cu_{20}$ standard at 20 keV

Nominal fraction	Point 1	Point 2	Point 3	Point 4
AuLα	10442.6	10945.8	10584.8	10705.6
AuMα	89292.1	90388	87751	86924.5
CuKα	12478.5	12523.4	12070.9	11886.7
CuLα	10486	10602.8	10505.9	10310.9

Table D–19: Measured x-ray intensity for the $Au_{80}Cu_{20}$ standard at 25 keV

Nominal fraction	Point 1	Point 2	Point 3	Point 4
AuLα	18664.5	18169.1	17837.2	18220.9
AuMα	82739.6	80670.2	81178.3	79710.4
CuKα	18199.9	18280.1	18004.3	17898.2
CuLα	6714.38	7051.45	6865.81	6889.16

Table D–20: Measured x-ray intensity for the $Au_{80}Cu_{20}$ standard at 30 keV

Nominal fraction	Point 1	Point 2	Point 3	Point 4
AuLα	23695	23341.7	23790	23433.9
AuMα	68193.6	67970.8	68498.1	68727.6
CuKα	21549.9	21965.1	22151.4	21143.3
CuLα	5046.8	5170.46	5056.94	5070.39

Table D–21: Measured x-ray intensity for the $Au_{20}Ag_{80}$ standard at 10 keV

Nominal fraction	Point 1	Point 2	Point 3	Point 4
AuLα	0	0	0	0
AuMα	1431.98	21043.8	1834.21	17355.7
AgKα	0	0	0	0
AgLα	44843.3	42872	33224.9	43249.4

Table D–22: Measured x-ray intensity for the $Au_{20}Ag_{80}$ standard at 15 keV

Nominal fraction	Point 1	Point 2	Point 3	Point 4
AuLα	503.046	356.047	601.45	246.599
AuMα	24096	22613	21868.6	2520.51
AgKα	0	0	0	0
AgLα	59092.6	59423.1	61249.8	59467.9

Table D–23: Measured x-ray intensity for the $Au_{20}Ag_{80}$ standard at 20 keV

Nominal fraction	Point 1	Point 2	Point 3	Point 4
AuLα	1912.58	2135.38	1242.56	1690
AuMα	8791.66	16770.3	18201.5	17526.6
AgKα	0	0	0	0
AgLα	46409.8	50079.6	52953.2	50168.2

Table D–24: Measured x-ray intensity for the $Au_{20}Ag_{80}$ standard at 25 keV

Nominal fraction	Point 1	Point 2	Point 3	Point 4
AuLα	3984.87	3955.08	4954.81	4786.53
AuMα	15873.6	11618	18596	20110
AgKα	0	0	0	0
AgLα	44042.6	49398.8	55218.3	53399

Table D–25: Measured x-ray intensity for the $Au_{20}Ag_{80}$ standard at 30 keV

Nominal fraction	Point 1	Point 2	Point 3	Point 4
AuLα	6769.94	4826.53	7098.37	6402.15
AuMα	20144.2	14341.4	12890	16274
AgKα	0	0	0	0
AgLα	52632.4	50340.1	49386.7	51198.2

Table D–26: Measured x-ray intensity for the $Au_{40}Ag_{60}$ standard at 10 keV

Nominal fraction	Point 1	Point 2	Point 3	Point 4
AuLα	0	0	0	0
AuMα	4455.98	44912.4	44057.7	45307.5
AgKα	0	0	0	0
AgLα	41281.7	39106.8	40679	41258.4

Table D–27: Measured x-ray intensity for the $Au_{40}Ag_{60}$ standard at 15 keV

Nominal fraction	Point 1	Point 2	Point 3	Point 4
AuLα	1534.58	509.021	204.127	0
AuMα	41018.5	39174.9	40212.4	0
AgKα	0	0	0	0
AgLα	41101	40874.9	42153.8	0

Table D–28: Measured x-ray intensity for the $Au_{40}Ag_{60}$ standard at 20 keV

Nominal fraction	Point 1	Point 2	Point 3	Point 4
AuLα	5865.87	4599.34	5133.79	5385.6
AuMα	33714.3	39126.3	46639.7	43238.9
AgKα	0	0	0	0
AgLα	41796.3	41430.1	36188.7	40953.4

Table D–29: Measured x-ray intensity for the $Au_{40}Ag_{60}$ standard at 25 keV

Nominal fraction	Point 1	Point 2	Point 3	Point 4
AuLα	8649.44	8071.38	8934.99	6494.93
AuMα	32392.6	34615.8	36699.3	32431.9
AgKα	0	0	0	0 hline AgLα
32118.8	32234.7	30437.4	32838.7	

Table D–30: Measured x-ray intensity for the $Au_{40}Ag_{60}$ standard at 30 keV

Nominal fraction	Point 1	Point 2	Point 3	Point 4
AuLα	14480.2	12787.6	13865.9	13892.3
AuMα	3694.57	33990.7	37072.9	26930.2
AgKα	0	0	0	0
AgLα	36621.9	34584.1	36996.9	36137.7

Table D–31: Measured x-ray intensity for the $Au_{60}Ag_{40}$ standard at 10 keV

Nominal fraction	Point 1	Point 2	Point 3	Point 4
AuLα	0	0	0	0
AuMα	42441.4	72907.7	14908.6	59393
AgKα	0	0	0	0
AgLα	26503.5	27808.8	28205.8	27098.6

Table D–32: Measured x-ray intensity for the $Au_{60}Ag_{40}$ standard at 15 keV

Nominal fraction	Point 1	Point 2	Point 3	Point 4
AuLα	1536.75	1265.54	1858.82	1508.64
AuMα	5903.71	63010	63696.5	66682
AgKα	0	0	0	0
AgLα	22542.8	24439.1	24521.5	24223.4

Table D–33: Measured x-ray intensity for the $Au_{60}Ag_{40}$ standard at 20 keV

Nominal fraction	Point 1	Point 2	Point 3	Point 4
AuLα	7662.48	8196.01	7019.66	7080.13
AuMα	59662.2	58996.9	64089.3	59217.8
AgKα	0	0	0	0
AgLα	22204.7	23275.2	22488.9	21126

Table D–34: Measured x-ray intensity for the $Au_{60}Ag_{40}$ standard at 25 keV

Nominal fraction	Point 1	Point 2	Point 3	Point 4
AuLα	14141.1	13082.8	12397.3	4878.07
AuMα	53022.3	56040.4	56777.4	55965.9
AgKα	0	0	0	0
AgLα	20324.6	21685.9	20646.4	21533.1

Table D–35: Measured x-ray intensity for the $Au_{60}Ag_{40}$ standard at 30 keV

Nominal fraction	Point 1	Point 2	Point 3	Point 4
AuLα	14642.2	14175.9	14767.9	16415.7
AuMα	46994.6	44224.3	46275.6	3870.88
AgKα	0	0	0	0
AgLα	15340	16481.3	17539	15657.1

Table D–36: Measured x-ray intensity for the $Au_{80}Ag_{20}$ standard at 10 keV

Nominal fraction	Point 1	Point 2	Point 3	Point 4
AuLα	0	0	0	0
AuMα	78460	34194.9	77063.9	80955.3
AgKα	0	0	0	0
AgLα	11955.2	11779.3	10943.4	8975.77

Table D–37: Measured x-ray intensity for the $Au_{80}Ag_{20}$ standard at 15 keV

Nominal fraction	Point 1	Point 2	Point 3	Point 4
AuLα	1527	1633.78	2594.44	910.087
AuMα	65063.4	89850.1	88325.5	7464.67
AgKα	0	0	0	0
AgLα	10741.1	11255.7	12018.2	11970.1

Table D–38: Measured x-ray intensity for the $Au_{80}Ag_{20}$ standard at 20 keV

Nominal fraction	Point 1	Point 2	Point 3	Point 4
AuLα	20906.1	21931.1	20303.8	9739.36
AuMα	178981	176150	32147.3	97025.2
AgKα	0	0	0	0
AgLα	18866.1	19487.7	21685.1	11746.6

Table D–39: Measured x-ray intensity for the $Au_{80}Ag_{20}$ standard at 25 keV

Nominal fraction	Point 1	Point 2	Point 3	Point 4
AuLα	19180.7	18828.8	19032.3	17721.8
AuMα	79882.2	84948.6	8287.58	81862.9
AgKα	0	0	0	0
AgLα	8999.41	8998.66	9721.9	9070.17

Table D–40: Measured x-ray intensity for the $Au_{80}Ag_{20}$ standard at 30 keV

Nominal fraction	Point 1	Point 2	Point 3	Point 4
AuLα	24856	21255.4	25448.3	22033.1
AuMα	73808.3	18413.5	77928.8	67312.9
AgKα	0	0	0	0
AgLα	6816.01	7790.37	7959.37	7904.33

References

[1] J. T. Armstrong. *Microbeam Analysis*, page 469. San Francisco Press, San Francisco, 1988.

[2] Walter Bambynek, Bernd Crasemann, R. W. Fink, H.-U. Freund, Hans Mark, C. D. Swift, R. E. Price, and P. Venugopala Rao. X-ray fluorescence yields, Auger, and Coster-Kronig transition probabilities. *Reviews of Modern Physics*, 44(4):716–813, 1972.

[3] G. F. Bastin, J. M. Dijkstra, and H. J. M. Heijligers. PROZA96: An improves matrix correction program for electron probe microanalysis, based on a double Gaussian $\varphi(\rho z)$ approach. *X-Ray Spectrometry*, 27:3–10, 1998.

[4] J. A. Bearden and A. F. Burr. Reevaluation of X-Ray Atomic Energy Levels. *Rev. Mod. Phys.*, 39(1):125–142, 1967.

[5] D. Benoît. Méthodes de soustraction du fond continu et de déconvolution des pics. In *Microanalyse Par Sonde Électronique : Aspects Quantitatifs*, pages F1–F21, Paris, France, 1989. Association Nationale de la Recherche Technique.

[6] M. L. Berger and S. M. Seltzer. *Studies of Penetration of Charged Particles in Matter*. Natural Ressources Council Pub. 1133, National Academy of Sciences, Washinghton, 1964.

[7] H. Bethe. *Handbook of Physics*, volume 24, page 273. Springer, 1933.

[8] H. A. Bethe. Zur Theorie des Durchgangs Schneller Korpuskularstrahlen durch Materie. *Ann. Physik*, 5:325, 1930.

[9] J. D. Brown and R. H. Packwood. Quantitative Electron Probe Microanalysis Using Gaussian Curves. *X-Ray Spectrometry*, 11(4):187–193, 1982.

[10] R. Browning, T.Z. Li, B. Chui, Jun Ye, R.F. Pease, Z. Czyzewski, and D.C. Joy. Empirical forms for the electron/atom elastic scattering cross sections from 0.1 to 30 keV. *J. Appl. Phys.*, 76(4):2016–2022, August 1994.

[11] J. L. Campbell. Fluorescence yields and Coster-Kronig probabilities for the atomic L subshells. *Atomic Data and Nuclear Data Tables*, 82:291–315, 2003.

[12] E. Casnati, A. Tartari, and C. Baraldi. An empirical approach for K-shell ionisation cross-section by electrons. *J. Phys. B*, 15:155–167, 1982.

[13] R. Castaing. PhD thesis, University of Paris, Publication O.N.E.R.A., 1952.

[14] R. Castaing. *Electron Probe Quantitation*, chapter Early Times of Electron Microprobe Analysis, pages 1–7. Plenum Press, 1991.

[15] P. E. Champness, G. Cliff, and G. W. Lorimer. Quantitative analytical electron microscopy of metals and minerals. *Ultramicroscopy*, 8:121–132, 1982.

[16] J. N. Chapman, C. C. Gray, B. W. Robertson, and W. A. P. Nicholson. X-ray production in thin films by electrons with energies between 40 and 100 keV: 1– bremsstrahlung cross-sections. *X-Ray Spectrometry*, 12(4):153 – 162, 1983.

[17] M. H. Chen, B. Crasemann, and H. Mark. Widths and fluorescence yields of atomic L-shell vacancy states. *Phys. Rev. A*, 24:177, 1981.

[18] Mau Hsiung Chen and Bernd Craseman. Radiationless transitions to atomic$M_{1,2,3}$ shells results of relativistic theory. *Physical Review A*, 27(6):2989–1994, 1983.

[19] Mau Hsiung Chen and B. Crasemann. M x-ray emission rates in Dirac-Fock approximations. *Physical Review A*, 30(1):170–176, 1974.

[20] G. Cliff and G. W. Lorimer. The quantitative analysis of thin specimen. *Journal of Microscopy - Oxford*, 103:203–207, 1975.

[21] Zbigniew Czyzewski, Danny O'Neill MacCallum, Alton Romig, and David C. Joy. Calculation of Mott scattering cross section. *J. Appl. Phys.*, 68(7):3066–3072, 1 1990.

[22] D. V. Davis, V. D. Mistry, and C. A. Quarles. Inner shell ionization of copper, silver and gold by electron bombardment. *Phys. Lett. A*, 38(3):169 – 170, 1972.

[23] Hendrix Demers. Filtering of spectra for background subtraction. Personal communication, 2005.

[24] R.D. Deslattes, E.G. Kessler, P. Indelicato Jr., L. de Billy, E. Lindroth, and J. Anton. X-ray transition energies : New approach to a comprehensive evaluation. *Rev. Mod. Phys.*, 75(1):35–99, 2003.

[25] Dominique Drouin, Pierre Hovington, and Raynald Gauvin. CASINO: A new Monte Carlo code in C language for electron beam interaction - part II: Tabulated values of Mott cross section. *Scanning*, 19:20–28, 1997.

[26] P. Duncumb and S. J. B. Reed. *The Electron Microprobe Microanalysis*, page p. 133. National Bureau of Standards Special Publication 298, 1968.

[27] R. F. Egerton. *Electron Energy-Loss Spectroscopy in the Electron Microscope.* Plenum Press, 1986.

[28] Mehmet Ertugrul. Measurement of L-subshell X-ray fluorescence cross-section and L-subshell fluorescence yields for the elements in the atomic range $73 \leq Z \leq 92$ at 60 keV. *Instrumentation Science and Technology*, 29(3):215 – 222, 2001.

[29] R. G. Faulkner, E. A. Little, and G. J. Adetunji. Comparative STEM and FEGSTEM analysis of grain boundaries in steels. *Mater. Charac.*, 25:83–97, 1990.

[30] J. M. Fernández-Varea, D. Liljequist, S. Csillag, R. Räty, and F. Salvat. Monte Carlo simulation of 0.1-100 keV electron and positron transport in solids using optical data and partial wave methods. *Nuclear Instruments and Methods in Physics Research B*, 108:35–50, 1996.

[31] Chuck Fiori, Carol Swyt-Thomas, and Bob Myklebust. Desktop Spectrum Analyzer (DTSA). http://www.cstl.nist.gov/div837/Division/outputs/DTSA/DTSA.htm, 2005.

[32] R. Gauvin and G. L'Espérance. A Monte Carlo code to simulate the effect of fast secondary electron on k_{AB} factors and spatial resolution in the TEM. *J. Microsc.*, 168:152–167, 1992.

[33] Raynald Gauvin. *Analyse Chimique Quantitative en Microscopie Électronique.* PhD thesis, École Polytechnique de Montréal, Juin 1990.

[34] Raynald Gauvin and Dominique Drouin. A formula to compute total elastic Mott cross-sections. *Scanning*, 15:140–150, 1993.

[35] Raynald Gauvin and Gilles L'Espérance. A monte carlo code to simulate the effect of fast secondary electrons on k_{AB} factors and spatial resolution in the TEM. *Journal of Microscopy*, 168(2):153–167, 1992.

[36] Raynald Gauvin, Eric Lifshin, Hendrix Demers, Paula Horny, and Helen Campbell. Win X-ray, a new Monte Carlo program that computes x-ray spectrum obtained with a scanning electron microscope. *Microscopy and Microanalysis*, 12:49–64, 2006.

[37] Joseph I. Goldstein, Dale E. Newbury, David C. Joy, Charles E. Lyman, Patrick Echlin, Eric Lifshin, L.C. Sawyer, and J.R. Michael. *Scanning Electron Microscopy and X-Ray Microanalysis.* Plemum Press, third edition, 2003.

[38] M. Green. Angular distribution of characteristic x radiation and its origin within solid target. *Proc. Roy. Soc.*, 83(533):435 - 451, 1964.

[39] M. Green and V. E. Cosslet. Measurements of K, L and M shell X-ray production efficiencies. *Brit. J. Appl. Phys.*, 1, series 2(4):425 - 436, 1968.

[40] Michal Gryzínski. Classical theory of atomic collisions. I. Theory of inelastic collisions. *Physical review*, 138(2A):A336–A358, 19 1965.

[41] K. F. J. Heinrich. *Electron Microprobe*, page 296. Wiley, New York, 1966.

[42] K. F. J. Heinrich. In J. D. Brown and R. H. Packwood, editors, *Proc. 11th Intl. Conf. On X-Ray Optics and Microanalysis*, page 67, London, Ontario, Canada, 1986. Univ. Western Ontario.

[43] K. F. J. Heinrich, R. L. Myklebust, S. D. Rasberry, and R. E. Michaelis. Standard reference materials: Preparation and evaluation of SRM's 481 and 482 Gold-Silver and Gold-Copper alloys for microanalysis. Technical Report 260-28, National Bureau of Standards, 1971.

[44] K. F. J. Heinrich and H. Yakowitz. *Pratical Scanning Electron Microscopy : Electron and Ion Microprobe Analysis*, page 338. Plenum Press, New York, 1975.

[45] Kurt F. J. Heinrich. Paramètres en microanalyse par sonde électronique. In *Microanalyse Par Sonde Electronique : Aspects Quantitatifs*, pages B1–B24, Paris, 1989. Association Nationale de la Recherche Technique.

[46] Kurt F. J. Heinrich. Uncertainty in quantitative electron probe microanalysis. *J. Res. Natl. Inst. Stand. Technol.*, 107(6):483–485, 2002.

[47] B. L. Henke, E. M. Gullikson, and J.C. Davis. X-ray interactions: Photoabsorption, scattering, transmission, and reflection at E = 50-30,000 eV, Z = 1-92. *Atomic Data and Nuclear Data Tables*, 54:181–342, 1993.

[48] Pierre Hovington, Dominique Drouin, and Raynald Gauvin. CASINO: A new Monte Carlo code in C language for electron beam interaction - part I: Description of the program. *Scanning*, 19:1–14, 1997.

[49] Pierre Hovington, Dominique Drouin, Raynald Gauvin, David C. Joy, and Neal Evans. CASINO: A new Monte Carlo code in C language for electron beam interaction - part III: Stopping power at low energies. *Scanning*, 19:29–35, 1997. CASINO III.

[50] J. H. Hubbell and S. M. Seltzer. Cross section data for electron-positron pair production by photons: A status report. *Nucl. Instr. and Meth. in Phys. Res. B*, 213:1–9, 2004.

[51] J. H. Hubbell, P. N. Trehan, Nirmal Singh, B. Chand, D. Mehta, M. L. Garg, R. R Garg, Surinder Singh, and S. Puri. A review, bibliography, and tabulation of K, L and M higher atomic shell x-ray fluorescence yields. *J. Phys. Chem. Ref. Data*, 23(2):339–364, 1994.

[52] John H. Hubbell. Compilation of photon cross-sections: Some historical remarks and current status. *X-Ray Spectrometry*, 28(4):215–223, 1999.

[53] D. C. Joy and S. Luo. An empirical stopping power relationship for low-energy electrons. *Scanning*, 11:176, 1989.

[54] David C. Joy. A database of elecron-solid interactions. http://web.utk.edu/ srcutk/htm/interact.htm, 2001.

[55] David C. Joy. Fundamental constants for quantitative x-ray microanalysis. *Miscros. Microanal.*, 7:159–167, 2001.

[56] Paul Kirkpatrick and Lucille Wiedmann. Theoritical continuous x-ray energy and polarization. *Physical Review*, 67:321–339, 1945.

[57] M. O. Krause. Atomic radiative and radiationless yields for K and L shells. *J. Phys. Chem. Ref. Data*, 8(2):307–326, 1979.

[58] D. F. Kyser and K. Murata. Quantitative electron-microprobe analysis of thin-films on substrates. *IBM J. Res. Dev.*, 18(4):352 - 363, 1974.

[59] Jinyue Liu. High-resolution and low-voltage FE-SEM imaging and microanalysis in materials characterization. *Mater. Charact.*, 44:353–363, 2000.

[60] X. Llovet, C. Merlet, and F. Salvat. Measurements of K-shell ionization cross sections of Cr, Ni and Cu by impact of 6.5-40 keV electrons. *J. Phys. B. : At. Mol. Opt. Phys.*, 33(18):3761–3772, 2000.

[61] Xavier Llovet, Claude Merlet, José M. Fernandez-Varea, and Francesc Salvat. Relative cross sections for L- and M- shell ionization by electron impact. *Mikrochimica Acta*, 132:163–171, 2000.

[62] M. W. Lund. *Current Trends in Si(Li) Detector Windows for Light Element Analysis*, chapter 3, pages 21–31. Plenum Press, 1995.

[63] G. L. Macdonald. X-ray spectrometry. *Anal. Chem.*, 50(5):135–142, 1978.

[64] Ricardo Mayol and Francesc Salvat. Cross sections for K-shell ionisation by electron impact. *J. Phys. B. : At. Mol. Opt. Phys.*, 23(12):2117–2130, 1990.

[65] Eugene J. McGuire. Atomic L-shell coster-kronig, auger, and radiative rates and flourescence yields for Na-Th. *Phys. Rev. A*, 3(3):587 - 594, 1971.

[66] Eugene J. McGuire. Atomic M-shell Coster-Kronig, Auger, and ratidative rates, and fluoresence yieds for Ca-Th. *Phys. Rev. A*, 5(3):1043–1047, 1972.

[67] C. Merlet, X. Llovet, and F. Salvat. Measurements of absolute K-shell ionization cross sections and L-shell x-ray production cross-section of Ge by electron impact. *Physical Review A*, 69(3):032708–1–032708–7, 2004.

[68] Claude Merlet. An Accurate Computer Correction Program for Quantitative Electron Probe Microanalysis. *Mikrochim. Acta*, 114/115:363–376, 1994.

[69] Y. Miyagawa, S. Nakamura, and S. Miygawa. Analytical formulas for ionization cross sections and Coster-Kronig corrected fluorescence yields of the L1, L2 and L3 subshells. *Nuclear Instruments and Methods in Physics Research*, B30:115–122, 1988.

[70] N. F. Mott and H. S. W. Massey. *The Theory of Atomic Collisions.* Oxford, 1965.

[71] D. E. Newbury and R. L. Myklebust. *Analytical Electron Microscopy*, chapter A Monte Carlo Electron Trajectory Simulation for Analytical Electron Microscopy, pages 91–97. San Francisco Press, 1981.

[72] D. E. Newbury, C. R. Swyt, and R. L. Myklebust. Standardless quantitative electron probe microanalysis with energy-dispersive x-ray spectrometry. Is it worth the risk? *Analytical Chemistry*, 67(11):1866, 1995.

[73] National Institute of Standards and Technology. Materials details - SRM 481 = Gold-Silver EPMA, 2006. *https* : *//srmors.nist.gov/view_detail.cfm?srm* = 481.

[74] National Institute of Standards and Technology. Materials details - SRM 482 = Gold-Copper EPMA, 2006. *https* : *//srmors.nist.gov/view_detail.cfm?srm* = 482.

[75] Elif Öz, Yüksel Özdemir, Neslihan Ekinci, Mehmet Ertugrul, Yusuf Sahin, and Hasan Erdogan. Measurement of atomic L shel fluorescence (ϖ_1, ϖ_2 and ϖ_3) and auger (a_1, a_2, a_3) yields for some elements in the atomic number range $59 \leq Z \leq 85$. *Spectrochimica Acta Part B*, 55:1869–1877, 2000.

[76] J. Philibert. In H. H. Pattee, V. E. Cosslet, and A. Engstrom, editors, *Proc. 3rd Intl. Symp. X-Ray Optics and X-Ray Microanalysis*, pages 379 – 392, New York, 1963. Standford University, Academic Press.

[77] J.-L. Pouchou and F. Pichoir. *Electron Probe Quantitation*, chapter Quantitative Analysis of Homogeneous or Stratified Microvolumes Applying the Model "PAP", pages 31–75. Plenum Press, New York, 1991.

[78] Jean-Louis Pouchou. Modèles de correction pour la microanalyse x quantitative. In *Microanalyse Par Sonde Electronique : Aspects Quantitatifs*, pages C1–C36, Paris, 1989. Association Nationale de la Recherche Technique.

[79] Jean-Louis Pouchou. Standardless x-ray analysis of bulk specimen. *Mikrochim. Acta*, 114/115:33–52, 1994.

[80] C. J. Powell. Abstract : Cross sections for ionization of inner-shell electrons by electron impact. *J. Vac. Sci. Technol.*, 13(1):219–220, 1976.

[81] C. J. Powell. Cross sections for ionization of inner-shell electrons by electrons. *Rev. Mod. Phys.*, 48(1):33–47, 1976.

[82] S. Puri, D. Mehta, B. Chand, N. Singh, and P. N. Trehan. L shell fluorescence yields and coster - kronig transition probabilities for the elements with $25 \leq Z \leq 96$. *X-ray Spectrometry*, 22(5):359 – 361, 1993.

[83] S. Puri, D. Mehta, B. Chand, Nirmal Singh, P. C. Mangal, and P. N. Trehan. M shell x-ray production cross sections and fluorescence yields for the elements with $71 \leq Z \leq 92$ using 5.96 keV. *Nuclear Instruments and Methods in Physics Research*, 73:319–323, 1993.

[84] S. J. B. Reed. Characteristic fluorescence correction in electron-probe microanalysis. *Brit. J. Appl. Phys.*, 16:913–926, 1965.

[85] S. J. B. Reed. *Electron Microprobe Analysis, Second Edition.* Cambridge University Press, 1993.

[86] Ludwig Reimer. *Scanning Electron Microscopy: Physics of Image Formation and Microanalysis*, volume 45 of *Springer Series in Optical Sciences.* Springer, second edition, 1998.

[87] Peter Rez. Electron ionization cross-sections for K, L and M shells. *X-Ray Spectrometry*, 13(2):55–59, 1984.

[88] Peter Rez. Accurate cross sections for microanalysis. *Journal of Research of the Nationale Institute of Standards and Technology*, 107:487–495, 2002.

[89] Peter Rez. Electron ionization cross sections for atomic subshells. *Microsc. Microanal.*, 9:42–53, 2003.

[90] S. I. Salem and L. D. Moreland. LII and LIII ionization cross sections in gold at very low energies. *Phys. Lett. A*, 37(2):161 – 162, 1971.

[91] Francesc Salvat and José Fernandez-Varea. Semiempirical cross sections for the simulation of the energy loss of electrons ans positrons in matter. *Nucl. Intruments Methods Phys. Res. B*, 63(3):255–269, 1992.

[92] Francesc Salvat, José M. Fernández-Varea, Eduardo Acosta, and Josep Sempau. PENELOPE - A code system forMonte Carlo simulation of electron and photon transport. Nuclear Energy Agency, November 2001.

[93] Francesc Salvat, José M. Fernández-Varea, and Josep Sempau. *PENELOPE - A Code System for Monte Carlo Simulation of Electron and Photon Transport.* Nuclear Energy Agency, Facultat de Física (ECM), Universitat de Barcelona,

Spain, November 2003. Workshop Proceedings, Issy-les-Moulineaux, France, 7–10 July 2003.

[94] Francesc Salvat and Ricardo Mayol. Elastic scattering of electrons and positrons by atoms. Schrödinger and Dirac partial wave analysis. *Computer physics communications*, 74:358–374, 1993.

[95] F. H. Schamber. *X-Ray Fluorescence Analysis of Environmental Samples*, chapter A Modification of the Linear Least-Square Fitting Method Which Provides Continuum Suppression, pages 241–257. Chapell Hill, 1977.

[96] H. Schneider, I. Tobehn, F. Ebel, and R. Hippler. Absolute cross sections for inner shell ionization by lepton impact. *Phys. Rev. Lett.*, 71(17):2707 - 2709, 1993.

[97] T. P. Schreiber and A. W. Wims. *Microbeam Analysis*, chapter Relative Intensities of K- and L-Shell X-Ray Lines, pages 161–166. San Francisco Press, San Francisco, CA, 1982.

[98] James H. Scofield. Hatree-Fock values of L x-ray emission rates. *Physical Review A*, 10(5):1507–1510, 1974.

[99] James H. Scofield. K- and L- ionization of atoms by relativistic electrons. *Physical Review A*, 18(3):963–970, 1978.

[100] M. P. Seah and I. S. Gilmore. Quantitative AES VII. the ionization cross-section in AES. *Surface and Interface Analysis*, 26(11):815 - 824, 1998.

[101] R. Shimizu and Z. J. Ding. Monte Carlo modelling of electron solid interaction. *Rep. Prog. Phys.*, pages 487–531, 1992.

[102] R. Shimizu, Y. Kataoka, T. Ikuta, T. Koshikawa, and H. Hashimoto. A Monte Carlo approach to direct simulation of electron penetration in solids. *J. Phys. D: Appl. Phys.*, 9:101–114, 1976.

[103] Maurice H. Stans. Certificate of analysis - standard reference material 481 gold-silver wires for microprobe analysis. https://srmors.nist.gov/view_detail.cfm?srm=481, 1969.

[104] Maurice H. Stans. Certificate of analysis - standard reference material 482 gold-copper wires for microprobe analysis. https://srmors.nist.gov/view_detail.cfm?srm=482, 1969.

[105] Peter J. Statham. Deconvolution and background subtraction by least-squares fitting with prefiltering of spectra. *Analytical Chemistry*, 49(14):2149–2154, 1977.

[106] Peter J. Statham. Limitations to accuracy in extracting characteristic line intensities from XS-ray spectra. *J. Res. Natl. Inst. Stand. Technol.*, 107(6):531–546, 2002.

[107] Imre Szalóki, Jànos Osán, and René Van Grieken. X-ray spectrometry. *Anal. Chem.*, 76(12):3445–3470, 2004.

[108] H. Tawara, K. G. Harrison, and F. G. De Heer. X-ray emission cross sections and fluorescence yields for lights atoms and molecules by electron impact. *Physica*, 63:351–367, 1973.

[109] Tran Phuc Thinh and Jean Leroux. New basic empirical expression for computing tables of x-ray mass attenuation coefficients. *X-Ray Spectrometry*, 8(2):85 – 91, 1979.

[110] Nicholas Tsoulfanidis. *Measurement and Detection of Radiation.* Taylor & Francis, Washington, second edition edition, 1995.

[111] Eris S. Windsor, Robert A. Carlton, Greg Gillen, Scott A. Wight, and David S. Bright. Copper Oxide precipitates in NBS standard reference material 482. *J. Res. Natl Inst. Stand. Technol.*, 107(6):663 – 679, 2002.